Investigating Self-Assembled Monolayers and Understanding Small Molecule/Polymer Blend Thin-Films in Organic Field-Effect Transistors

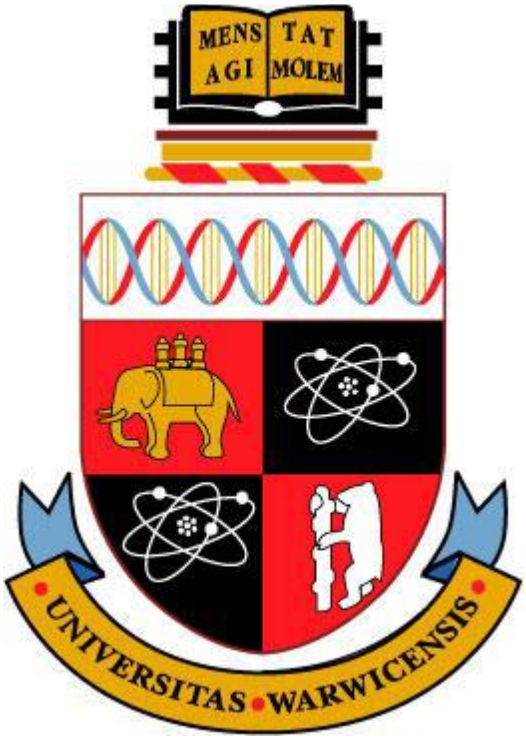

By Gavin Brian Jones

A thesis submitted for the degree for Doctor of Philosophy

Department of Chemistry

University of Warwick

April 2015

Abstract

Organic Thin-Film Transistors (OTFTs) are now surpassing the performance of amorphous silicon based devices which once set the benchmark. State of the art development of OTFTs in active-matrix organic light emitting diodes (OLEDs) for flexible displays has shown the potential for future applications utilising organic materials. This unprecedented advancement of flexible base electronics is now at the forefront of research and development in the electronics industry. Although charge-carrier mobility has now exceeded expectations the processing of organic materials and device functionality is still under intense investigation. Through understanding energetic interactions and charge-carrier properties at the electrode/organic semiconductor (OSC) interface alongside morphological structuring of the thin-film active layer, a more complete understanding of OTFTs can be reached.

Active layers formed of a soluble small molecule blended with a polymer binder have shown significant improvements in OTFT operational performance and device yield due to enhanced morphological effects. This thesis will primarily discuss the implementation of 6,13-bis(triisopropyl-silylethynyl) pentacene (TIPS-pentacene) blended with poly(4-methylstyrene) (P4MS) in the expectation of enhanced device performance offering heightened charge-carrier mobility. Through investigative work conducted in this thesis into self-assembled monolayer (SAM) formation on the source/drain electrodes (**Chapter 3**), changes in the surface properties of the metal contact and the resulting interfacial properties at the electrode/OSC interface are correlated to OTFT performance, alongside morphological changes in the active layer and its relation to charge-carrier conduction in TIPS/P4MS thin-films (**Chapter 4**). Additional studies concerning 2,8-difluoro-5,11–bis (triethylsilylethynyl) anthradithiophene (diF-TES-ADT) are also discussed (**Chapter 5)** relating to similar processing and fabrication conditions.

Declaration

I declare that the experimental work presented in this thesis was carried out between October 2010 and March 2014 under the supervision of Prof. Tim Jones and Dr. Piotr Wierzchowiec. I can confirm that this research project contains an account of the research conducted within this timeframe and that no part of this work has been previously submitted to any academic institution for a higher degree.

All solution preparation, device measurements, and thin-film characterisation was coordinated by the author with the exception of the following experiments detailed below.

- XRD measurements presented in this thesis were measured by Dr. Luke Rochford on samples prepared by the author.
- UPS measurements were conducted by Dr. Luke Rochford and Dr. Marc Walker on their respective UHV analysis systems. Sample preparation and data analysis was performed by the author.
- XPS data was obtained by Dr. Marc Walker and Dr. James Mudd from the Department of Physics, University of Warwick. Sample preparation, data analysis and interpretation were performed by the author.
- SIMS measurements were conducted by Dr. Richard Morris and Prof. Mark Dowsett in the Department of Physics, University of Warwick. Sample preparation was performed by the author.

Acknowledgement

I would like to thank Prof. Tim Jones and Dr. Piotr Wierzchowiec for their supervision and guidance throughout my Ph.D. I would like to thank Merck Chemicals for the incredible opportunity to work within a company at the forefront of organic electronics. The enthusiasm and breadth of knowledge from students and employees at Merck along with the opportunity to annually present my findings has made my learning experience enjoyable and unforgettable. I would like to express my gratitude to all members of staff at the Department of Chemistry and all fellow colleagues within the Prof. Tim Jones group who have come and gone during my time at the University of Warwick. I give huge gratitude to the Engineering and Physical Sciences Research Council (EPSRC) and Merck Chemicals for funding the project.

I would like thank my mother, father and sister for their unfaltering love and support throughout my academic career. Your belief and motivation has given me the drive to achieve and this thesis is dedicated to you.

And finally…I would like to thank Lisa for her unfaltering love and support during my Ph.D. You have been there through it all and I cannot thank you enough.

Table of Contents

List of abbreviations

3,4-DFTP	3,4-difluorothiophenol
4-BTP	4-bromothiophenol
4-FTP	4-fluorothiophenol
a-Si:H	Amorphous Hydrogenated Silicon
AFM	Atomic Force Microscopy
Ag	Silver
Au	Gold
BE	Binding Energy
BG	Bottom-Gate
BG/BC	Bottom-Gate/Bottom-Contact
BTFMBT	3,5-Bis(trifluoromethyl)benzenethiol
CCD	Charge-Coupled Device
CIL	Charge Injection Layer
DFT	Density Functional Theory
diF-TES-ADT	2,8-Difluoro-5,11-bis(triethylsilylethynyl)anthradithiophene
DOS	Density of States
FET	Field-Effect Transistor
FWHM	Full Width Half Maximum
HOMO	Highest Occupied Molecular Orbital
IFT	Interfacial Surface Tension
IP	Ionisation Potential
I-V	Current-Voltage
KE	Kinetic Energy
KP	Kelvin Probe
LCD	Liquid Crystal Display

MI	Diiodomethane
MIS	Metal-Insulator-Semiconductor
ML	Monolayer
MOSFET	Metal Oxide Semiconductor Field-Effect Transistor
OED	Organic Electronic Devices
OLED	Organic Light Emitting Diode
OMBD	Organic Molecular Beam Deposition
OPV	Organic Photovoltaic
OSC	Organic Semiconductor
P4MS	Poly(4-methylstryene)
QCM	Quartz Crystal Microbalance
RFID	Radio Frequency Identification
R&D	Research and Development
RT	Room Temperature
SAM	Self-Assembled Monolayer
SCL	Space-Charge Limited
SECO	Secondary Electron Cut-Off
SiO_2	Silicon Dioxide
SIMS	Secondary Ion Mass Spectroscopy
STM	Scanning Tunnelling Microscopy
TFTFMBT	2,3,5,6-Tetrafluoro-4-(trifluoromethyl)benzenethiol
TG	Top-Gate
TG/BC	Top-Gate/Bottom-Contact
TIPS-pentacene	6,13-Bis(triisopropylsilylethynyl)pentacene
TP	Thiophenol
UHV	Ultra-high Vacuum
UPS	Ultraviolet Photoemission Spectroscopy

UV	Ultraviolet
VBM	Vacuum Band Maxima
XPS	X-ray Photoemission Spectroscopy
XRD	X-ray Diffraction

List of symbols / notations

CB	Conduction Band
E_B	Binding Energy
E_{EA}	Electron Affinity
E_f	Fermi Level
Eg	Band Gap
E_{IP}	Ionisation Potential
E_{SECO}	Secondary Electron Cut-Off
$f(E)$	Fermi-Dirac Population Distribution
g_m	Transconductance
I-V	Current – Voltage
I_D	Drain Current
I_{off}	Off Current of I_D
I_{on}	On Current of I_D
$I_{on/off}$	On/Off Current Ratio
ip	In-plane
k_B	Boltzmann Constant
L	Channel Length
oop	Out-of plane

Φ	Work Function
S	Subthreshold Swing
S_{lin}	Linear Subthreshold Swing
S_{sat}	Saturation Subthreshold Swing
μ_{lin}	Linear Mobility
μ_{sat}	Saturation Mobility
VB	Valence Band
V_{bi}	Built-in Field
V_G	Gate Voltage
V_I	Vacuum Level
V_{on}	Turn-on Voltage
V_T	Threshold Voltage

Chapter 1

Introduction

The field of organic electronics has advanced significantly over the past 40 years due to considerable progress in material development and innovation of technological applications.[1,2] The market for printable and flexible electronics has gained significant momentum over the last decade due to the commercial motivation for lightweight, robust, and low-cost consumer electronics. Plastic electronics is poised to have substantial market dominance, being valued at more than £25 billion by 2020.[3] The current UK stance within the industry has become much stronger to date due to increased availability of government grants and investment funding for new and established organisations, with a drive towards joint ventures with the European and Asian markets.[4,5] The requirement for large-scale, printable organic electronic devices (OED) naturally leads to the development for air-stable, solution-processable materials with high performing characteristics for application specific devices. Significant market growth in plastic electronics has led to increased investment from both industry and research councils to investigate and improve upon these application caveats. With regards to organic thin-film transistors (OTFTs) the continuation towards achieving enhanced performance from solution-processed organic semiconductor (OSC) materials is studied in this thesis, with investigations into their properties and processability. The motivation and aims underlying this thesis are presented in *Section 1.7*.

1.1 A Brief History of Organic Electronics

Its history dates back to the late 19th century where the first reported polycyclic aromatic compounds were shown to display semiconducting charge-transfer complex properties. A significant milestone in organic semiconductors came in the 1970's when conjugated polymers were successfully synthesised to produce insulating or semiconducting polymeric materials. The area of organic semiconductors (OSC) flourished within the next decade with the successful development of organic light-emitting diodes (OLED) and organic photovoltaic (OPV) devices by Tang *et al*.[6] In 1982, the first reported metal-oxide-semiconductor was demonstrated using polyacetylene as the semiconductor and polysilocane as the dielectric materials, where shortly afterwards the first OTFT was developed. The electric current in these devices was significantly low, therefore doping through oxidation of polyacetylene with iodine led to significantly higher conductivity, paving the way for the production of highly conductive polymers.[7] Further development into the synthesis of conjugated polymers with better semiconducting properties became a major aspiration in this field. The technological milestone of developing soluble organic semiconductors sparked the potential for printable electronics with the production of several soluble derivatives of conjugated polymers.

Due to the low charge-carrier mobility of organic semiconductors, OTFTs cannot rival the high switching speeds associated with inorganic semiconductor transistors. Device performance at present for OTFTs has surpassed that of amorphous hydrogenated silicon (a-Si:H) devices which opens avenues for alternative applications of products already recognised within this well-established

industry.[8,9] The charge-carrier mobility associated with OTFTs is several magnitudes lower than crystalline silicon devices, but still retains numerous competitive properties. The strong technological interest in OTFTs stems from its capability to be processed at low temperatures meaning plastic substrates can be utilised, offering flexibility and transparency to device applications. Since no covalent bonds need to be broken or reformed, unlike in the case of inorganic semiconductors, organic semiconductor materials can be manipulated using a small energetic input.[10] The possibility to fabricate organic materials from solution makes them compatible for production using non-conventional printing methods such as inkjet-printing and roll-to-roll processing, leading to the development of a large-area printing technology which offers decreased energy consumption at the manufacturing stage.[11] Organic electronic devices are not expected to rival high-end silicon products but to compliment conventional silicon technology dominant in low-end electronic applications, opening new marketing opportunities for disposable electronics. The introduction of OTFTs into the consumer market has been demonstrated in radio frequency identification (RFID) tags, backplanes (e.g. pixel drivers) for flexible active matrix displays,[12-14] and low cost circuits for sensor applications (e.g. chemical, thermal, and pressure). Electronic-readers (e-readers) have been a major focus for companies such as Plastic Logic Ltd, but its insurgence into the consumer market has been challenging. Corporations such as Samsung and Sony have shown significant advancements in the development of OTFT-driven OLEDs and liquid-crystal displays (LCD). Commercialisation of plastic electronic products has raised the demand on industry to upscale manufacturing of solution-processable molecular materials while maintaining cheap and reliable production, together with good device performance and operational stability. RFID tags have

achieved significant market dominance in retail due to their low-cost high-volume production. RFID tags are inexpensive (ca. < 1 pence) and flexible which has led to their potential replacement of barcodes.

The realisation of large-scale high performing OTFTs has led to research into varied processing methods and device configurations for optimum manufacturing processes and device performance. Along with manufacturing demands, increased understanding of the device functionality in terms of charge injection physics at the metal/organic interfaces and charge transport mechanisms of organic semiconductors requires further clarification. In this thesis, the research motivation is towards enhancing the performance of OTFTs by adopting 6,13-bis(triisopropyl-silylethynyl) pentacene (TIPS-pentacene) and 2,8-difluoro-5,11-bis(triethylsilylethynyl) anthradithiophene (diF-TES-ADT) as the organic semiconductor, with particular focus in improving the charge-carrier mobility of the device. The application of source/drain modification using self-assembled monolayers (SAMs) is implemented to influence the interfacial properties at the metal/semiconductor interface, along with the introduction of small molecule/polymer blends as the active layer (i.e. the semiconducting material) within the OTFT due to the better OSC morphology achievable through this approach.

1.2 Field-Effect Transistors

The first proposed explanation of the field-effect transistors (FET) was patented by Julius Edgar Lilienfeld in 1925.[15] A large amount of research conducted thereafter at Bell Labs by Shockley, Bardeen and Brattain propelled this work forward by producing operational versions of Lilienfeld's work. A significant breakthrough in this field occurred when Kahng and Atalla made the first metal-

oxide-semiconductor field-effect transistor (MOSFET) which now dominates the electronic market.[16] Field-effect transistors are commonly used to amplify analogue or digital signals and can also be used as a switch to direct currents or function as an oscillator.

1.2.1 Principles of Operation

The operation of a field-effect transistor can be described by considering the setup of a parallel plate capacitor where two metal electrodes are separated by a vacuum for insulation purposes (see **Fig.1.1**). Through the application of a voltage difference between the plates a build-up of charges $+Q$ and $-Q$ appears on the electrodes, where the magnitude of charge equates to the capacitance (C_{ox}) of the insulator multiplied by the applied voltage. This leads to the formation of an electric field which is represented in **Fig.1.1(a)**. This electric field is given by the applied voltage divided by the electrode spacing ($E = V/L$). All charges reside on the metal surface upon which mobile electrons are displaced by the electric field leading to current conduction between the contacts.

Replacing one of the electrodes in this scenario with a semiconductor (e.g. *p*-type) leads to a metal-insulator-semiconductor structure, as shown in **Fig.1.1(b)**. The insulating material is typically silicon dioxide (SiO_2) when concerning MOSFETs, which is formed as an oxide layer close to the surface of the crystalline silicon substrate adopted as the semiconductor. A positive voltage (V_G) is applied in this situation to the metal contact which is acting as the gate-electrode. This is an independent contact that controls the flow of electrical current within a MOSFET. The electric field penetrates into the semiconductor exposing negatively charged

acceptors to make up the charge $-Q$ in this circumstance. This leads to the formation of a 'depletion layer' due to the semiconductor being depleted of its equilibrium concentration of hole (aka. electron-hole) charge-carriers. If the voltage is increased further, the electric field becomes stronger which resultantly penetrates deeper into the semiconductor leading to more exposure of the bulk, as shown in **Fig.1.1(c)**. This directly increases the $-Q$ which extends the depletion layer width further into the semiconductor. As the electric field increases it become more difficult to maintain the $-Q$ by enhancement of the depletion region, therefore a more favourable approach of attracting conduction electrons into the depletion region leads to the formation of a thin electron layer at the semiconductor/insulator interface which is termed the 'channel region'. At this point, the electric field is largely enhanced due to the gate-electrode/channel region capacitor being strongly biased, repelling majority carriers (holes) and attracting minority carriers (electrons). This formation of an electron-rich layer formed within a *p*-type semiconductor (i.e. a material with a majority of hole-carriers) is called an 'inversion layer'. The same effect occurs in *n*-type semiconductors (i.e. a material with a majority of electron-carriers), whereby a layer rich with hole charge-carriers is forms. Through increasing the strength of the electric field, first a depletion layer is formed, and then an inversion layer occurs at the insulator/semiconductor interface, which happens only when the applied voltage exceeds a material dependent parameter called the threshold voltage (V_T). The threshold voltage is defined as the gate voltage from which the conduction channel starts to form, hence, the voltage required to overcome the potential barrier to conduction in the device. Permitting that the applied voltage is higher than the threshold voltage ($V_T > V_G$) any increase in the electric field leads to more electrons

in the inversion layer, in which its rate is determined by the capacitor relationship $Q = C_{ox}(V_G - V_T)$.

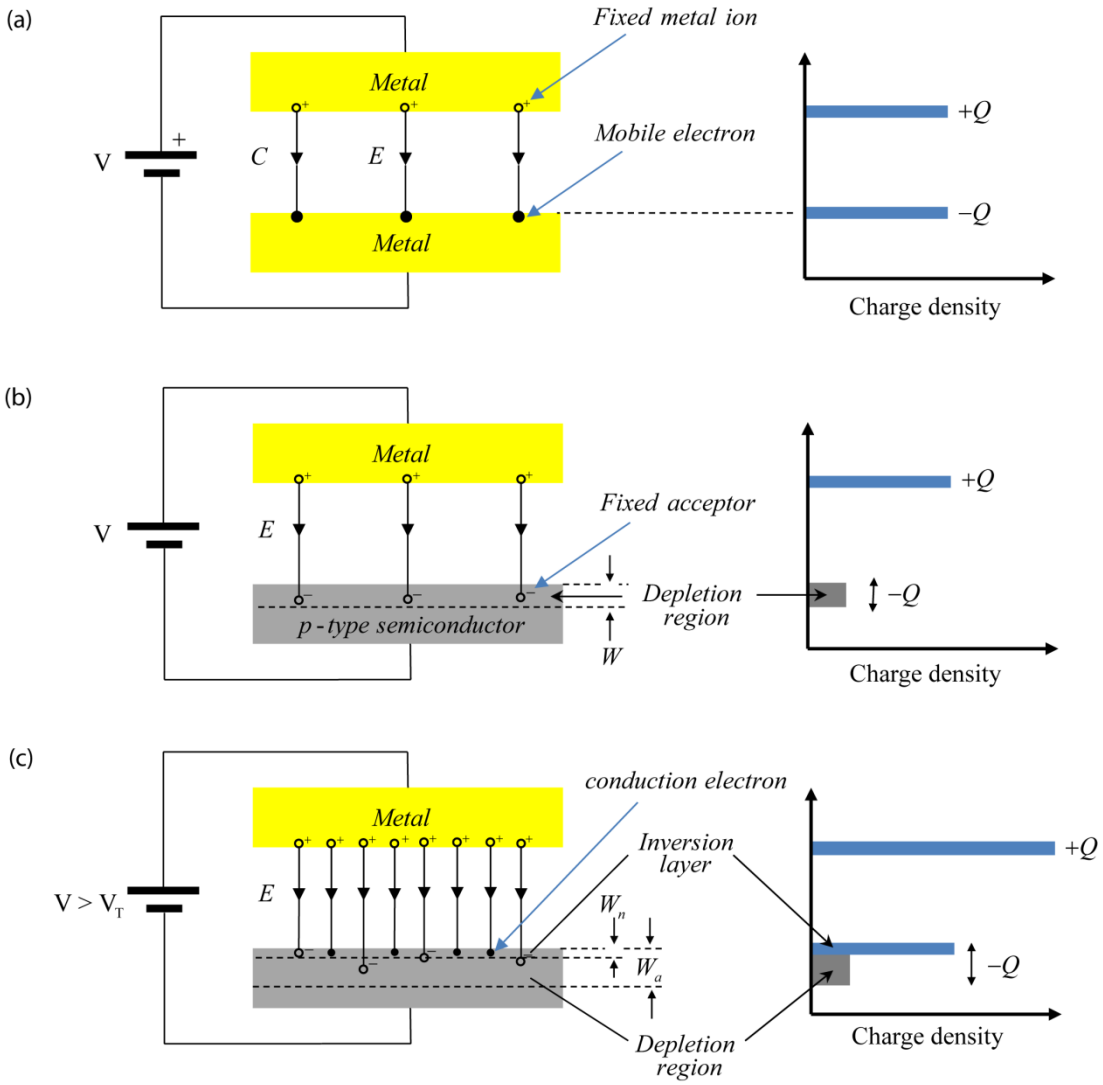

Figure 1.1: (a) Metal-air-metal capacitor, (b) Field penetration into a *p*-type semiconductor, (c) Inversion layer formed near the surface of the semiconductor when $V > V_T$ where there are now conduction electrons.

In an actual MOSFET configuration, the inversion layer formed at the insulator/semiconductor interface is described as the 'conducting channel'. This forms between two ohmic contacts known as the source and drain. Traditionally in

crystalline silicon MOSFETs, the source and drain are doped to form two back-to-back *p-n* junctions. This arrangement stops the flow of current in both directions in the channel until the inversion layer is formed, which becomes the same doping type as the diffused source and drain electrodes. This results in a short-circuit between the back-to-back diodes formed amid the source and drain contacts, producing a resistor whose resistance is determined by the sheet charge density at the surface.[10] The charge-carrier density formed within this channel is controlled by the voltage applied to the gate-electrode which is capacitively coupled across the gate-dielectric. The gate-electrode effectively controls the conductivity of the channel and hence the current which flows through it. At a given gate voltage, a larger bias applied between the two contacts either side of the conducting channel, called the source/drain voltage (V_{DS}), causes the field generated by the gate to be diminished. This reduces the charge density within the conducting channel in close proximity to the drain. When the potential close to the drain is equal to the threshold voltage a resultant effect termed 'pinch-off' occurs, where the current in the device ceases to increase with increasing V_{DS} and enters a region of operation called 'saturation'.

The operation of an OTFT behaves substantially different to that of a MOSFET but overlaps when considering their I-V characteristics and physical parameters. The operation principles of OTFTs will be introduced in the following section.

1.3 Organic Thin-Film Transistors (OTFTs)

A thin-film transistor (TFT) is subtly different when compared to conventional field-effect transistors, where thin layers of the electrode, semiconductor, and dielectric materials are deposited. Thin-film transistors have

been around for several decades within the inorganic transistor community with amorphous silicon and polycrystalline silicon dominating this field. The performance of a TFT is strongly dependent on the chemical and structural properties of the semiconductor layer, where critically the degree of crystallinity determines the charge-transfer properties of the device. Amorphous silicon and polycrystalline silicon are typically adopted for display and sensor arrays due to the large areas required which restricts the use of crystalline silicon for these applications. This results in TFT with slow switching speeds due to the low conductivity properties of these materials.

1.3.1 Principles of Operation

A field-effect transistor (a.k.a. thin-film transistor) is a three terminal planar device in which the current through the semiconductor, connected to two terminals (source and drain), is controlled by a bias (V_{GS}) applied to a third terminal (the gate) that creates an induced electric field through the dielectric of the device (see **Fig.1.2**). The gap between the source/drain electrodes is defined as the channel region where the conductance of the device depends on the electrical length of the channel. Conventionally charge-carriers are swept across the channel region parallel to the surface of the gate-dielectric, represented by an arrow in **Fig.1.2(a)**. The dimensions of the channel are defined by its length (L), which runs in the direction of current travel, and width (W), which is in the plane of current flow perpendicular to the channel length, shown in **Fig.1.2(b)**. The physical length of the channel is fixed, but its effective electrical length can be varied by the application of a voltage to the gate-electrode. The separation of the gate electrode from the channel region by

the dielectric layer establishes a capacitor arrangement analogous to the gate

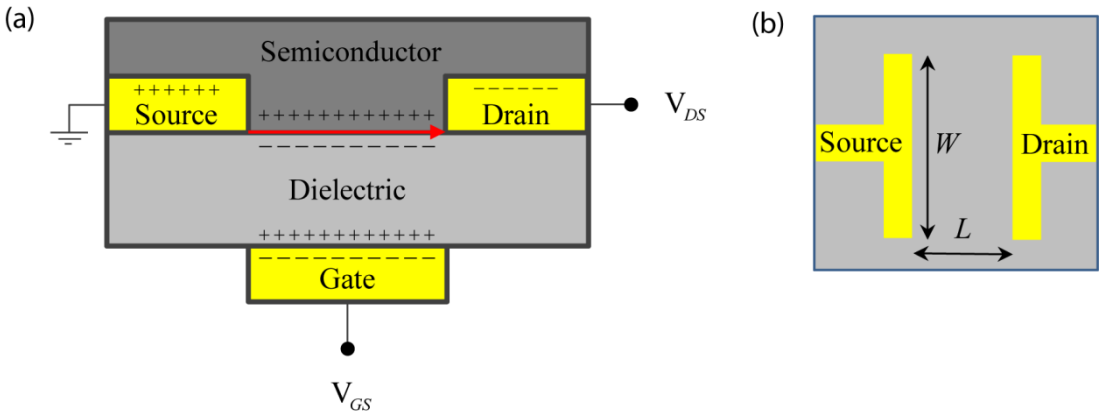

Figure 1.2: (a) Scheme of a thin-film transistor (*p*-channel device) and designated applied voltages $(V_G < 0)$. (b) Aerial view of channel dimensions. L = channel length; W = channel width; V_{DS} = drain voltage; V_{GS} = gate voltage.

capacitor previously described for the MOSFET, where the insulator aids in the creation of an electric-field across the semiconductor. This field-effect causes the formation of an accumulation region, when a voltage is applied between the source and drain (V_{DS}), where charges gather at the dielectric/semiconductor interface forming the resultant conducting channel.[9] This causes majority carriers to drift from the source to the drain, controlling the conductance of the channel between the two respective electrodes by the application of an external electric field. The control of the source/drain current (I_{DS}) via the third terminal gate electrode has resulted in their widespread use as switches, where small changes in V_G can cause large variations in I_{DS}. The corresponding biases are applied to the gate electrode and commonly to the drain electrode with the source grounded. Conventionally the source is the charge-injecting electrode, providing the electrical current, and the drain is the charge-extracting electrode. The source contact is always more negative

than the gate contact when a positive V_{GS} is applied (i.e. electrons are injected into the semiconductor) and more positive than the gate electrode when a negative V_{GS} is applied (i.e. holes are injected into the semiconductor).

Two distinct modes of operation exist in a TFT called the linear regime and saturation regime. The behavioural features of each regime can be observed in the output curve (I_{DS} *vs.* V_{DS}) where varying the drain voltage at a constant gate bias can give information on the switching performance of the FET. This will be used to demonstrate the operational characteristic of the TFT. When no bias is applied between the source-drain ($V_{DS} = 0$) the carrier concentration within the channel is zero. A small source-drain voltage is applied ($V_{DS} \ll V_{GS}$) which leads to a linear gradient of charge density (i.e. equal and opposite charge stored at the gate/dielectric and dielectric/semiconductor interface). The voltage at the source and drain is nearly identical, therefore the electrical potential along the channel is constant (see **Fig.1.3(a)**). The current flowing through the conductive channel, I_{DS}, is directly proportional to V_{DS} and V_{GS}, where the potential across the channel length increase linearly from the source to drain, thus obeying Ohms law. This mode of operation is termed the linear regime and the current can be described by **Eq.1.1**, where in the linear region $V_{DS} \ll V_{GS} - V_T$.

$$I_{DS} = \frac{W}{L}\mu_{lin} C_i \left(V_{GS} - V_T - \frac{V_{DS}}{2} \right) V_{DS} \qquad \textbf{Equation 1.1}$$

Here, C_i is the capacitance per unit area of the dielectric (F/cm^2) and μ_{lin} is the field-effect mobility in the linear regime.[18] As the drain voltage is increased further until its value is equal to $V_{GS} - V_T$, the electrical potential within the channel falls to zero (see **Fig.1.3(b)**). The channel is now 'pinched-off' and the drain current

saturates, therefore charge density across the channel drops to zero due to the formation of a depletion region close to the drain electrode.[19] This is due to the local potential ($V(x)$) and the gate voltage falling below the threshold voltage. The increasing drain voltage causes the accumulated charge density to decrease from the source to drain due to lowering of the voltage drop at the drain, while the voltage drop at the source remains the same. The drain current is now independent of the drain voltage and increases sublinearly up to 'pinch-off'. This mode of operation is termed the saturation regime and its current can be approximated by **Eq.1.2**, where in the saturation regime $V_{DS} \geq V_{GS} - V_T$.

$$I_{DS} = \frac{W}{2L} \mu_{sat} C_i \left(V_{GS} - V_T \right)^2 \qquad \textbf{Equation 1.2}$$

Here, μ_{sat} is the field effect mobility in the saturation regime. Charge-carriers can still flow through the channel due to the comparatively high electric field in the narrow depletion region. This leads to a space-charge limited (SCL) saturation current ($I_{D,sat}$) which is swept from the point of pinch-off to the drain electrode.[20] Further increasing V_{DS} cause an expansion of the depletion region with no substantial increase in I_{DS}, where the current will saturate at a level I_{OFF} (see **Fig.1.3(c)**).

Throughout this work only *p*-channel devices are used, therefore a negative gate bias is applied. From an energetic point-of-view, a voltage drop occurs near the dielectric/semiconductor interface, where the electronic equilibrium is disrupted causing the E_F of the metal and semiconductor to realign via a redistribution of charge at the interface (i.e. band bending).

A major difference in the operation of a TFT is the device operates in an accumulation regime, where the conducting channel is formed by the accumulation

of majority carriers at the dielectric/semiconductor interface, compared to an inversion layer described previously for MOSFETs. Due to the absence of a depletion region in a TFT, which is essential in MOSFETs to isolate the device from the substrate, the equations used to model crystalline silicon FETs are also

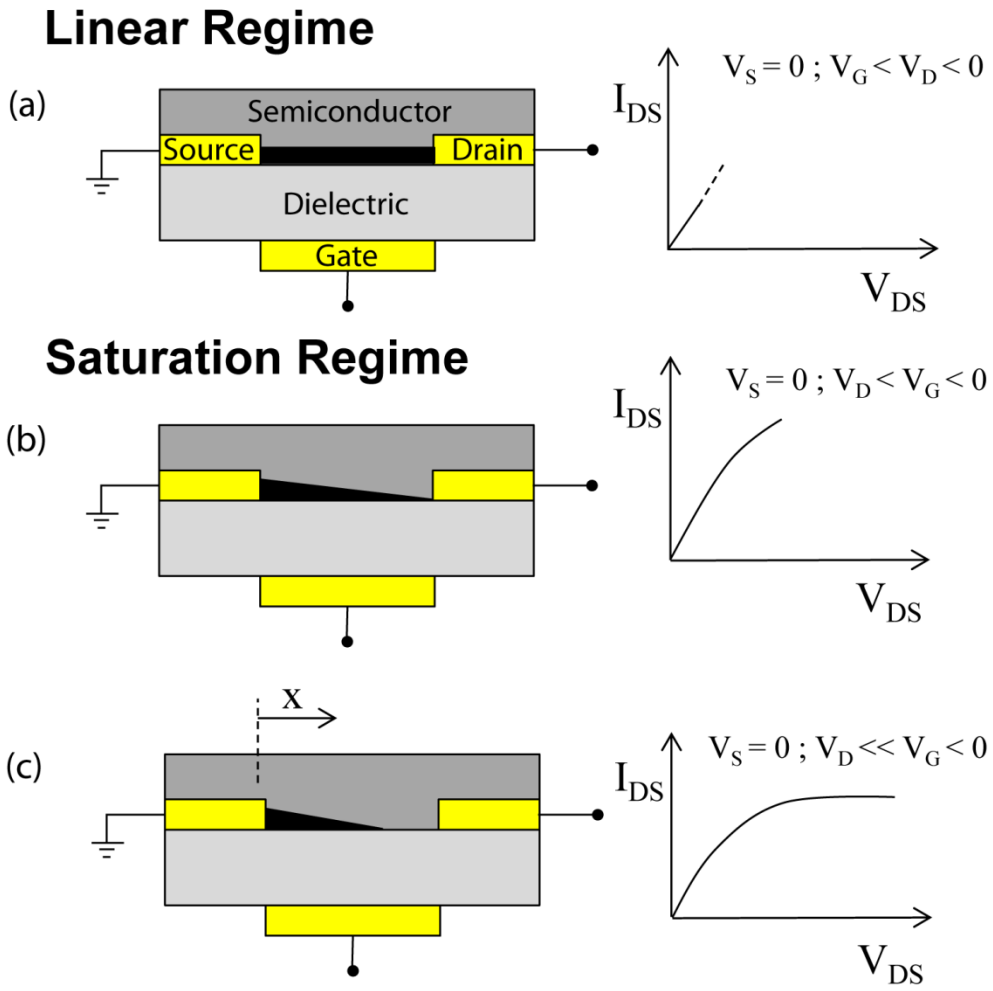

Figure 1.3: Schematic and operating regimes of a field-effect transistor: (a) linear regime, (b) saturation regime at 'pinch off', (c) saturation region beyond 'pinch-off'.[20] The channel region is represented by the shaded area between source and drain.

considered when describing TFT operation. The current-voltage equations are therefore oversimplified for each regime when adopted for TFTs with several

assumptions not usually fulfilled in organic devices. The main assumptions are: the field-effect mobility is taken as being constant, and a gradual channel approximation is presumed (i.e. the electric-field along the channel is smaller than that across it, leading to voltage variations along the channel). This latter assumption is only valid when the distance between the source and drain is much larger than the thickness of the gate-dielectric.

All field-effect mobility values stated in this thesis were extracted using the following equations taken for standard MOSFET devices, which in the linear (**Eq.1.3)** and saturation (**Eq.1.4**) regimes are:

$$\mu_{lin} = \frac{L}{WC_i V_{DS}} \frac{\partial I_{DS}}{\partial V_{GS}} \qquad \textbf{Equation 1.3}$$

$$\mu_{sat} = \frac{2L}{WC_i} \left(\frac{\partial \sqrt{I_{DS}}}{\partial V_{GS}} \right)^2 \qquad \textbf{Equation 1.4}$$

The field-effect mobility is used as a figure of merit for assessing the efficiency of the OTFTs device performance and only be taken as an estimate. In regards to this, it must be noted that mobility extraction is complex due to the presence of physical artefacts and over-simplified models leading to erroneous values. These equations assume a constant mobility and ignores the gate-voltage dependence of mobility which is often the case in OTFTs and similarly in a-Si:H transistors. All mobility values in this thesis are to be taken as the most representative result and used as comparative assessment of a range of devices.

The electrical performance of the TFT is dependent on several factors, such as, the capacitance of the dielectric layer; the semiconductor material (e,g. OSC, semiconducting oxide material); and the properties of the source and drain contact.

The electric current of a TFT flows inside the semiconductor layer in close proximity to the dielectric, therefore the structural and electronic properties of both materials, as well as the interfacial properties at the dielectric/semiconductor interface can influence the electrical performance of the transistor. The growth and crystalline order of the semiconductor at the dielectric/semiconductor interface can strongly dictate the electrical performance of the transistor. The first few molecular layers of the organic semiconductor at this interface play a pivotal role in formation of the conducting channel due to the vast majority of mobile charges drawn here due to the gate electric field. Surface fluctuations associated with roughness can influence charge transfer as they can serve as scattering sites for charge-carriers. The adopted molecular orientation of the semiconductor is also an important factor in regards to charge-transport through the material, where in the case of TIPS-pentacene its arrangement perpendicular to the substrate offers greater diffusion, whereas pentacene arranges with its highest mobility parallel to the substrate. Controlling the growth behaviour of the OSC is usually achieved by functionalising the underlying surfaces with SAMs for preferential structuring of the thin-film. The OSC forms an interface with the source/drain contacts and the dielectric depending on the device architecture. With regards to the dielectric/OSC interface, SiO_2 is commonly used as the gate dielectric or can be replaced with an organic polymeric insulator which can be modified with alkylsilanes. Treatment of hydroxylated surfaces with octadecyltrichlorosilane (OTS) or hexamethyldisilazane (HDMS) helps to remove hydroxyl groups from the surface which impede favourable growth modes for the organic semiconductor. These factors are of key importance for good electrical characteristic performance when operating TFTs. Additionally, the nature of the electrode and its interfacial properties with the semiconductor are important factors

for charge injection and its influence on electrical current within the TFT. The contacts of the TFT are commonly engineered to have good electrical access to the channel but injection phenomenon in organic/metal is not fully understood.

Three major metrics are used to determine the performance of an organic semiconductor. Firstly, field-effect mobility (μ_{FE}), which is a measure of how fast charge-carriers can move (i.e. their drift velocity, υ_d) under an applied electric field (E):

$$\mu_{FE} = \frac{\upsilon_d}{E} \qquad \textbf{Equation 1.5}$$

Mobility is a macroscopic quantity which is intimately related to the intermolecular and intramolecular charge transport which is a material specific parameter, therefore the molecular ordering of the semiconductor layer has a strong influence on this parameter as well as the transistor design (e.g. device geometry, structural dimensions). Charge-carrier mobility is also influenced by the thickness of the dielectric and the materials of different layers in the device.[21] Two other key metrics are the $I_{on/off}$ ratio and V_T. The $I_{on/off}$ is a measure of the maximum current when the device is on to when the device is off, which are divide by each other to give a ratio. It is essential this ratio be high in value (e.g. 10^5 - 10^8) and correspondingly low leakage current during operation. The I_{off} is usually higher in TFTs compared to MOSFETs which is problematic when used as switches due to unwanted leakage currents. This inherent effect is commonly observed in OTFTs due to parasitic capacitance effects present between neighbouring transistors (i.e. cross-talk) but can be reduced by Corbino-type structures or device isolation by dry or wet etching. High I_{off} currents can also occur due to doping or degradation of the OSC.

The off-current can also be improved by isolating the device, minimising parasitic effects, and reducing the overlap between the gate-electrode and the source/drain contacts. MOSFETs overcome such an issue by the presence of a blocking *p-n* junction near the source and drain contacts which prevent current flow when the channel is absent. The thickness of the OSC primarily affect the on-current (I_{on}) but can cause undesirable increases in I_{off} if too thick and a lowering in mobility (e.g. > 100 nm).[22]

The threshold voltage is essentially the voltage required to turn the device on and is desirable for this to occur when I_{off} is at its lowest value and occurring close to a gate bias of 0 V. This is important for minimising power requirements (i.e. low operation voltages) and improving switching speeds. The threshold voltage depends on the bulk and interfacial states of the dielectric, where shifts in threshold voltage are a result of interfacial stresses, and metastable defects created in the semiconductor layer under an applied gate bias. In summary, necessary prerequisites for expectable OTFT performance are high mobility, low threshold voltage, large on/off current ratio, and steep sub-threshold slope. Additionally, minimal hysteresis and good long-term operational stability are desirable.

The device performance of an organic transistor is severely limited by the intrinsically low charge-carrier mobility of organic semiconductors compared with crystalline silicon-transistors. Single-crystal mobilities between 5 - 40 $cm^2\ V^{-1}s^{-1}$ have been reported for organic semiconductors but solution-processed thin-films typically display much lower mobilities.[9,23-25] This is primarily due to the presence of disordered film formation, with both polycrystalline and amorphous phases present throughout the layer. This disorder is known to severely limit charge-carrier

mobility due to insufficient conductive pathways. The evolution of *p*-channel and *n*-channel charge-carrier mobility for evaporated and solution based organic materials in OTFTs are shown in **Fig.1.4**. Ground-breaking research by Yuan *et al.* has achieved unprecedented mobility values of up to 43 cm^2 $V^{-1}s^{-1}$ for solution processed 2,7-dioctyl[1]benzothieno[3,2-b][1] benzothiophene (C8-BTBT) blended with polystryrene (PS).[26] This work adopts an off-centre spin-coating method which results in highly aligned anisotropic crystals compared with conventional spin-coating. This work strongly reiterates the point that device performance is dictated by charge transport in the semiconductor, which is related to the field-effect mobility, in addition to the charge injection at the contacts which is related to the contact resistance.

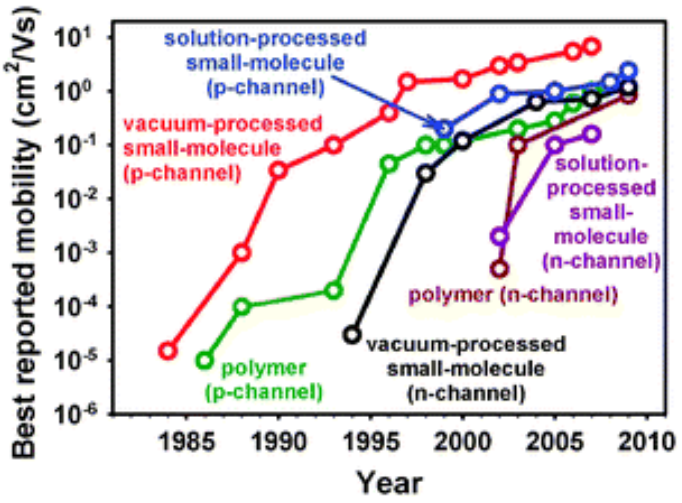

Figure 1.4: Evolution of OTFT performance in terms of charge-carrier mobility in both *p*-channel and *n*-channel devices for vacuum-processed and solution-processed organic semiconductors.[27]

A brief discussion of charge transport mechanisms used to describe charge-carrier behaviour in organic semiconductors will now follow.

1.4 Semiconductor Theory

An individual molecule, consisting of two hydrogen atoms, possesses a molecular orbital formed by the overlap of the discrete atomic orbital of each hydrogen atom. This molecular orbital consists of a bonding (Ψ_B) and anti-bonding (Ψ_A) orbital, which are discrete energy levels, separated by a forbidden energy gap referred to as the bandgap (E_G). A schematic representation of this for a carbon atom and its six electrons is shown in **Fig.1.5**. The molecular orbitals are filled according to the Pauli principle, with electrons occupying the lowest energy orbitals first, with each consisting of two electrons of opposite spin as indicated by arrows for carbons electron configuration ($1s^2$ $2s^2$ $2p^2$). The hybridisation of carbon is discussed in *Section 1.5.1*.

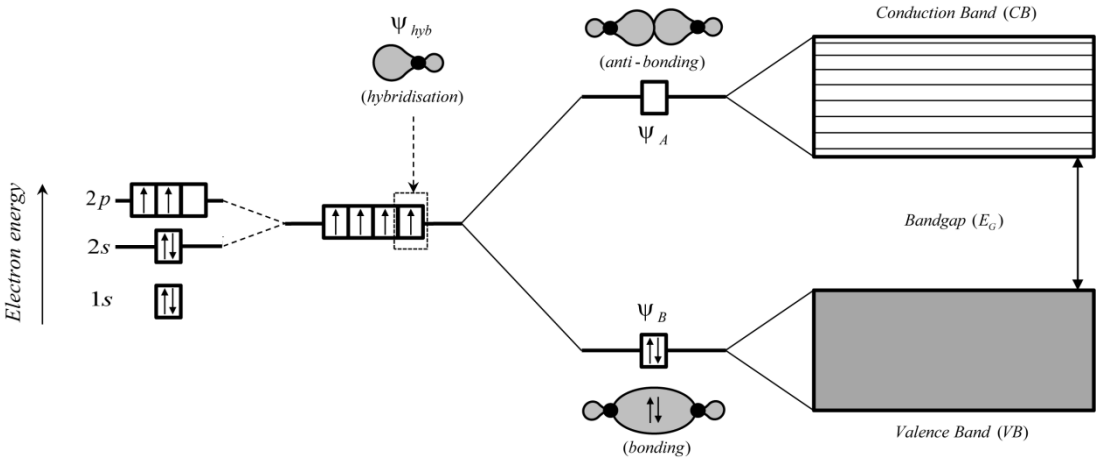

Figure 1.5: Hybridisation of energy bands for carbon into anti-bonding (Ψ_A) and bonding (Ψ_B) orbitals separate by a bandgap (E_G).[28]

The electronic characteristics of metals, semiconductors and insulators are explained in terms of their energy band formation, which relate directly to the relative positions of their Ψ_B and Ψ_A, which are also called the valence band (VB)

and the conduction band (CB), respectively. In a metal, various energy bands overlap to give a single energy band that is only partially full of valence electrons (i.e. no energy gap exists). This positions the Fermi level (E_F) of the metal at the band edge where the CB and VB overlap. At absolute zero (T = 0 K), all energy levels up to the E_F are full (i.e. no electrons have enough energy to exist above this point). The probability of finding an electron at an energy level (E) is explained by the Fermi-Dirac function:

$$f(E) = \frac{1}{1 + \exp\left(\frac{E - E_F}{k_B T}\right)} \qquad \textbf{Equation 1.6}$$

where E_F is the Fermi energy, and $k_B T$ refers to the thermal energy, k_B is the Boltzmann constant, and T is the temperature. The $f(E)$ describes the population distribution of electrons in the solid as a statistical representation. The Fermi level or also termed as the Fermi Energy is defined as the energy for which the probability of occupancy $f(E_F)$ equals ½.

The conductivity of a semiconductor (σ) is dependent on the electron and hole concentration which can be represented by the following equation:

$$\sigma = en\mu_e + ep\mu_h \qquad \textbf{Equation 1.7}$$

where n and p are the electron and hole carrier concentrations in the conduction band and valence band, respectively, e is the electron charge, and μ_e and μ_h are the electron and hole drift mobilities, respectively. A pure intrinsic semiconductor (i.e. no impurities or crystal defects) has equal electron and hole concentrations due to thermal generation across E_G, where the E_F sits in the middle of the energy gap

(see **Fig.1.6(a)**). Extrinsic semiconductors are produced through the introduction of dopants to the crystal lattice (e.g. Si or Ge) in a result to ensure the concentration of one type of charge-carrier is largely in excess of the other. By adding pentavalent impurities which have a valency of more than four, it is possible to obtain a semiconductor in which the electron concentration is much larger than the hole concentration ($n > p$). Doping the crystal lattice with Group V elements from the Periodic Table (e.g. As, P, Sb) aids in donating additional electrons into the conduction band, which subsequently moves E_F closer to the conduction band energy level, E_C, leading to the formation of an *n*-type semiconductor (see **Fig.1.6(b)**). It is also possible to have excess holes in the valence band, by

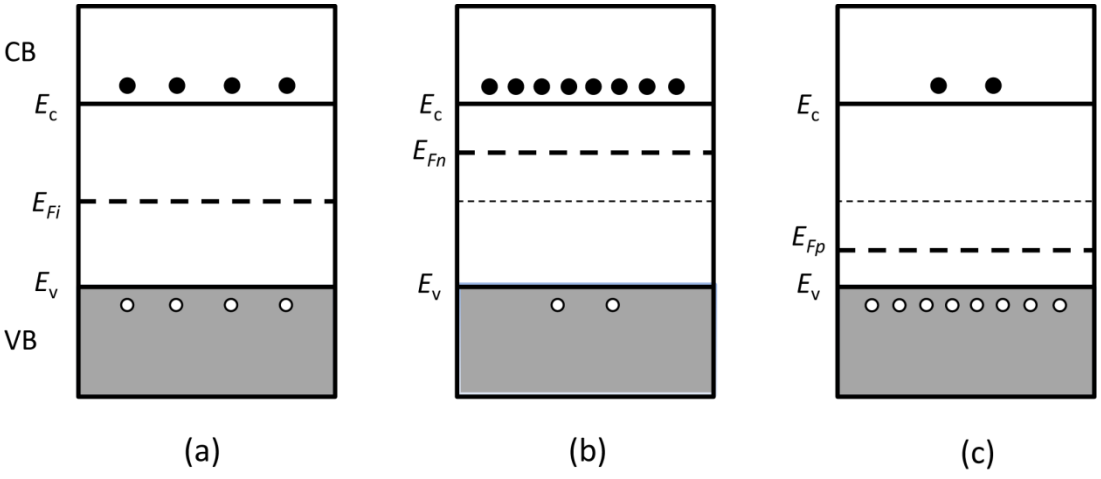

Figure 1.6: Energy band structure for (a) intrinsic, (b) n-type, (c) p-type extrinsic semiconductors.

adding impurities that remove electrons from the valence band and thereby generate holes. The addition of trivalent impurities specific to Group III of the Periodic Table (e.g. B, Al, Ga, or In) which have a valency less than four can lead to an excess of

holes over electrons. In this case the E_F moves closer to the valence band energy level, E_V, and is defined as a *p*-type semiconductor (see **Fig.1.6(c)**).

The electronic structure for an organic semiconductor can be represented by the energy level diagram in **Fig.1.7**. The vacuum level is the energy level where both the potential energy and kinetic energy of the electron are zero. It defines the energy level where the electron is just free of the solid. The electron affinity (χ) is the energy required to remove an electron from E_C to the vacuum level. The ionisation potential (or ionisation energy, E_I) is the energy required to remove an electron from the edge of the valence band to the vacuum level. The energy required to move

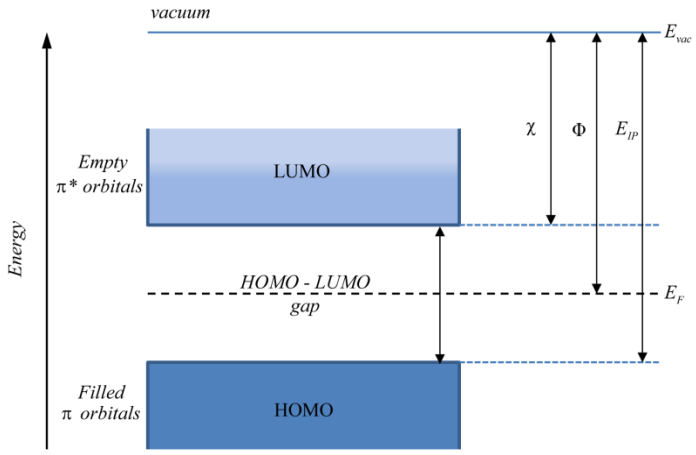

Figure 1.7: Energy band diagram of an organic semiconductor.

an electron from the E_F to the vacuum level where the electron becomes free from the solid is called the work function (Φ). The continuous band structuring of inorganic semiconductors have their energy levels defined as the valence band and conduction band whereas the electronic structure of organic semiconductors are defined by frontier molecular orbitals associated with the molecular overlap of

π-bonding orbitals. The equivalent energy levels (or orbitals) for organic semiconductors are, the highest occupied molecular orbital (HOMO) which is associated with the π-bonding orbital and analogous to the valence band (i.e. filled π-orbitals), where the lowest unoccupied molecular orbital (LUMO) is associated to the higher energy π-antibonding orbital and analogous to the conduction band (i.e. empty π-orbitals). Additionally, the HOMO-LUMO gap is analogous to the E_G. Conjugated organic solids behave more like insulator than semiconductors due to poor charge transport in these materials. This is due to the non-continuous electronic band structure associated with organics which leads to less efficient transport. This difference in band structure results in weaker electronic coupling between molecules leading to relatively narrow bandwidths for both HOMO and LUMO levels.

1.5 Organic Semiconductors (OSCs)

Organic semiconductors can generally be categorised into two major classes: small molecules (low molecular weight and short carbon chain molecules) and polymers (high molecular weight and long carbon chain molecules). A large majority of polymers and small molecules are miscible in a number of common organic solvents, whereas polyacenes can be sublimed due to their poor solubility. Resistive heating of small molecules under vacuum conditions is very advantageous but is critically application dependent, whereas long chain polymers decompose under such high thermal processing conditions. In order for organic materials to be semiconductors they must possess a rich pi (π) electron system (i.e. molecules composed of sp^2 hybridised carbons like aromatics) and be capable of charge transfer effectively upon excitation.[29] These low energetic π-electrons can be easily dislocated unlike sigma (σ) bonds.[29] Organic semiconductors of molecular crystals

are formed by weak intermolecular bonds between molecules, commonly Van der Waals interactions, π-π interactions, hydrogen bonding, or other weak interactions.[17] These characteristics of organic semiconductors lead to more pronounced polaron formation and stronger electron lattice interactions. Typical E_G for insulating organic materials are in excess of c.a. 4 - 5 eV, where semiconducting highly conjugated organic materials are between 1 - 3 eV.[29]

1.5.1 Charge Transport in Organic Semiconductors

The family of acene-based semiconductors with linear-fused ring structuring has been widely adopted in OTFTs due to their planarity and rigidity which gives excellent stacking properties. Deposition techniques (e.g. sublimation or solution-processing) commonly lead to polycrystalline films at room temperature which provide $\pi - \pi$ overlapping between neighbouring molecules which governs the charge-carrier transport through the layer. The exact structural ordering is dependent on the influence of the underlying substrate and deposition technique adopted. π-stacking between organic semiconducting molecules is a necessity for ensuring high mobilities, which is critically dependent on strong electronic coupling between molecules, and therefore associated with excellent overlap between the π-systems on adjacent molecules. The precise nature of the π-stacking, rather than solely the presence of π-stacking interactions is also a key factor. This has been observed in cases where molecules with effective wave function overlaps, but without extensive π-stacking, have shown high mobility and vice versa. Work conducted by Brédas *et al*. has shown that spatial overlap of orbitals to determine coupling must be considered alongside the phase relationships between the orbitals of each molecule.[30]

Carbon exists under three different hybridisation configurations, sp, sp^2, and sp^3 (see **Fig.1.5**), which makes this element unique compared with silicon or germanium. In the latter of these configurations, sp^3, each carbon atom is connected to its neighbours by four strong σ-bonds that point to the four verges of a tetrahedron.[10] Due to the strong nature of σ-bonds this leads to large distance between the bonding and anti-bonding energy levels (HOMO and LUMO, respectively). As a consequence of this it leads to carbon-based materials being electrically insulating but a lot more versatile than silicon. Organic molecules that are defined as semiconducting utilise the sp^2 hybridised carbons which provide conjugation throughout the organic material. In this instance, each carbon is linked to its neighbour by three sigma (σ) bonds resulting in the hybridisation of 2s, $2p_x$, and $2p_y$, while the remaining $2p_z$ orbital forms a π-bond (which does not contribute to the sp^2 hybridisation). Reduction in E_G through use of the sp^2 orbitals makes carbon semiconducting at non-zero temperatures. By comparison, σ-bonds are stronger than π-bonds due to the lower energy levels associated with the π-orbitals due to these orbitals being further away from the positively charged nucleus. The strong σ-bond framework holds the molecule together, where the weak π-bond has little influence on the molecule structure. In acene or polyacene compounds such as benzene, the π-orbitals become delocalised, due to its conjugated structure, forming a π-system which extends throughout the molecule. The delocalisation of π-electrons is a result of *p*-orbitals overlapping, allowing the movement of such charges from one bond to another, and thus extending across the whole molecule. This type of organic materials is termed as being π-conjugated, where molecules with neighbouring carbon atoms which are sp^2 hybridised form delocalised clouds of π-electrons. In essence, conjugation is present when a polymer or small molecule has alternating

single and double bonds between its carbon atoms. A single carbon bond $(C-C)$ possesses a σ-bond, where both carbon atoms give-up an electron from their respective *s* orbitals. This forms localised electrons which are attached to the two carbon nuclei. A double bond $(C=C)$ consists of both a σ-bond and a π-bond, whereby the π-bond involves the direct sharing of electrons between the *p* orbitals of the two atoms. The degree of conjugation, with regards to polyacenes, effects E_G between the π-π* transition states leading to smaller HOMO-LUMO gap for larger conjugated networks (e.g. benzene: E_G = 6.0 eV; pentacene: E_G = 2.1 eV).[10] The bandgap of conjugated polymers are within the energy range of 1 - 4 eV. The extension of polyacenes from linear fused benzene rings is limitless in its molecular design. The increase in mobility measured for pentacene (five fused benzene rings) compared with anthracene (three fused benzene rings) is related to the extension of the π-conjugation system. Increasing the conjugation length beyond five benzene rings leads to very unstable organic molecules which are problematic from a synthetic and device performance perspective. In terms of molecular arrangement, both organic molecules display similar packing motifs but the higher mobility associated with increasing polyacenes is related to the lower reorganizational energy and improved intermolecular interactions.[31]

To understand the behaviour of charge transport in conjugated molecules we must consider electron transfer between molecules. π-bonds have significantly less overlap compared with σ-bonds, and more specifically orbital overlap between conjugated molecules is low. This leads to complex issues when explaining charge transport in these organic materials. Explaining charge transport requires consideration of different charge transport models to fully encapsulate the

complexity of this field. The theory of charge transport in thin-films is additionally challenging as charge transport occurs at the interface close to the dielectric/organic semiconductor where interface defects and trap-sites can influence conduction. For sake of brevity only the foremost charge-transport theories will now be discussed.

1.5.1.1 Band Transport

The mechanism for charge transport can be explained in terms of band formation which occurs between neighbouring atoms. The discrete energy levels of individual atoms become closely packed within a solid, leading to the formation of energy bands across interacting atoms. This band formation is ideal for conduction but is limited by the likelihood that these bands are filled with electrons. The probability of finding an electron in an energy state (E) can be explained by the Fermi-Dirac statistic (see **Eq.1.6**). In semiconducting materials, the small bandgap, E_G, can be bridged by thermal excitations which is seen in the Fermi-Dirac function whereby, as the temperature increases, $f(E)$ extends into higher energies resulting in the increase of carrier-mobility. Conduction in crystalline semiconductors such as silicon is explained by band transport where carriers move through delocalised states.

Due to thin-films of solution processed organic semiconductors being highly disordered or amorphous, adopting a band transport model is erroneous due to the presence of grain boundaries and defects within the structural disorder of these films. Band like transport has been reported for some highly crystalline (i.e. single crystal) organic semiconductors.[32] This argument has been put under scrutiny for acene-based materials where at least for temperatures above $100\ \mathrm{K}$, the mean free path falls below the atomic distance between molecules in single crystals. This is not

consistent with diffusion limited transport when considering the Drude model which questions the validity of this transport model.

1.5.1.2 Hopping Transport

Hopping transport models are useful in explaining the behaviour of disordered materials such as polymers which have delocalised states.[33] Weak intermolecular interactions and amorphous structuring of conductive polymers result in poor charge transport. In the instance of amorphous or organic semiconductors with low conductivity, this model is invalid due to mean free path falling below the distance between molecules; therefore the thermally activated tunnelling of charge-carriers, described as 'hopping' is the dominant carrier transport mechanism amongst localised states.

It is generally accepted that at low temperature, band-like motion could be used to describe charge transport in single crystal organic semiconductors (i.e. defect free films). This means charge-carriers are delocalised over small chains or free chains and the hole and electron mobilities are governed by the total valence and conduction bandwidths which are built from interactions of the HOMO and LUMO levels.[17] This has been shown for highly pure single crystals of small molecules such as rubrene which has one of the highest intrinsic mobilities of c.a. 15 $cm^2 V^{-1}s^{-1}$.[18] At higher temperatures (e.g. room temperature) the charge transport can be described by a polaronic hopping transport process where charge-carriers are expected to be localised over a single molecule unit. Charge-carriers are transported between localised states by polaron-assisted tunnelling, a process which is thermally assisted and scattered at every step. The hopping mechanism (i.e. conduction) is assisted by phonons which are formed from thermally induced lattice scattering,

whereas crystalline inorganic semiconductors are limited by phonon scattering due to their delocalised transport. Due to most organic electronic devices being operated at room temperature, impurities and defects are inevitable, therefore a charge hopping model is commonly adopted with a mobility boundary between 0.1 - 1 $cm^2 V^{-1}s^{-1}$ for associated localised transport. Localised transport is a common characteristic of organic conjugated materials, due to the strong electron-phonon coupling and the effect of splitting energy levels.

Alongside the temperature dependence behaviour of charge mobility in organic materials, the mobility of organic semiconductors become field dependent at high electric field strengths (e.g. $>10^5$ V/cm). This field-dependence of mobility can be explained in terms of the Pool-Frenkel equation:

$$\mu = \mu_0 e^{-\left(\Delta_0 - \beta\sqrt{F}\right)/kT_{eff}} \qquad \textbf{Equation 1.8}$$

where μ_0 is the mobility at zero applied field, β is the Pool-Frenkel factor ($\beta = (e/\pi\varepsilon\varepsilon_o)^{1/2}$), F is the magnitude of the electric field, and T_{eff} is the effective temperature. The carrier mobility in these materials is described as a thermally activated process in which the mobility increases with temperature. This Pool-Frenkel mechanism describes a phenomenon by which an applied electric field changes the potential near the localised states causing an increased tunnel transfer rate between active sites. Studies conducted by Sakanoue *et al*. have shown TIPS-pentacene polycrystalline FETs display a temperature dependent mobility whereby field-effect mobility increases with decreasing temperature.[32] Additionally, at low drain and gate voltages ($V_D = V_G = -15V$) traps-states inhibit mobility but at high drain and gate voltages ($V_D = V_G = -30V$) trap-states are filled and more mobile

states can be accessed. It was concluded from the study that charge transport is not band-like neither is it polaron trapped as in some polymer thin-films, but experiences an increased mobility at low temperatures due to freezing of intermolecular motions.

Charge-carrier mobility is highly dependent on the degree of long-range ordering with the semiconductor as well as the amount of defects present. Increasing the long-range order and limiting the number of defects within the film structure is highly advantageous approach for better charge transport.

1.5.1.3 Grain Boundary Models & Traps Limited Transport

In organic transistors, charge transport is limited by localised states induced by defects and unwanted impurities.[34] These large scale macroscopic effects within an OTFT can be described by three major traps-states that decrease charge-carrier mobility.[29] Firstly, impurities within the thin-film or present close to the dielectric/semiconductor interface can trap holes or electrons due to their unoccupied energy states residing close to the HOMO or LUMO, respectively. Secondly, grain boundaries composed of several grains within the active layer can be severely detrimental to charge transport. This trap-state effect is the main cause for decreased charge transport in polycrystalline thin-film transistors. The effect of grain boundaries are well known in polysilicon TFTs where their influences are strongly manifested in the mobility and subthreshold swing. Thirdly, misalignment of neighbouring organic semiconductor molecules within grains, due to poor nucleation and growth (i.e. weak London dispersion forces or Van-der Waal intermolecular bonds) can hinder charge transport as a result of poor electronic overlap between molecules. This last point is significantly important as the exact stacking order, orientation and alignment of the organic semiconductor, specifically for small

molecules, strongly influences device performance. It is critical for achieving higher charge-carrier mobility to supress disorder phases and grain boundaries in the active layer material. Polymorphic crystal growth leads to grain boundaries which have been observed in evaporated pentacene films offering lower device performance.

The effective mobility (μ_{eff}) in amorphous and polycrystalline films (taken from models based on silicon) can be represented by the following equation:

$$\frac{L}{\mu_{eff}} = \frac{L_g}{\mu_g} + \frac{L_{gb}}{\mu_{gb}} \qquad \textbf{Equation 1.9}$$

where the mobility is related to the intra-grain mobility (μ_g) and grain boundary mobility (μ_{gb}), and the effective length of the grains (L) is related to their respective grain length (L_g) and grain boundary length (L_{gb}).[18,24] Due to the intra-grain mobility and length being much larger in relation to the associated components of the grain boundaries, **Eq.1.9** can be tentatively approximated to $\mu_{eff} \approx \mu_{gb}$.

Multiple trapping and thermal release (MTR) transport model is commonly used to describe real organic transistors due to charge transport being mostly limited by localised states induced by defects and unwanted impurities. This leads to only a fraction of the gate induced charge contributing to the current flow, whereas the remaining part is trapped in an exponential band tail of trapping states.[35] As the gate voltage increases, injected charge-carriers fill trap-sites rendering them inactive, leading to improved delocalised charge transport. This forms a gate voltage dependence mobility which has been observed in amorphous silicon TFTs,[36] but seldom in single crystal OTFTs,[37] confirming that the V_G dependence originates

from localised levels associated with chemical and physical defect-induced effects.[34] Accordingly, as the quality of the OTFT improves, the gate voltage dependence and thermally activated mobility is reduced. The impact of grain boundaries and the electrode and substrate surface conditions on the electrical performance of OTFTs are studied in **Chapter 4** and **Chapter 5**.

1.5.1.4 Marcus Model

The mobility for the vast majority of organic semiconductors measured at ambient temperature can be explained in terms of a series of thermally activated electron transfer processes that allow charges to move from molecule to molecule.[38] The rate of charge transfer between neighbouring semiconducting molecules can be described by:

$$k_{ET} = \frac{2\pi}{\hbar}\frac{t^2}{\sqrt{4\pi\lambda kT}}\exp\left[-\frac{\lambda/4 - t}{kT}\right] \qquad \textbf{Equation 1.10}$$

where k_{ET} is the rate of charge transfer, t is the transfer integral, and λ is the reorganisation energy.[34] The transfer integral is related to the electronic overlap between adjacent molecules and the reorganisation energy is the energetic penalty associated with charging a molecule (i.e. the difference in energy between charge and neutral species). Enhanced charge transport, in terms of the rate of electron transfer, requires a large transfer integral for better electronic overlap (i.e. electronic coupling between molecules), and a smaller reorganisation energy.[29,39] Charge transport for a series of polyacene semiconductors (e.g. naphthalene to pentacene) has been explained by applying this method.[30] This Marcus model deduces that π-stacking alone does not guarantee high mobility (which has been seen for certain

small molecules with excellent π-stacking properties), and orbital overlap is not determined by orbital energies.

1.5.2 Charge Carriers in Organic Semiconductors

Organic semiconductors are commonly described by charge transport models associated with disordered systems (e.g. hopping transport). Amorphous or polycrystalline organic semiconductors are known to exclusively favour either positive (holes) or negative (electrons) charge-carriers, due to the asymmetrical density of states (DOS) of these systems. This is a fundamental issue in OTFT design as this limits the fabrication of ambipolar transistors.

Pentacene is a widely studied organic semiconductor due to its impressive hole mobility (μ_{FET} = 0.5 – 1.5 $cm^2 V^{-1}s^{-1}$). The nature in which this organic material is classified as a *p*-channel OTFTs is due to the exact molecular structuring of the molecule. The hydrogen atoms which surround the carbon backbone are less electronegative than the associated carbon core thereby lending some electron density to the delocalised π-cloud. Due to the electron-rich nature of the conjugated carbon backbone this shifts the energy levels so as to favour the loss of an electron over its gain. Positive charge-carriers dominant the transport properties of pentacene classifying it as a *p*-channel device material. Pentacene does display good chemical and thermal stability but is easily oxidised (most commonly in the 6 and 13 positions) which disrupts its crystallinity and electronic properties.

The chemical structure of organic semiconductors is not the only factor which determines whether an OTFT displays *p*-channel or *n*-channel device characteristics. Processing conditions (e.g. inert atmosphere, material oxidation),

device architecture, choice of gate dielectric, and choice of electrodes, play important functional roles.[20] Further investigations suggest organic semiconductors to be ambipolar and thus capable of conducting electrons and holes under optimised conditions, leading to a revised DOS for such systems which suggests a symmetrical charge distribution.[40] Experimental work conducted by Chau *et al.* showed electron trapping mechanisms in SiO_2 when used as the gate-dielectric.[40] This was caused by mobile electrons being trapped by hydroxyl groups in the form of silanols present at the dielectric/OSC interface, which prompted the use of a hydroxyl-free insulator. Unintentional doping from electronegative groups on the gate-dielectric is known to form trap-sites which contribute to the asymmetry observed in the DOS. As well as being dependent on trap-states, the charge-carrier type is also reliant on the HOMO-HOMO wave function overlap between neighbouring molecules, the respective LUMO-LUMO wave function overlap, and the relative positions of the HOMO and LUMO with respect to the Fermi energy of the source and drain electrodes.[18]

An abundant of *n*-channel organic semiconductors have been developed but display much lower mobility performance in OTFTs compared with hole transporting organic materials. Commonly electron withdrawing groups are incorporated to create an electron deficient core which carries electrons more efficiently.[10] By doing so this increases the electron affinity of the molecule by lowering the LUMO making it easier to gain an electron.[34] The electron deficiency has a strong impact on the injection of charges at the electrode, since the relatively low lying LUMO can be readily reduced in comparison with electron-rich materials. This is important in applications where charge needs to be electrically injected which strongly applies to TFTs. Due to the nature of these semiconductors, they are prone to atmospheric oxidants due to the instability of the organic anions.[34] In undoped

organic semiconductors no free charges exists at zero bias (except for thermally excited charges from the metal contact), although unintentional doping by oxidation can influence this factor.[41]

Solution-processable organic polymer semiconductors have advanced to meet requirements for low-cost manufacturing but are still limited by poor charge-transport properties. Regioregular poly(3-hexylthiophene) (P3HT) has gained significant focus due to the averagely high mobility (< 1 cm^2 V^{-1} s^{-1}) quoted for this organic semiconductor.[42,43] Recent progress in the development of high mobility polymers has advanced with the production of poly(2,5-bis(3-alkylthiophen-2-yl)thieno[3,2-b]thiophene) (PBTTT).[44] This is a Merck Chemicals semiconducting liquid crystalline polymer which has shown very high mobilities and excellent stability for a soluble polymer. The field of solution-processable polymers and electron dominant charge transport in organic semiconductors are advancing areas of research but are vastly outperformed by *p*-channel device materials. Solution-processable materials of TIPS-pentacene and diF-TES-ADT are the two small molecule semiconductors studied in this thesis due to their large hole mobility as quoted in literature.

1.6 Source/Drain Modification in OTFTs

The operating junction between the source and drain contacts and the channel region of the device is one of two critical interfaces in OTFTs, with the second occurring between the dielectric and semiconductor. It is essential that the source and drain electrodes are engineered to inject charges under all bias conditions. The strategy of achieving ohmic contacts by means of strong localised doping of the semiconductor close to the surface is commonly adopted for inorganic

semiconductors but is challenging to implement in OTFT design.[45] Organic transistors rely on engineering appropriate alignment of the electrode E_F and the respective frontier molecular orbital of the organic semiconductor to achieve ohmic conditions. Optimising the energetic alignment between the injecting electrode and the organic semiconductor is essential for OTFTs as interfacial barriers formed at this interface will impede charge flow through the device. The use of Au as the source/drain electrode is commonly adopted due to its high work function ($\Phi = 5.1\,\text{eV}$) matching closely to most HOMO levels of many *p*-channel organic semiconductors (see **Fig.1.8(a)**), along with its low

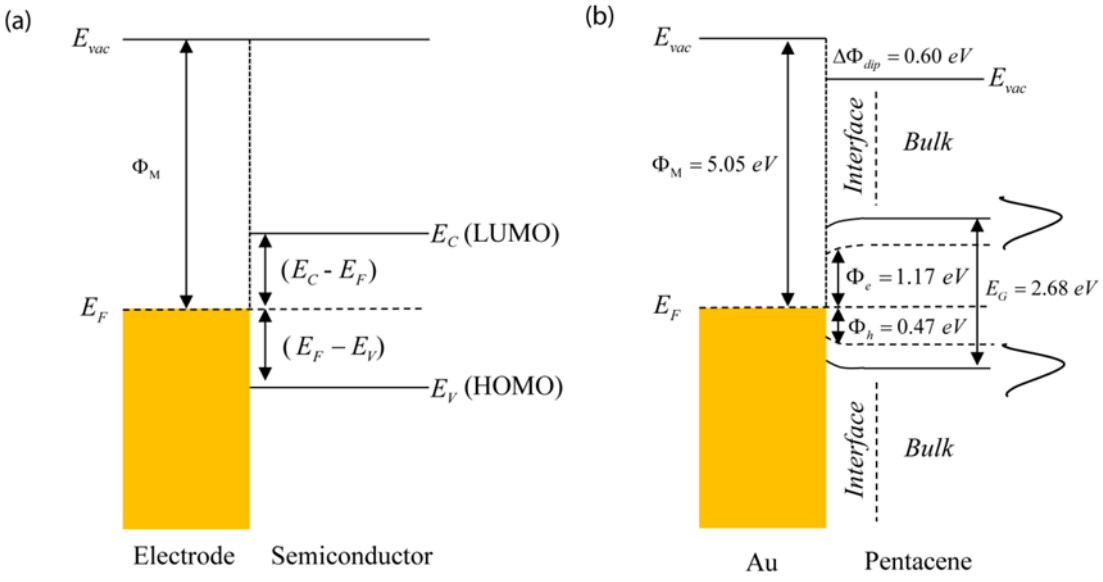

Figure 1.8: (a) Simple band line-up diagram for metal-semiconductor interface assuming the Mott-Schottky rule holds and that the vacuum level for the metal and semiconductor are aligned. (b) Band line-up diagram for the Au-pentacene interface.[34]

oxidation rate compared with other metals (e.g. Ag, Cu). In reality, the interface formed between Au and pentacene leads to a significantly greater resistance. Instead,

the interface exhibits an additional 'dipole' barrier ($\Delta\Phi_{dip}$) that shifts the vacuum level upwards by 0.60 eV or higher (see **Fig.1.8(b)**). The barrier height is substantially increased which is a result of the 'push-back' effect, where the tail of electron density extending from the metal free surface tends to be pushed back as molecules are deposited, resulting in a decreasing work function of the metal.[34] The slight shrinking of the band-gap at the interface is due to polarization effects by the metal.[34]

Minimising the barrier to hole injection ($\varphi_B = IP_{SC} - \Phi_M$) for *p*-channel devices is essential for efficient current injection, as shown in **Fig.1.9**. Metals with even higher work functions than Au are also adopted but not as widely studied (e.g. Pd, Pt). Theoretically, a similar but opposite approach should be beneficial for access to the LUMO level through the use of low work function metals (e.g. Ca, Mg, Al, etc.). This approach is actually limited by the high reactivity and oxidation rates of these metals due to their low activation energy. The formation of insulating surface oxides and adsorbates are hypothesised to interfere with conduction at the electrode and known to alter the work function. The environmental stability of a metal such as Au provides low contact resistance (which is a function of both parasitic resistance and charge-barrier formation) at the metal/semiconductor interface by limiting the formation of surface oxides. Studies implementing high work function Au electrodes in *n*-channel devices have shown to be a much better approach, not from an energetics point, but because of its lower reactivity.[46] This shows that it is also important for contacts to possess high conductivity for optimal performance. It is a highly complex task to disentangle influences at the metal/semiconductor interface in OTFTs and their related effect on device performance (e.g. morphological, charge

transfer, surface dipoles). Additionally, improved performance can be related not just to the energetic alignment but also field enhancement effects at the contact edge.[10]

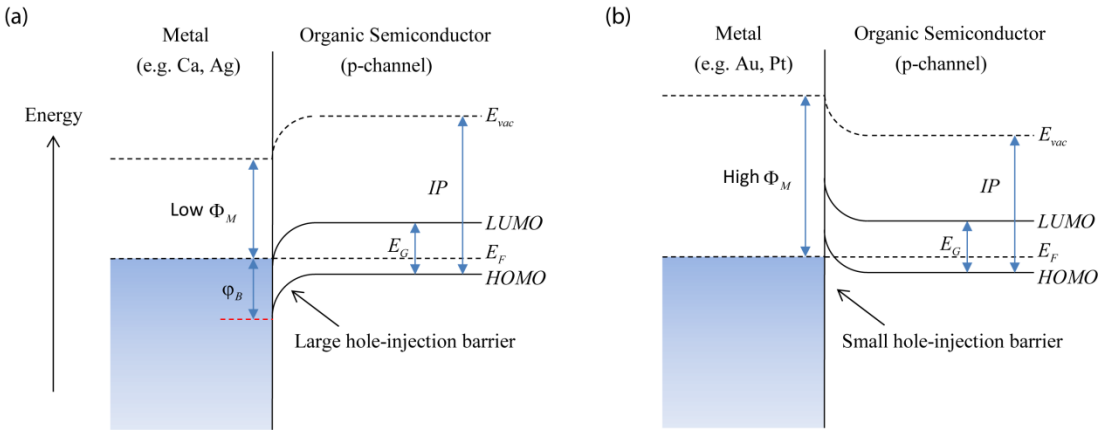

Figure 1.9: Energy band diagrams of a metal/semiconductor interface in a *p*-channel device for (a) low work function metal forming poor contacts and (b) high work function metals forming improved contacts. This scheme ignores interface state formation.

The type of material used as the gate-electrode is somewhat relaxed in comparison to selection of the source/drain contacts, but is required to be highly conductive and provide low surface roughness, which is a more significant factor for bottom-gate architectures. Additionally, the gate-electrodes compatibility with other subsequently deposited device layers is essential.

1.6.1 Charge Injection: Theories and Principles

Charge-carrier transport across metal/semiconductor interfaces experience potential energy barriers that must be overcome for charge injection into the semiconducting material to occur. This injection of charge-carriers can be described fundamentally by two principle mechanisms (i) thermionic emission and (ii)

quantum mechanical tunnelling, as illustrated in **Fig.1.10**. Diffusion limited injection occurs at metal/semiconductor interfaces due to changes in temperature (i.e. thermionic emission) and changes in gate voltage. Other injection mechanisms are also known to exist (e.g. defect-assisted transport) but will not be discussed in this work. It must be noted, that for disordered systems with significantly large potential barriers, thermionic emission models cannot explain the field and temperature dependence of charge injection. Hopping injection into disordered density of localised states are commonly used to explain this type of charge injection more concisely. A caveat of thermionic emission is that it neglects disorder in the semiconducting material as it is adapted from inorganic crystalline semiconductors.

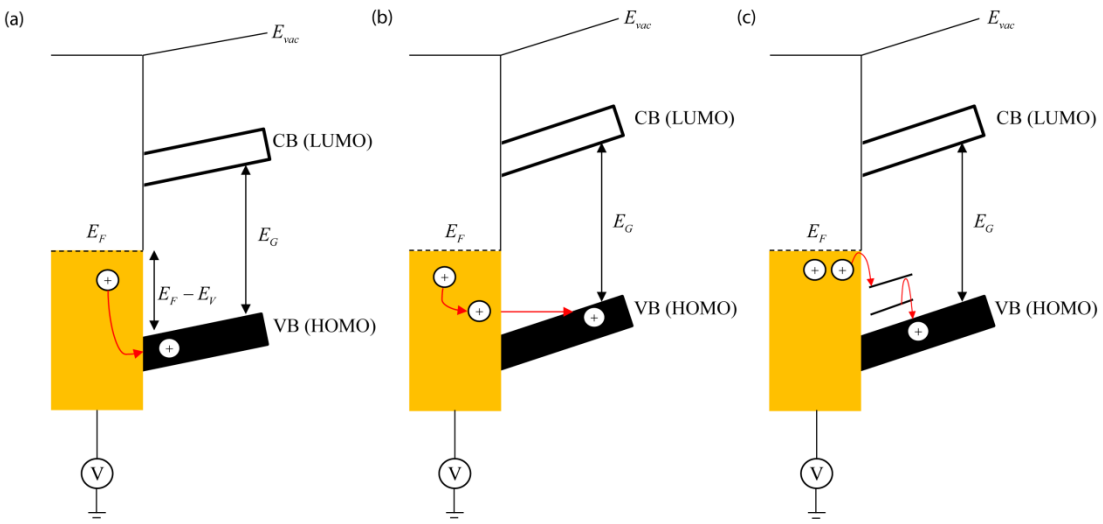

Figure 1.10: (a) Thermionic emission, (b) Field emission (tunnelling), (c) Defect-assisted injection.

Charge-carriers (electrons or electron-holes) in the metal contact are thermally excited across/over the potential barrier when the barrier is < 0.3 eV. An offset in energy misalignment, typically > 0.3 eV, occurs because of a potential difference (aka. Schottky junction) between the Fermi level, E_F, of the metal and

the frontier molecular orbital of the organic semiconductor. This Schottky junction current at this interface can be described by the Richardson-Dushman equation:

$$J = B_e T^2 \exp\left(-\frac{\Phi_B}{k_B T}\right) \qquad \textbf{Equation 1.12}$$

where B_e is the emission constant (related to the Richardson-Dushman constant), T is absolute temperature, and Φ_B is the potential barrier.

When a voltage is applied to the metal (anode) leading to an electric field across the barrier (with respect to the cathode), thermionic emission (or injection current) is increased by a lowering in the potential energy barrier (Φ). This reduction against thermionic emission leads to a new barrier $\left(E_F + \Phi_{eff}\right)$ which becomes the effective work function in the presence of an applied field. This can be described mathematically by:

$$\Phi_{eff} = \Phi - \left(\frac{e^3 E}{4\pi\varepsilon_o}\right)^{1/2} \qquad \textbf{Equation 1.13}$$

where E is the applied electric field, e is the elementary charge of an electron and ε_o is the dielectric constant of a vacuum. This lowering in the work function by the applied field is known as the Schottky effect.

The current density (defined in **Eq.1.12**) now changes to incorporate the effective work function which defines field-assisted thermionic emission by:

$$J = B_e T^2 \exp\left[-\frac{(\Phi - \beta_s \mathrm{E}^{1/2})}{k_B T}\right] \qquad \textbf{Equation 1.14}$$

where β_s is the Schottky coefficient. When the applied field is significantly large $\left(E > 10^7 \text{ V/cm}\right)$ the potential barrier at the metal surface bends becoming narrow in its shape leading increased probability that an electron will tunnel through barrier escaping into vacuum (or into the semiconductor). This process is termed field emission.

The current density is given by the Fowler-Nordheim equation:

$$J = BE^2 \exp\left(-\frac{E_C}{E}\right) \qquad \textbf{Equation 1.15}$$

where B and E_C are temperature-independent constants that depend on the work function of the metal.

A potential barrier regularly exists at the injecting electrode and organic semiconductor in the majority of cases. The most common approach in overcoming such barriers is through matching energy misalignments through optimum selection of materials to overcome the barrier-offset. Buffer layers (e.g. transparent conducting oxides) sandwiched between two unmatched materials (i.e. metal and OSC) can aid energetic alignment by behaving as an interfacial electric field for better alignment of the Fermi level with the semiconductor. Facile techniques for modifying the surface conditions of the metal contact can done by ultraviolet ozone treatment $\left(UV/O_3\right)$, argon ion bombardment, and oxygen plasma exposure. These approaches are quick and effective but unstable in the long-term. A commonly adopted technique for a wide range of scientific fields is surface modification by wetting agents such as SAMs.

1.6.2 Self-Assembled Monolayers (SAMs)

Self-assembled monolayers are two-dimensional asymmetrical molecular assemblies formed spontaneously by the immersion of an appropriate substrate into an active surfactant solution dissolved with an organic solvent.[47] From an energetic point of view, a self-assembling surfactant molecule can be divided into a three element structure (illustrated in **Fig.1.11**).

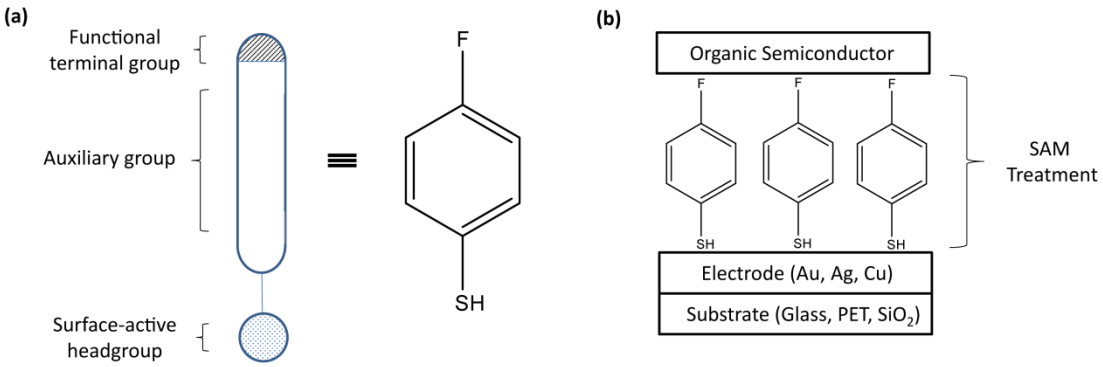

Figure 1.11: (a) Scheme of a thiolate monomer divided into its three constituent parts, and (b) an illustrated representation of a SAM formed from an aromatic thiol.

The three constituent parts of a self-assembled molecule will be discussed separately in the following section:

Head-group: The surface active head group (aka. anchor group) has high affinity to the surface and performs the most exothermic process (i.e. chemisorption of the molecule to the substrate surface).[47] Due to its exothermic nature each molecule tries to occupy every available binding site on the surface resulting in the formation of a monolayer. Commonly adopted head groups are, hydroxyl, carbonyl, carboxyl, amino, sulfhydryl and phosphonates. Typically, -SH groups are used to modify noble metals, and head-groups such as -COCl, $-PO_2Cl_2$, and $-SO_2Cl$ have high affinity to

-OH terminated surfaces. Chemisorption of the -SH head-group to the metal surface can form a bound species or can remain –SH terminated leading to a physisorbed unbound species. Adsorption of TP onto Au(111) has shown sulphur anchoring between two substrate atoms (i.e. close to the bridge site) but slightly shifted towards the nearest hollow.[48]

Auxiliary group: This constituent part is connected to the head group and typically consists of an alkyl chain or aromatic ring which facilitates charge transport across the length of the surfactant molecule. The auxiliary group is critical in the ordering/packing of the surfactant on the surface associated with molecular interactions between neighbouring organic molecules. Interactions between alkyl chains are formed of Van der Waals and electrostatic interactions, whereas the most dominant intermolecular interactions between aromatic species are $\pi - \pi$ interactions (when orientated normal to the substrate surface). The more densely packed the layer becomes, the greater the interactions between the organic molecules. Aromatic thiols have rigid structures which provide greater stability and are highly conductive due to their conjugated nature.[49,50] These key properties means highly ordered SAMs can be produced due to the face-to-face or/and face-to-edge interactions between phenyl rings, and have shown to offer better OTFT performance as electrode modifiers than alkanethiols.[51] For these main reasons, derivatives of aromatic based thiols were the primary class of monomers studied in this thesis. Short aromatic thiols consisting of a single benzene ring with strongly halogenated terminal groups were of interest in this work due to the large conductivity associated with such molecules.

Terminal group: Lastly, the terminal group determines the physical and chemical interaction of the thiolate to subsequent deposited layers.

The most common approach for interface engineering in OEDs is through the implementation of self-assembled monolayers.[19] Their use as a passivation layer and surface modifier has led to their widespread usage in numerous applications. Interface modifications in OTFTs are introduced at the dielectric/semiconductor and metal/semiconductor regions due to their critical importance in device functionality. The former mentioned interface addresses charge trapping effects at the dielectric interface, commonly adopting alkylsilanes to passivate the surface (e.g. octadecyltrichlorosilane,[52], hexamethyldisilazane[53]). Research into using varied chain lengths (*n*) of alkyltrichlorosilanes ($CH_3(CH_2)_{n-1}SiCl_3$) as well as oxygen-plasma exposure treatment to the dielectric surface have shown insightful results in terms of reduced charge trapping effects at this interface. The most widely used class of SAMs for contact modification at the metal/semiconductor are thiols, which are typically adopted in bottom-contact OTFTs. These monomers bind to noble metal surfaces (e.g. Ag, Au, Pt) through a chemisorption process, where the sulfhydryl group of the thiol forms a covalent bond with a metal atom and the hydrogen atom is subsequently released. SAMs are self-limiting, as once all binding sites on the target surfaces are occupied a single molecule thick monolayer will form across the exposed surface, which is densely packed and highly ordered when considering ideal conditions. At high coverages strong depolarization occurs due to a counterbalancing effect of the electric field generated by the dipole moments of neighbouring molecules, resulting in a gradual plateau in the work function contributed by the molecular dipole of the adsorbate.[54]

Thiols composed of auxiliary groups made of aromatic structures have minimal impedance (i.e. low contact resistance) to conduction whereas long alkyl chains are more insulating in nature. SAMs are classified as organic polar molecules which possess an intrinsic dipole moment that strongly relates to the associated work function shift.[21] The adoption of SAM modification is commonly implemented in devices for tailoring the work function of the electrode to increase the built-in potential or reduce energy barriers for charge injection or collection (i.e. reduce contact resistance), and enhance wetting of the organic layer deposited on top by altering the surface energy at non-ideal interfaces. This offers a high degree of control over the surface properties at these interfaces if optimal conditions are asserted. The thiol molecules can be deposited from the vapour phase (in a saturated atmosphere) or formed from solution using an organic solvent. Functionalizing metal surfaces from aqueous solution (under atmospheric conditions) leads to the formation of several defects/instabilities formed within the monolayer, which strongly influence the structural ordering of the monolayer. Although this practise is the most common and expedient approach, its ease of facilitation heavily outweighs other alternative methods. The conditions associated with self-assembly deposition from solution strongly influence the structural ordering of the monolayer. Parameters such as the concentration of adsorbate (molar concentration),[55,56] temperature,[57] and solvent properties,[58] which are some of the key factors influencing packing density and structural defects within the SAM. The surface crystallography/reconstruction and surface free energy properties also influence the structural arrangement of thiolates. Additionally, the exposure time designated for self-assembly plays a critical role in the molecular ordering and completeness of the

resultant layer, which is strongly dependent on the cleanliness and topological structuring of the target surface.

Numerous publications have reported improvements in energetic alignment and enhancements in semiconductor film quality in relation to improved device performance. The majority of thiols discussed in this thesis form hydrophobic surfaces which aids in the reduction of surface tension of the electrode surface promoting better molecular ordering of the OSC. Different interfacial properties can be achieved by varying the rigidity, length, and functional terminal group of the molecule. By making these changes, alterations in morphological features (e.g. stacking, uniformity, packing density) and electronic properties (e.g. polarity, charge density at the surface) can occur in both the SAM and the adjacently deposited layer.

The simplicity and effectiveness of implementing SAMs has led to its widespread adoption in OPV and OLED design. Research conducted in OPV development has shown the effective approach of surface modification of the indium tin oxide (ITO) electrode by application of benzoic (carboxylic) acids and phosphonic acids as surface based modifiers. This has shown to improve energy matching at the ITO/donor or acceptor interface providing better short circuit current $\left(J_{SC}\right)$.[59,60] Additionally, OPV development by introduction of a SAM at the ITO electrode has shown to be non-effective due to Fermi level pinning effects,[61] whereas other results have shown minimal contribution to OPV performance when energetic alignment is equal to or increased beyond the ionisation potential of the interfacial organic material.[62]. It has been noted that long exposure periods are required for effective functionalisation of the ITO surface leading to excessive preparation times.

1.6.3 Thiol Self-Assembly on Gold: Mechanisms and Kinectics

The grafting of organic molecules (polar or non-polar) onto a metal can affect the dipole layer present at this surface. A change in the dipole modulates the work function of the metal, where increasing or decreasing of the work function is dependent on the electron accepting and electron donating properties, respectively. Polar molecules which possess a permanent dipole moment and a strong electron accepting functional group lead to an increase in the work function at the metal surface. This can be achieved without charge-transfer between the metal and organic molecule or rearrangement of the electron cloud protruding from the metal surface. Decreasing of the work function is more commonly achieved with non-polar molecules which are attributed to a chemical mechanism such as charge transfer mechanisms or the rearrangement of the electron distribution at the interface as a result of the formation of new chemical bonds.[63]

The potential energy shift (i.e. change in work function, $\Delta\Phi$) as a result of the assembly of a monolayer can be expressed by:

$$\Delta\varphi = -eN\left(\frac{\mu_o}{\varepsilon_{SAM}\varepsilon_o}\right) \qquad \textbf{Equation 1.16}$$

Where N is the surface density of molecules, μ_o is the molecular dipole moment normal to the surface, ε_{SAM} is the dielectric constant of the SAM.

The study of self-assembly has been extensively investigated on single-crystal Au (111) due to its well-known reconstructive surface and stable properties. A smaller amount of research has been conducted on other single-crystals such as Ag and Cu (e.g. most commonly <110> and <100>), but some excellent work in this area exists. The absorption of thiols onto Au surfaces has been described as an

oxidative addition of the S-H bond onto its surface.[64-68] This reaction can be described as:

$$R-S-H+Au_n \rightarrow R-S^{(-)}-Au^{(+)}+Au_{n-1}+\frac{1}{2}H_2 \qquad \textbf{Equation 1.17}$$

This reaction leads to a reductive elimination of the hydrogen molecule after deprotonation. It is generally thought that the hydrogen molecule is lost on chemisorption, resulting in an Au-S interaction.[68]

The metal-sulphur interaction on Au (111) surfaces drives the assembly to form an $(\sqrt{3}\ \text{x}\ \sqrt{3})\ \text{R30°}$ overlayer of thiolates. However, a secondary ordered superlattice is also formed which is commonly referred to as $\text{c}\,(4\ \text{x}\ 2)$. The structuring of such monolayers are strongly determined by the chain length and nature of the terminal group. In such configurations the average area occupied per molecule is 0.215 nm^2 and distance between alkyl chains is ca. 0.5 nm. Tilt angles normal to the surface and twist angles about the molecular axis of the thiol can be influential in terms of packing density.

1.6.4 Charge Injection Layers (CILs): Alternatives to SAMs

Although SAM modification of conductive contacts is widely used, several other charge injection layers (CILs) have been reported. Polymer light emitting diodes (PLEDs) and OPVs have shown to benefit from ITO modification by using poly(3,4-ethylenedioxithiophene):polystyrene sulfonic acid (PEDOT:PSS), due to its higher work function and less variable conductivity issues compare with ITO.[59]. Large conductivity values (e.g. 800 - 3000 Scm^{-1}) have been published for this polymer ionomer mixture, making it suitable as an electrode and viable for roll-to-

roll processing.[70] Additionally, evaporated metal oxide layers deposited onto the ITO electrode, such as molybdenum oxide $\left(MoO_x\right)$ and vanadium oxide $\left(V_2O_5\right)$, have shown to improve interfacial contacts in these devices.[71,72]

Modulation of the interfacial barrier height formed in OTFTs can be achieved by alternative methods. Depinning of the Fermi level at the metal/OSC interface can be achieved through the introduction of an ultrathin insulating interfacial layer, Si_3N_4 to produce tunnelling contacts.[73,74] Other methods such as, changing the metal used as the electrode,[75] doping the electrode surface (i.e. chemical treatment),[76] and implementation of a hole-injection layer (e,g. PEDOT:PSS),[77] have all shown to induce different surface properties resulting in enhanced carrier injection for *p*-channel devices. Insertion of CuPc between ITO and pentacene has also shown significant improvements in charge-injection for OTFT devices.[78] Insulating polymers such as polyethylenimine ethoxylated (PEIE) and polyethylenimine (PEI) have shown to be effective in lowering the work function of electrode surfaces (c.a. 1 eV). These surface dipole compounds which physisorb to the electrode surface show particular promise for their potential implementation into *n*-channel OTFTs.[79]

1.7 Thesis Motivation and Layout

The research emphasis behind this thesis is to investigate device engineering and active-layer development for improving OTFT functionality. The key objectives of this thesis are to advance the device performance of OTFTs through investigating the critical interface at the electrode/semiconductor region, and study the influence of acene-polymer based ternary systems for advancing structural properties of the active layer. Particular emphasis is made in this work regarding the influence of

SAMs formed at the source/OSC interface and it helps to overcome poor charge-injection properties at this critical junction of the device.

Chapter 1 has provided a review of OTFTs and functional properties of organic semiconductors, along with discussions of interfacial modification of the critical interfaces in organic transistors.

Chapter 2 discusses the experimental techniques used throughout this work with an overview of their operation. OTFT device preparation and parameter extraction is also discussed.

Chapter 3 addresses the application of SAM modification of noble metal surfaces (i.e. Au and Ag) with discussion of the chemical and physical properties of the functionalised surface. Electronic properties of the thiol modified surfaces are discussed in terms of surface energy properties and work function shifts associated with the dipole of the polar molecule. The stability of such thiol was also investigated when prepared under thermal treatment conditions.

Chapter 4 discusses the implementation of thiols into organic thin-film transistors as the electrode modifier of the source and drain contacts. A range of thiols were used as comparative study to examine their influence on device performance. All devices in this chapter were prepared using TIPS-pentacene/polymer based active layers in top- and bottom-gated devices.

Chapter 5 explores the implementation of diF-TES-ADT used with a polymer binder under similar SAM modified electrodes discussed in Chapter 4. A discussion in terms of active layer morphology and its formation from spin-coating is examined.

Chapter 6 summaries the work achieve in this thesis and outlines ideas for the continuation of research within this field.

1.8 References

[1] G. Gelinck, P. Heremans, K. Nomoto, T. D. Anthopoulos, *Adv. Mater.*, (2010) **22**, 3778.
[2] Y.-L. Loo, I. McCulloch, *MRS Bull.*, (2008) **33**, 653.
[3] Capability Guide: UK Plastic Electronics (2012).
[4] House of Commons: Fourth Report of Session (2008-09) **1**, 28-52.
[5] http://www.softmachines.org/wordpress/?p=1276, April 2014.
[6] C. W. Tang, *Appl. Phys. Lett.*, (1986) **48**, 183.
[7] C. K. Chiang, C. R. Fincher, Y. W. Park, A. J. Heeger, H. Shirakawa, E. J. Louis, S. C. Gau, A. G. MacDiarmid, *Phys. Rev. Lett.*, (1977) **39**, 1098.
[8] K. Takimiya, H. Ebata, K. Sakamoto, T. Izawa, T. Otsubo, Y. Kunugi, *J. Am. Chem. Soc.*, (2006) **128**, 12604.
[9] V. Podzorov, S. E. Sysoev, E. Loginova, V. M. Pudalov, M. E. Gershenson, *Appl. Phys. Lett.*, (2003) **83**, 3504.
[10] I. Kymissis, *Organic Field Effect Transistors*. (2009) Springer, 1st Edition.
[11] S. R. Forest, *Nature*. (2004) **428**, 911.
[12] K. Nomoto, N. Yoneya, N. Hirai, I. Yagi, N. Kawashima, M. Noda, J. Kasahara, *J. Soc. Inf. Display.*, (2007) **15**, 491.
[13] I. Yagi, N. Hirai, Y. Miyamoto, M. Noda, A. Imaoka, N. Yoneya, K. Nomoto, J. Kasahara, A. Yumoto, T. Urabe, *J. Soc. Inf. Display.*, (2008), **16**, 15.
[14] E. Huitema, G. Gelinck, B. V. D. Putten, E. Cantatore, K. Kuijk, K. Hart, D. D. Leeuw, *J. Soc. Inf. Display.*, (2002) **10**, 195.
[15] J. E. Lilienfeld, (1930) *Method and apparatus for controlling electric currents*, United States, 1745175.
[16] D. Kahng, (1963) *Electric field controlled semiconductor device*, United States, 3102230.
[17] H. Dong, X. Fu, J. Liu, Z. Wang, W. Hu, *Adv. Mater.*, (2013) **25**, 6158.
[18] V. C. Sundar, J. Zaumseil, V. Podzorov, E. Menard, R. L. Willett, T. Someya, M. E. Gershenson, J. A. Rogers. *Science*, (2004) **303**, 1644.
[19] I. H. Campbell, S. Rubin, T. A. Zawodzinski, J. D. Kress, R. L. Martin, D. L. Smith, N. N. Barashkov, J. P. Ferrais, *Phys. Rev. B.*, (1996) **54**, 14321.
[20] J. Zaumseil, H. Sirringhaus, *Chem. Rev.*, (2007) **107**, 1296.
[21] V. K. Singh, M. Baquer, *J. Appl. Phys.*, (2012) **111**, 034905.
[22] M. Kano, T. Minari, K. Tsukagoshi, H. Maeda, *Appl. Phys. Lett*., (2011) **98**, 073307.
[23] C. Reese, Z. Bao, *J. Mater. Chem.*, (2006) **16**, 329.
[24] R. W. I. de Boer, M. E. Gershenson, A. F. Morpurgo, V. Podzorov, *Physica Status Solidi A.*, (2004) **201**, 1302.
[25] T. Hasegawa, J. Takeya, *Sci. Technol. Adv. Mater.*, (2009) **10**, 024314.
[26] Y. Yuan, G. Giri, A. L. Ayzner, A. P. Zoombelt, S. C. B. Mannsfeld, J. Chen. D. Nordlund, M. F. Toney, J. Huang, Z. Bao, *Nat. Comm.*, (2014) **5**, 1.

[27] H. Klauk, *Chem. Soc. Rev.*, (2010) **39**, 2643.
[28] S. O. Kasap, *Principles of Electronic Materials and Devices*, (2002) Boston:McGraw-Hill, 2nd Edition, p255-258.
[29] A. Virkar, (2012) Ph.D Thesis. *Investigating the Nucleation, Growth, and Energy Levels of Organic Semiconductors for High Performance Plastic Electronics.* Springer.
[30] J.-L. Brédas, D. Beljonne, V. Coropceanu, J. Cornil, *Chem. Rev.*, (2004) **104**, 4971.
[31] M. Watanabe, Y. J. Chang, S.-W. Liu, T.-H. Chao, K. Goto, Md. M. Islam, C.-H. Yuan. Y.-T. Tao, T. Shinmyozu, T. J. Chow. *Nat. Chem.*, (2012) **4**, 574.
[32] T. Sakanoue, H. Sirringhaus, *Nat. Mater.*, (2010) **9**, 736.
[33] A. Salleo, R. J. Kline, D. M. DeLongchamp, M. L. Chabinyc, *Adv. Mater.*, (2010) **22**, 3812.
[34] Z. Bao, J. Locklin, (2010). *Organic Field Effect Transistors*. CRC Press, 143.
[35] G. Horowitz, M. E. Hajlaoui, R. Hajlaoui, *J. Appl. Phys.*, (2000) **87**, 4456.
[36] P. G. Le Comber, W. E. Spear, *Phys. Rev. Lett.*, (1970) **25**, 509.
[37] A. F. Stassen, R. W. I. de Boer, N. N. Iosad, A. F. Morpurgo, *Appl. Phys. Lett.*, (2004) **85**, 3899.
[38] J. E. Anthony, A. Facchetti, M. Heeney, S. R. Marder, X. Zhan, *Adv. Mater.*, (2010) **22**, 3876.
[39] V. Coropceanu, J. Cornil, D. A. da Silva, Y. Oliver, R. SIlbey, J.-L. Bredas, *Chem. Rev.*, (2007) **107**, 926.
[40] L.-L. Chau, J. Zaumseil, J.-F. Chang, E. C. W. Ou, P. K. H. Ho, H. Sirringhaus, R. H. Friend, *Nature*, (2005) **434**, 194.
[41] C. D. Dimitrakopoulos, D. J. Mascaro, *IBM J. Res. & Dev.*, (2001) **45**, 11.
[42] H. Sirringhaus, P. J. Brown, R. H. Friend, M. M. Nielsen, K. Bechgaard, B. M. W. Langeveld-Voss, A. J. H. Spiering, R. A. J. Janssen, E. W. Meijer, P. Herwig, D. M. de Leeuw, *Nature*, (1999) **401**, 685.
[43] Z. Bao, A. J. Lovinger, *Chem. Mater.*, (1999) **11**, 2607.
[44] M. L. Chabinyc, M. F. Toney, R. J. Kline, I. McCulloch, M. Heeney, *J. Am. Chem. Soc.*, (2007) **129**, 3226.
[45] D. Natali, L. Fumagalli, M. Sampietro, *J. Appl. Phys.*, (2007) **101**, 014501.
[46] C. D. Dimitrakopoulos, P. R. L. Malenfant, *Adv. Mater.*, (2002) **14**, 99.
[47] A. Ulman, *An Introduction to Ultrathin Organic Films*. (1991) Academic Press.
[48] J. Nara, S. Higai, Y. Morikawa, T. Ohno, *J. Chem. Phys.*, (2004) **120**, 6705.
[49] J. M. Tour, L. Jones II, D. L. Pearson, J. J. S. Lamba, T. P. Burgin, G. M. Whitesides, D. L. Allara, A. N. Parikh, S. V. Atre, *J. Am. Chem. Soc.*, (1995) **117**, 9529.
[50] H.-T. Rong, S. Frey, Y.-J. Yang, M. Zharnikov, M. Buck, M. Wühn, C. Wöll, G. Helmchen, *Langmuir*, (2001) **17**, 1582.
[51] C. Bock, D. V. Pham, U. Kunze, D. Kafer, G. Witte. C. Woll, *J. Appl. Phys.*, (2006) **100**, 114517.
[52] Y.-Y. Lin, D. J. Gundlach, S. F. Nelson, T. N. Jackson, *IEEE Elec. Dev. Lett.*, (1997) **18**, 606.
[53] I. Yagi, K. Tsukagoshi, Y. Aoyagi, *Appl. Phys. Lett.*, (2005) **86**, 103502.
[54] L. Romaner, G. Heimel, C. Ambrosch-Draxl, E. Zojer, *Adv. Funct. Mater.*, (2008) **18**, 3999.

[55] M. Kawasaki, T. Sato, T. Tanaka, K. Takao, *Langmuir*, (2000) **16**, 1719.
[56] C. D. Bain, E. B. Troughton, Y.-T. Tao, J. Evall, G. M. Whitesides, R. G. Nuzzo, *J. Am. Chem. Soc.*, (1989) **111**, 321.
[57] R. Yamada, H. Wano, K. Uosaki, *Langmuir*, (2000) **16**, 5523.
[58] O. Dannenberger, J. J. Wolff, M. Buck, *Langmuir*, (1998) **14**, 4679.
[59] S. Khodabakhsh, B. M. Sanderson, J. Nelson and T. S. Jones, *Adv. Funct. Mater.*, (2006) **16**, 95.
[60] N. Beaumont, I. Hancox, P. Sullivan, R. A. Hatton and T. S. Jones, *Energy & Environmental Science*, (2011) **4**, 1708.
[61] A. Sharma, A. Haldi, W. J. Potscavage, Jr., P. J. Hotchkiss, S. R. Marder and B. Kippelen, *Journal of Materials Chemistry*, (2009) **19**, 5298.
[62] R. M. Cook, L.-J. Pegg, S. L. Kinnear, O. S. Hutter, R. J. H. Morris and R. A. Hatton, *Advanced Energy Materials*, (2011) **1**, 440.
[63] H. Ishii, K. Sugiyama, E. Ito, K. Seki, *Adv. Mater.*, (1999) **11**, 605.
[64] A. Ulman, *Chem. Rev.*, (1996) **96**, 1533.
[65] D. K. Schwartz, *Annu. Rev. Phys. Chem.*, (2001) **52**, 107.
[66] F. Schreiber, *Prog. Surf. Sci.*, (2000) **65**, 151.
[67] J. C. Love, L. A. Estroff, J. K. Kriebel, R. G. Nuzzo, G. M. Whitesides, *Chem. Rev.*, (2005) **105**, 1103.
[68] P. Laibinis, G. Whitesides, *Langmuir*, (1990) **6**, 87.
[69] T.-W. Lee and Y. Chung, *Adv. Funct. Mater.*, (2008) **18**, 2246.
[70] L. S. Roman, M. Berggren and O. Inganas. *Appl. Phys. Lett.*, (1999) **75**, 3557.
[71] V. Shrotriya, G. Li, Y. Yao, C. W. Chu and Y. Yang, *Appl. Phys.Lett.*, (2006) **88**, 073508.
[72] I. Hancox, L. A. Rochford, D. Clare, P. Sullivan, and T. S. Jones, *Appl. Phys. Lett.*, (2011) **99**, 013304.
[73] D. Connelly, C. Faulkner, P. A. Clifton, D. E. Grupp, *Appl. Phys. Lett.*, (2006) **88**, 012105.
[74] Z. Liu, M. Kobayashi, B. C. Paul, Z. Bao, Y. Nishi, *Phys. Rev. B.*, (2010) **82**, 035311.
[75] L. Burgi, T. J. Richards, R. H. Friend, H. Sirringhaus, *J. Appl. Phys.*, (2003) **94**, 6129.
[76] B. H. Hamadani, D. Natelson, *J. Appl. Phys.* (2005) **97**, 064508.
[77] K. Hong, S. Y. Yang, C. Yang, S. H. Kim, D. Choi, C. E. Park, *Org. Electron.*, (2008) **9**, 864.
[78] Y. Watanabe, K. Kudo, *Proc. SPIE*, (2009), **7415**, 741515.
[79] Y. Zhou, C. Fuentes-Hernandez, J. Shim, J. Meyer, A. J. Giordano, H. Li, P. Winget, T. Papadopoulos, H. Cheun, J. Kim, M. Fenoll, A. Dindar, W. Haske, E. Najafabadi, T. M. Khan, H. Sojoudi, S. Barlow, S. Graham, J.-L. Brédas, S. R. Marder, A. Kahn, B. Kippelen, *Science*, (2012) **336**, 6079.

Chapter 2

Materials and Experimental Techniques

2.1 OTFT Characterisation and Testing Procedure

Current-voltage (I-V) curves were measured using an Agilent 4155C semiconductor parameter analyser. An Intertek manual probe station with three micropositioners (tungsten tips) was used to contact the designated electrodes of the transistor. All measurements were conducted under ambient conditions at room temperature, with no exposure to light during each measurement.

2.1.1 OTFT Parameter Extraction

Device parameters of interest from the I-V measurements of OTFTs are the field-effect mobility (μ_{FE}), on/off current ratio ($I_{ON/OFF}$), threshold voltage (V_T), subthreshold behaviour associated with the subthreshold slope (S), and turn-on voltage (V_{ON}). The field-effect mobility is extracted from transconductance (g_m) measurements in the linear and saturation regimes with associated mobilities μ_{lin} and μ_{sat}, respectively. The transconductance can be defined as the control of an output current by an applied input voltage, which in terms of transistor characteristics, g_m is the changes in drain-current as a result of a small change in the gate-voltage C_i, with constant drain-voltage (V_{DS}). The transconductance in the linear (**Eqn.2.1**) and saturation (**Eqn.2.2**) regimes are expressed as:

$$g_{m,lin} = \frac{\partial I_{D,lin}}{\partial V_{GS}} = \mu_{FE} C_i \frac{W}{L} V_{DS} \qquad \textbf{Equation 2.1}$$

$$g_{m,\text{sat}} = \frac{\partial I_{D,\text{sat}}}{\partial V_{GS}} = \mu_{FE} C_i \frac{W}{L}(V_{GS} - V_T) \qquad \textbf{Equation 2.2}$$

where C_i is the gate-dielectric capacitance, and L and W are the channel length and width dimensions, respectively. Through plotting g_m vs. V_{GS}, extrapolation and curve fitting can be used to measure the slope and intercepts of the graph for parameter extraction.

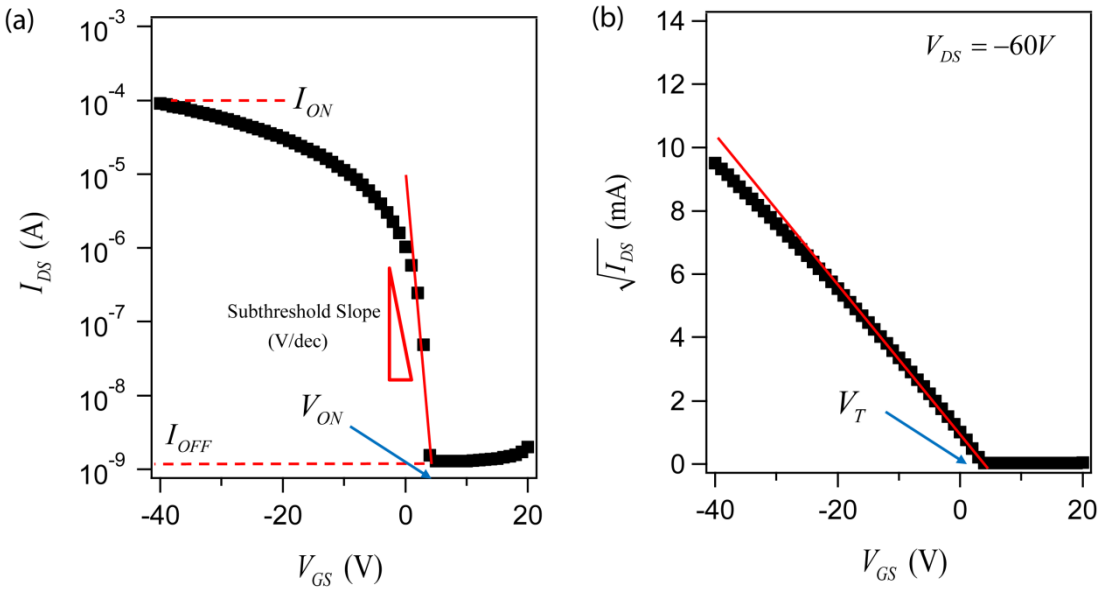

Figure 2.1: Extraction of OTFT device parameters from electrical characteristics: (a) $\sqrt{I_{DS}}$ vs. V_{GS} for extracting V_T and (b) I_{DS} vs. V_{GS} for extraction of I_{ON}/I_{OFF}, V_{ON}, and subthreshold slope (S).

Fig.2.1(a) shows a typical transfer characteristic in the linear regime as a semi-logarithmic plot which is used to extract the turn-on voltage (i.e. the gate bias at which the drain current abruptly increases above a defined low off-current level) and the subthreshold swing $(S = \partial V_{GS} / \partial(\log I_{DS}))$. The gradient of the current increase is directly proportional to the field-effect mobility, μ_{lin}, in accordance with

Eqn.2.1 if the mobility is independent of the gate voltage. **Fig.2.1(b)** shows a linear plot of a typical transfer characteristic in the saturation regime. Here, the square root of the drain current should display linear dependence with the gate voltage, with its gradient proportional to the field-effect mobility, μ_{sat}, in accordance with **Eqn.2.2**. Extrapolation to zero by creating a linear fit to the data plot yields the threshold voltage.

Several assumptions are made when modelling OTFT device performance when using the linear and saturation current equations mentioned above. Unique properties related specifically with OTFTs are the absence of an inversion layer, voltage-dependent mobility, and contact resistance, which are particular oversights when adopting these equations. Several other comprehensive models exist but were not implemented in this thesis due to the ever expanding nature of this field.[1]

Unless otherwise stated, all device data presented in this thesis was extracted from OTFTs with channel lengths (L) of 20 μm and channel widths (W) of 1000 μm. Linear regime measurements were conducted at V_D = -5 V and saturation regime at V_D = - 60V. An interdigitated transistor design with a continuous gate electrode stretching across all devices within each row was adopted. Devices were not electrically isolated and testing was conducted immediately after fabrication. **Fig. 2.2** is a graphical representation of the standard I-V plots used throughout this thesis. Forward and reverse scans from sweeping of the gate voltage between 20 V to -60 V and back are included in the majority of I-V curves. All devices were tested firstly in the linear regime and then the saturation regime.

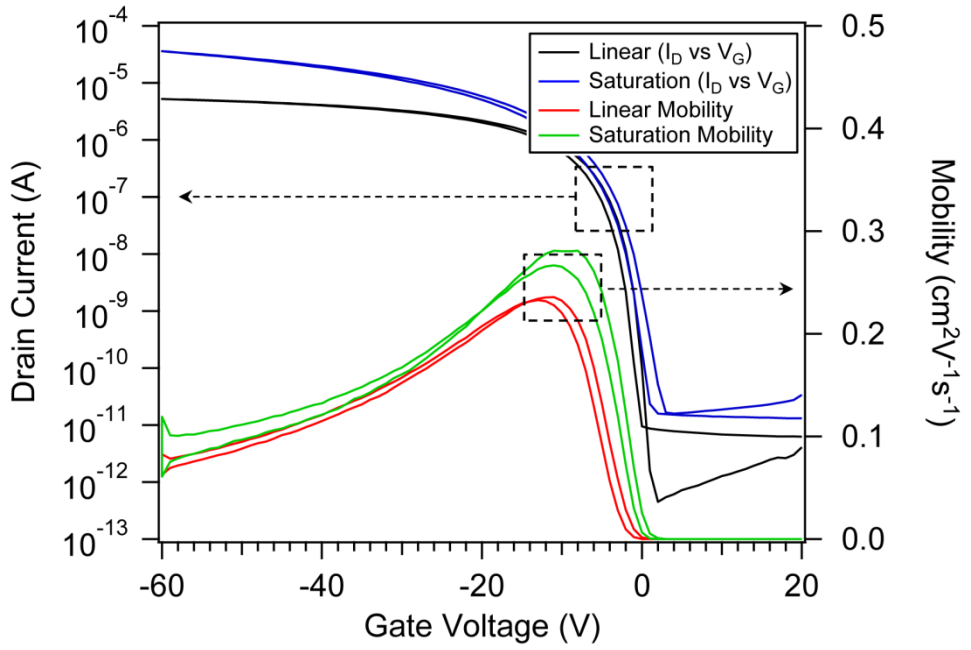

Figure 2.2: I-V graphical layout for generic OTFT device adopted throughout this thesis.

The device configuration adopted for the large majority of OTFTs discussed in this thesis was the top-gate/bottom-contact (TG/BC) architecture as shown in **Fig.2.3(a)**, unless stated otherwise. This device structure is termed as 'staggered' due to the position of the source/drain relative to the where the channel is formed. **Chapter 4** introduces the bottom-gate/bottom-contact (BG/BC) device structure as shown in **Fig.2.3(b)** for comparative purposes. This device structure is termed as 'planar' as the source/drain electrodes are in the plane of the channel.

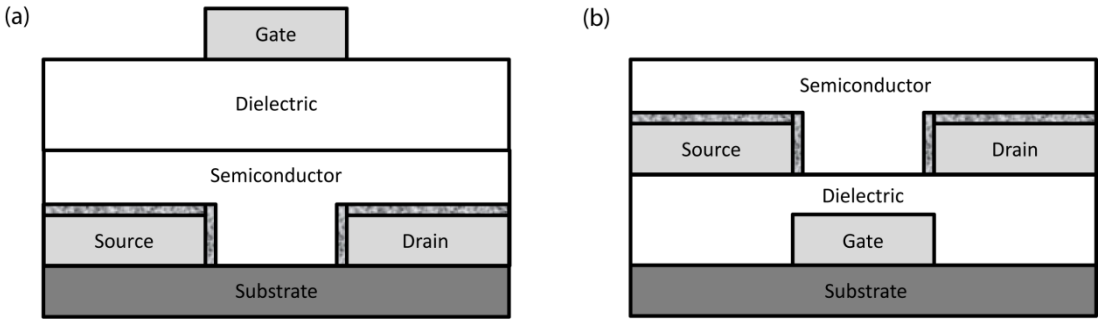

Figure 2.3: OTFT configuration of (a) TG/BC staggered device (b) BG/BC planar device. Shaded region encasing source and drain electrode is the SAM layer.

2.2 Substrate and Thin-Film Preparation

2.2.1 Substrate Preparation

Devices were fabricated on Corning glass (1x1 inch) substrates after a rigorous cleaning procedure involving ultrasonication at approximately 60 degrees in detergent (Decon, 3%), three individual stages in deionised water and a final stage in methanol. Each step involved sonicating for 30 minutes with the final methanol treatment performed for 10 minutes. Each glass substrate was rinsed with methanol and spun dry on using a spin-coater.

Electrode deposition of the source and drain contacts was evaporated by shadow masking at base pressures above 5 x 10^{-6} mbar and a rate of 0.2 Å/s, achieving a thickness of 40 nm. The same processing conditions were used for deposition of the gate electrode. Immediately after electrode deposition, the source and drain contacts were modified with the respective SAM treatment to avoid any possibility of degradation under atmospheric conditions. All thiols used in this work were used without any further purification. The source and drain contacts were submerged in the surfactant solution (10 mM in anhydrous IPA unless otherwise

stated) for 1 minute before being rinsed with copious amounts of solvent (anhydrous IPA) and spun dry or additionally annealed in air for 1 minute.

The organic semiconductors 6,13-bis(triisopropylsilylethynyl)-pentacene (TIPS-pentacene) and 2,8-difluoro-5,11-bis(triethylsilylethynyl)anthradithiophene (diF-TES-ADT) were purchased from Sigma Alrdich and used as received. The introduction of a polymer binder, poly(4-methylstyrene) (P4MS) with a M_w = 72,000 $g.mol^{-1}$, was used in a 4:1 organic semiconductor to polymer binder ratio dissolved in mesitylene (Sigma, 98%). This active-blend formulation was spin-coated using a two stage process (500 rpm / 15 seconds and 200 rpm / 60 seconds) with a total solids content of 2 wt%. Annealing of the semiconductor blend immediately afterwards was carried out for 1 minute at 100 °C in air. A fluorinated dielectric (Merck Chemicals Ltd – amorphous fluoropolymer) was then spin-coated on top and annealed for 2 minutes at 100 °C. The capacitance of the TG/BC dielectric was 1.70 nF/cm^2 and for the BG/BC dielectric was 2.50 nF/cm^2. Planar devices were encapsulated as an additional step using its corresponding dielectric. This was done to limit the exposure of the semiconductor to atmospheric conditions. The gate electrode (Au, ~ 40 nm) was deposited in the same manner as previously described source and drain contacts. All devices prepared and tested under ambient conditions and measured within a dark box.

2.2.2 Spin-Coating

Spin-coating is a quick and inexpensive solution processing method for the formation of thin-films which can be implemented under ambient and inert atmospheric conditions.[2] This processing method is highly advantageous for achieving uniform thin-film formation over small and large area substrates. Typically, the substrate is flooded with the formulation material covering the whole

surface prior to spinning. Whilst held in place under suction, the substrate is then spun on a rotating chuck to a specified rotational speed. Due to centrifugal forces, a relatively even thin-film can be achieved, however the resulting layer displays a strong dependence on the cleanliness, surface-energy distribution, and uniformity across the substrate. A high degree of molecular disorder can occur in spin-coated films, therefore control over spin speeds and adoption of post-treatment annealing steps can be implemented to promote more preferential order within the film. The evaporation rate of the solvent during spin-coating and its interaction with the substrate can influence the thickness and uniformity of the film.[3] Spin-coating is very wasteful with a large percentage of the starting material removed during the spinning process, albeit, a comparatively reproducible method for achieving a high yield of uniformity in OTFTs. Spin-coating can provide an element of control over the morphology and thickness of the layer but such physical parameters are more closely related to variables such as rotational speed, solution viscosity, material concentration and solubility, and solvent properties (e.g. boiling point and vapour pressure).

Several sections of the OTFT architecture were completed by spin-coating, specifically the SAM treatment, gate-dielectric, and organic semiconductor stages. Designated spin-coating parameters were adopted for each specified layer (optimised in-house by Merck Chemicals) which involved spinning between 1500 and 3000rpm from 30 – 60 seconds, with a post-treatment annealing step between 1 - 2 minutes at temperatures ranging from 75 - 200 °C. Heat treatment by annealing of the thin-film after layer formation is commonly adopted to help reorganise the morphology to induce preferential conditions aided by the removal of residual solvent and impurities. All processes were conducted under atmospheric conditions in

individually designated fume-hoods to avoid cross-contamination. All spin-coating was conducted with the cover to the lid removed. Humidity conditions in the laboratory played a significant factor when spin-coating and were duly noted. Preparation of the semiconductor in particular was strongly affected by humidity (optimal conditions below 50% humidity) and remaining solvent atmosphere within the fume-hood by previous users.

2.2.3 Organic Molecular Beam Deposition

Studies involving deposition of the metals (e.g. Ag) and organic materials (e.g. pentacene) for investigative purposes were thermally evaporated using an organic molecular beam deposition (OMBD) chamber at the University of Warwick. Under high vacuum conditions (c.a. 10^{-7} Torr), in which to ensure a clean growth environment, the starting material, in this case pentacene, was resistively heated within a Knudsen effusion cell (K-Cell) and deposited once sublimated forming a molecular beam from the resulting vapour pressure. In the instance of silver deposition, much higher thermal energy is required to achieve sublimation therefore a high melting point sources was used. The thickness of the resulting film was controlled by both a shutter and manual regulation of the source temperature. The deposition rate and thickness was monitored by an *in-situ* quartz crystal microbalance (QCM) in which the oscillating frequency of the QCM is sensitively measured for any mass increase (i.e. drop in frequency) related to the uptake of the sublimated material. Variations in the monitored to real film thicknesses can occur due to the lifetime of the QCM, positioning of substrates relative to the source, and the material density. This affects the accuracy of the computed thickness value, therefore tooling factors were extracted by *ex-situ* step-edge measurements using an atomic force microscopy (AFM) for calibration purposes.

2.3 Selected Techniques for SAM and Organic Semiconductor Characterisation.

An abundance of complementary experimental techniques available for studying SAMs has paved the way for in-depth understanding of their properties and characteristics at the molecular scale. Spectroscopic techniques (vibration and electron), scanning probe microscopy, and diffraction methods are frequently implemented tools when investigating SAMs present on surfaces.[4] Each experimental technique discussed henceforth has its own uniqueness in investigating the characteristics of SAMs.

2.3.1 X-ray Photoemission/Photoelectron Spectroscopy (XPS)

XPS is an electron spectroscopy chemical analysis technique commonly used to study the surface chemistry of materials. The sensitivity of this technique leads to its versatility as one of the more powerful methods for studying elemental surface concentration. Quantitative information of the surface chemical composition, chemical bonding, and electronic states within the material surface can be determined due to the binding energy of electrons and their relative intensities.[5] In this thesis, XPS measurements are used to characterise polycrystalline Au and Ag surfaces for changes in surface composition after various thiol treatments. The surface composition of the electrode is an important factor when discussing charge-injection at the electrode/semiconductor interface. The chemical properties and density of atoms present at the electrode surface, along with the nature of bonding at this surface can be useful when understanding OTFT device performance. Changes in elemental concentration of sulphur are investigated with regards to exposure time of the metal surface, and additional studies into the presence of oxygen and

formation of oxidative states due to high-temperature annealing of the thiol treated surface.

2.3.1.1 Theoretical background

The basis of this technique is described by Einstein's photoelectric effect, whereby incident photons interact with matter inducing electron emission from the atomic orbitals.[6] For electron ejection to occur the photon energy ($h\nu$) must be equal to or greater than the associated binding energy (E_b) of the electron. By meeting such requirements the transfer of energy from the photon is sufficient enough to remove the electron from the solid leading to photoemission. The kinetic energy (E_k) of such a photoelectron is represented mathematically by:

$$E_k \cong h\nu - E_b \qquad \textbf{Equation 2.3}$$

Calculated values of E_b are extracted from the measured kinetic energy associated with each photoelectron detected by the XPS analyser. This results in a characteristic set of peaks at specific binding energies associated with the atomic orbital of each element. Peak positions in the photoelectron spectra and relative intensities can provide information on elemental surface states and surface composition, respectively.

The kinetic energy of the emitted photoelectrons can be physically described by Einstein's photoelectric equation:

$$E_b = h\nu - E_k - \phi - E_{loss} \qquad \textbf{Equation 2.4}$$

where ϕ is the work function of the sample and E_{loss} are losses concerning instrumental energy losses and surface charging and relaxation effects. Removal of the term E_{loss} would mean the electron is unchanged after ionisation as explained by Koopmans Theorem.[7] E_b is a reference to the vacuum level, defined as 'energy zero' for the equation to meet the principle of energy conservation. The binding energy when plotted graphically is referenced to the Fermi level of the sample.

2.3.1.2 Instrumentation, Operation, and Analysis

A typical XPS instrument consists of an x-ray gun (Al Kα or Mg Kα), a monochromator, an analyser, and a detector, as depicted in **Fig.2.4**. The x-ray radiation is produced by the bombardment of charges onto an Al or Mg anode surface, with a resultant wavelength corresponding to photon energies of 1486.6 eV and 1253.6 eV, respectively. A monochromator is used to filter out unwanted satellite peaks leaving only the intense $K\alpha_1$ and $K\alpha_2$ doublet which are focussed onto the sample by a quartz crystal. Ejected electrons from the sample are selectively scanned depending on the pass energy (PE) of the electrostatic lenses. Only electrons which have a given energy (associated with that of the pass energy) are focussed on the hemispherical analyser entrance slit and therefore detected. A range of selected voltages applied to the lenses are set to detect photoelectrons of varying kinetic energies to create a spectral plot of the relative binding energies. Measurements are conducted under ultra-high vacuum (UHV) conditions due to the small diffusion length of x-rays.

Subtle differences in kinetic energy are related to different electronic environments which are characteristic of the state in which the atom exists. This can give powerful qualitative information in which elements of the same species exist on

the surface. An XPS spectrum commonly displays an ensemble of core-level peaks that can present asymmetrical features from spectral overlapping of closely associated binding energies. Resolving such features was done computationally by peak fitting in CasaXPS. Modelling of XPS data requires convolution of the experimental spectrum with specific computational functions for accurate replication. Line widths have been fitted by symmetrical Voigt functions with a variable Lorientzian-Gaussian line shapes (defined as the experimental outline), whereby the Gaussian function accounts for broadening effects caused by the instrument and the Lorentzian function for interactions at core-levels within the material. A Shirley-type background removal was also used to model stepping

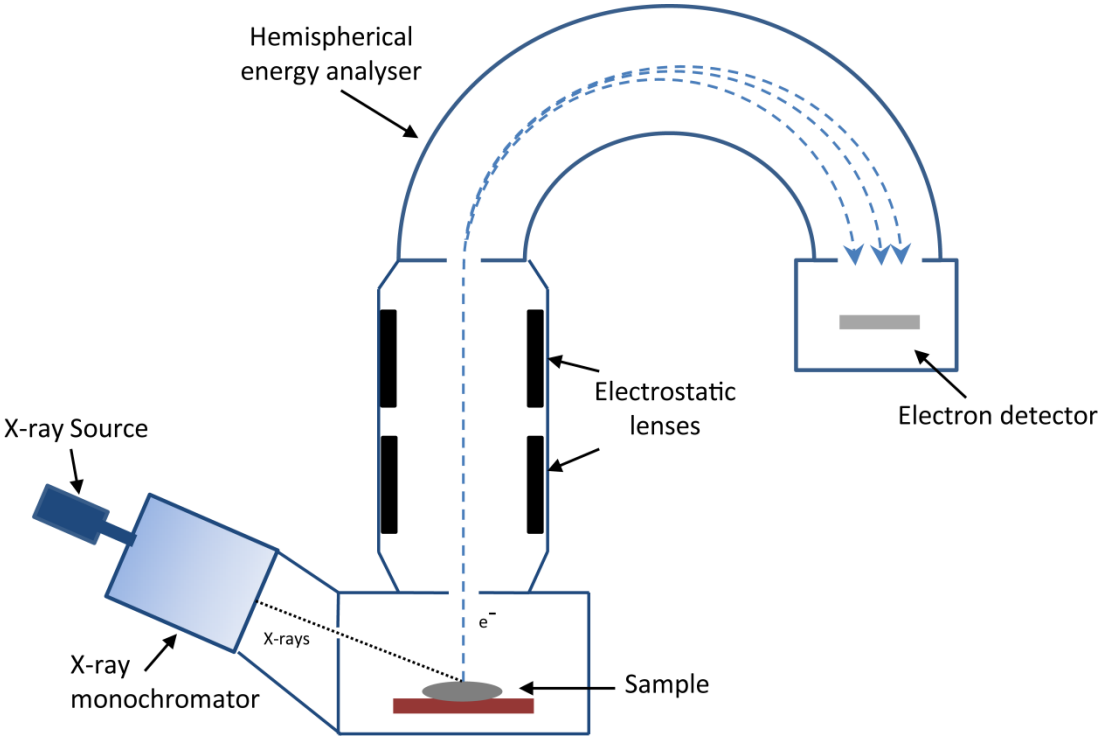

Figure 2.4: Schematic of XPS instrumentation with major components labelled.

features associated with inelastic scattering. Relative sensitivity factors (R.S.F) were taken from CasaXPS concerning specific elemental states (e.g. R.S.F for sulphur: $S_{2p3/2}$ = 1.11 and $S_{2p1/2}$ = 0.567). The accuracy of the resulting BE and FWHM is 0.02-0.03 eV.

XPS measurements were obtained using a monochromated Al K_α source (Omicron XM 1000, $h\nu$ = 1486.6 eV) and detected using an Omicron Sphera electron analyser. Electron binding energies were calibrated according to C(1s) 284.5 line for adventitious carbon. Atomic composition was calculated by measuring the area under each peak and its associated relative sensitivity factors.

2.3.2 Ultraviolet Photoemission Spectroscopy (UPS)

UPS spectra were obtained to determine the change in work function of the electrode (e.g. source and drain) upon SAM modification and the energy level alignment at the electrode/OSC interface. The work function of the metal (Φ_{metal}) contact can be measured using UPS through determining the Fermi level, E_F, and the energy of the secondary electron cutoff $\left(E_{cutoff}\right)$.[8] The work function of the metal can be extracted from the kinetic energy spectra by the following equation:

$$\Phi_{metal} = h\nu - (E_F - E_{cutoff}) \qquad \textbf{Equation 2.5}$$

UPS spectra were obtained using a He (I) plasma source (Omicron VUV Lamp HIS 13, $h\nu$ = 21.21 eV) for excitation of the sample. A 10 V bias was applied between the sample and the detector to improve the transmission of low kinetic energy electrons to improve identification of the low energy cutoff. An analyser take-off angle of 90 degrees and a pass energy of 10 eV was employed for both UPS and XPS measurements. All samples were prepared *ex-situ* and placed under N_2

after surface modification before being transferred for analysis, conducted *in-situ* under UHV base pressures of c.a. 10^{-11} Torr.

2.3.3 Raman Spectroscopy

2.3.3.1 Theoretical background

Raman spectroscopy is a non-destructive optical technique based on the emission of radiation due to the inelastic scattering of phonons. A monochromatic source (typically a single wavelength laser) has the majority of its photons elastically scattered, conversely a small amount of photons undergo inelastic scattering different to that of the incident photon frequency. This interaction of inelastic photons with a molecule leads to changes in its polarisability which causes elemental vibrational excitations. Relaxation of electrons after excitation releases photons with an energy change equal to the vibrational energy of the molecule. The line shape and position of the Raman bands are determined by the chemical composition and crystalline structure of the sample, being highly sensitive to changes due to crystal defects (e.g. grain boundaries, polymorphs), impurities (e.g. oxidation), and strain.[5] This makes Raman spectroscopy sensitive to subtle structural changes between crystalline polymorphs in organic semiconductors. This spectroscopic technique is highly versatile in its application. It can be used to study vibrational, rotational and other low-frequency deformation modes which can also be represented by image mapping of the Raman spectra.

2.3.3.2 Instrumentation and operation

A schematic layout of the Raman spectrometer is shown in **Fig.2.5**. A single wavelength of laser light (e.g. 514.5 nm; 785 nm) is impinged on a sample undergoing vibrational excitation associated with the Raman effect. The laser source

is focussed on the sample using an optical microscope (allowing for high spatial resolution) with scattered radiation collected at 180° (backscattered geometry). The scattered light is collected by lenses and subsequently passes through a filter which removes wavelengths associated with elastically scattered light (i.e. laser energy), leaving only the inelastically scattered signal (i.e. Raman light) from the sample. This passes through two holographic notch filters and subsequently focussed onto a single 1200 l/mm diffraction grating (used specifically for 514.5 nm) for splitting of the Raman scattered light into its constituent wavelengths. Finally, the light is detection by a back-illuminated CCD. Plotting the intensity of the collected scattered light against the excitation/emission energy difference yields a Raman spectrum.

All Raman results were taken using an inVia Renishaw spectrometer at room temperature. Raman scattered photons were generated using 10 mW of laser power at the sample surface produced by an Ar^+ ion laser operating at 514.5 nm in a 180° backscattering geometry. The laser power was reduced according for studying organic semiconductors to minimise thermal damage to the material. The spatial resolution of the beam spot was c.a. 1 μm. The spatially resolved measurements were obtained using a 50x objective Leica microscope. A holographic grating (1800 lines/mm) was used to achieve the high resolution spectra. Raman mapping measurements were conducted using the line-scan method, Streamline^{TM}. Raman images were generated using WIRE 3.3^{TM} software (Renishaw). Unwanted fluorescence from overhead light sources was eliminated by covering of the eyepieces during each measurement. Measurements conducted at the University of Warwick were calibrated manually (Si = 520.5 cm^{-1}), whereas Raman imaging conducted at Merck Chemicals Ltd was equipped with an inbuilt calibration stage.

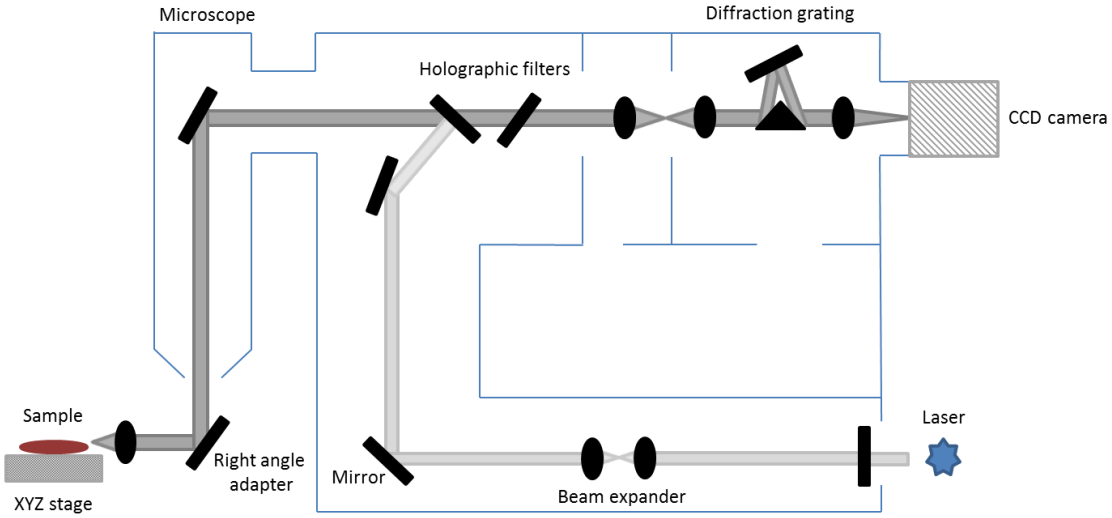

Figure 2.5: Schematic representation of Raman spectrometer.

A technique adopted for studying SAMs on metal surfaces was Surface enhanced Raman spectroscopy (SERS). This unique characterisation technique provides greatly enhanced Raman scattering from molecules that have been adsorbed onto specially prepared metal surfaces.[5] The enhancement factor for SERS substrates can be as high as 10^{11} due to the surface signal overcoming that of the bulk. The surface enhancement is a combination of a local enhancement of the electromagnetic field (e.g. surface plasmon effect) and contributions from chemical interactions between the molecule and the metal surface.

2.3.4 Atomic Force Microscopy (AFM)

The atomic force microscope is an example of a scanning probe microscope. The technique was developed in 1986 and has become a widely used surface analysis method for obtaining 3D topological surface images.[9] An AFM is highly versatile due to the ability to image both conducting and insulating materials which can be performed with atomic resolution. All micrographs in this thesis were performed using tapping-mode (aka. AC mode) using an Asylum Research MFP-3D. Tapping-mode involves intermittent contact of the tip with the sample surface, which is commonly adopted for organic thin-films and polymers to minimise surface damage

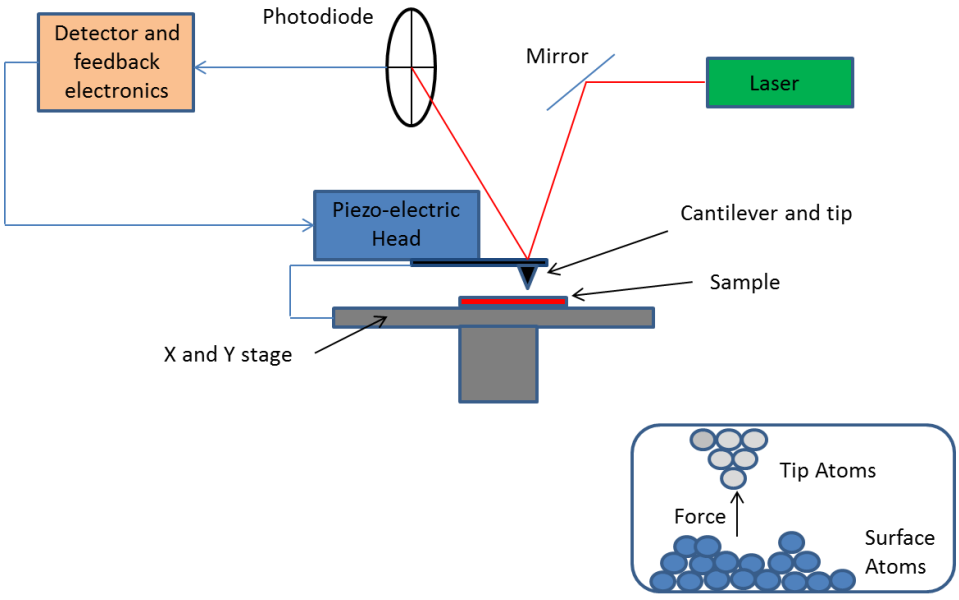

Figure 2.6: Schematic representation of an AFM. Inset displays the interaction between the tip and surface.

of these soft materials. An atomically sharp tip (typically made of Silicon or Silicon Nitride) vibrating near to its resonant frequency is positioned within an order of tens

to hundreds of Angstroms above the sample surface. On approach to the surface the vibrating tip is heavily influenced by attractive forces due to their long distance dependence (e.g. electrostatic and Van der Waals) but as the tip moves closer the repulsive forces (e.g. electron-electron Columbic interactions) now dominate. The amplitude of the oscillating tip is dampened by its interaction with the surface and corrected by a feedback loop that changes the z-position of the cantilever base in order to maintain a constant amplitude (set point). These changes in the z-position give a direct measurement of the sample topography. All micrographs were analysed and reconstructed using Igor Pro. A scheme of an AFM is shown in **Fig.2.6**.

2.3.5 Kelvin Probe

The Kelvin probe technique was developed in 1861 by Lord Kelvin. The technique comprises of a vibrating probe (typically Au) brought in close proximity with a conducting sample to form a capacitor, where the work function (ϕ) difference between the sample and vibrating tip can be measured in a non-contact and non-destructive way.

Prior to electrical connection, the sample and probe share the same vacuum energy level, shown in **Fig.2.7(a)**. When put in close proximity and connected electrically, equal and opposite charges accumulate on the surface of the two metals forming a capacitor. The transport of electrons now flow from the metal possessing the higher E_F to the lower E_F, leading to the alignment of the E_F between the sample and vibrating/oscillating tip, shown in **Fig.2.7(b)**. Through monitoring of the output voltage of the formed capacitor a sinusoidal waveform is seen which periodically oscillates from a peak-to-peak voltage determined by the capacitor potential. The internal potential drop ($\Delta\Psi$) or contact potential difference (CPD) between the two

metals is now equal to the difference in their work function. Through application of an external bias (compensating voltage) a nulling point will be seen where all surface charges will disappear, therefore no further charge flow between the two metals, and a flattening of the oscillating waveform occurs, shown in **Fig.2.7(c)**. The voltage applied to reach this nulling point is equal to the CPD (mV), which is equivalent to the difference in the work function (eV) of the metals and can be taken as the work function value of the sample once correlated to a known reference.

All measurements were conducted under nitrogen conditions and referenced to a freshly cleaved highly oriented pyrolytic graphite (HOPG) substrate with an absolute value of 4.475 eV.[10] The make of Kelvin probe was a Besocke Delta Phi. The accuracy of work function readings was ±10mV with average readings along the sample surface being performed for all results.

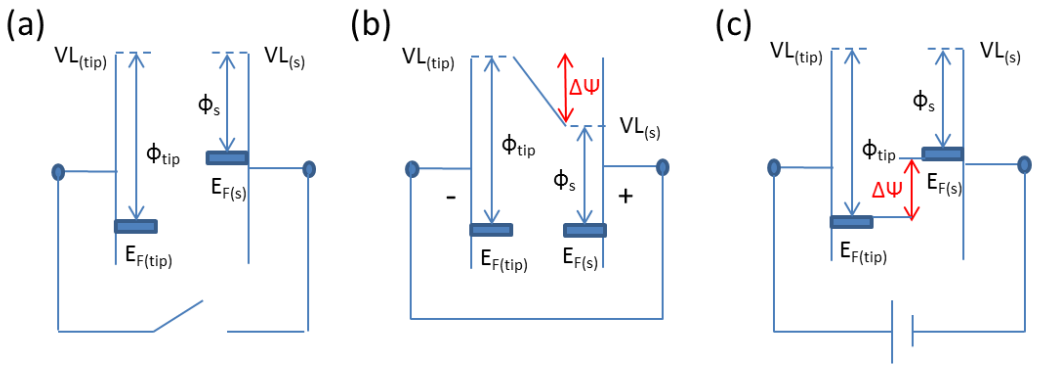

Figure 2.7: Schematic diagram of the kelvin probe technique in terms of a parallel plate capacitor, with (a) no potential, (b) short-circuited, and (c) with a DC voltage.

2.3.6 Contact Angle Analysis

Contact angle analysis is a surface tension technique whereby a quantitative measure of the wetting of a liquid on a solid surface can be studied by the contact

angle (θ) produced at this interface. Characteristic properties of the surface (e.g. surface energy) can be investigated to deduce the solids wettability. A contact angle can be regarded as the measure of the attraction between molecules within the probing droplet against the attractive or repulsive forces it experiences at the surface. The contact angle can be defined geometrically as the angle formed by a liquid at a three phase boundary where a liquid, gas and solid intersect as illustrated in **Fig.2.8**. The contact angle in terms of surface tension (γ) can be given by the Young equation:

$$\gamma_{SV} = \gamma_{SL} + \gamma_{LV} \cos\theta \qquad \textbf{Equation 2.6}$$

where solid (S), liquid (L) and vapour (V) in the **Eqn.2.6** represent the three phases.

A large contact angle exemplifies a hydrophobic surface with low surface energy as shown in **Fig.2.8(a)**, whereas a small contact angle indicates the surface is

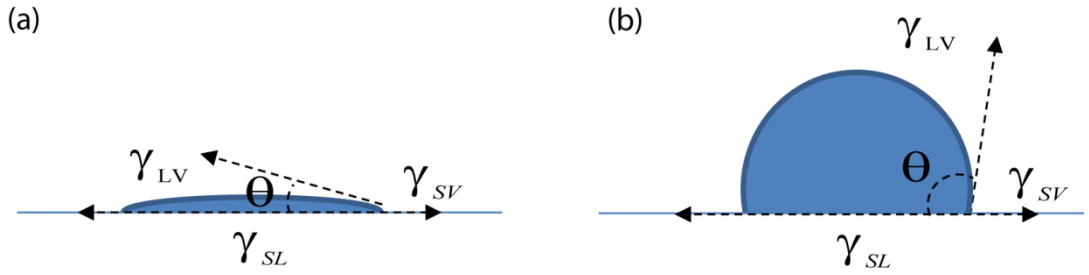

Figure 2.8 Scheme representing static water contact angle (θ) formation on surfaces of different wettability: (a) hydrophobic surface, and (b) hydrophilic surface. The surface tension at each interface is denoted by γ_{SL} at the solid/liquid, γ_{SV} at the solid/vapour, and γ_{LV} at the liquid/vapour.

hydrophilic and has a high surface energy, as demonstrated in **Fig.2.8(b)**. Hydrophobicity is a repulsive force between non-polar molecules and water, while

hydrophilicity of a surface is associated to its affinity to water and its ability to form H-bonds (i.e. typically due to the presence of polar molecules). Common materials used as substrates (e.g. glass) or gate-dielectrics (e.g. SiO_2) in organic transistor design display hydrophilic properties. Additionally, oxygen plasma treatment results in the formation of polar constituents which leads to increasingly hydrophilic surface properties.

The surface energy of source and drain electrodes, and additionally the substrate and gate-dielectric regions exposed within the channel of the transistor, specifically for bottom contact devices, strongly influence the assembly of the subsequently deposited organic semiconductor. It is strongly regarded that low surface energy properties (i.e. energetically stable) of these regions are preferential for favourable molecular assembly of the semiconductor.

Surface energy values were calculated by a First Ten Angstrom drop shape goniometer (FTA1000) using static contact angle measurements of both deionised water and diiodomethane (MI) for evaluation of the dispersive and polar components. The surface energy was exacted using the Owens-Wendt Method (geometric mean combining rule) represented by the following equation:

$$1+\cos\theta = 2\left(\gamma^{d}{}_{S}\gamma^{d}{}_{L}\right)^{0.5} / \gamma_L + 2\left(\gamma^{h}{}_{S}\gamma^{h}{}_{L}\right)^{0.5} / \gamma_L \qquad \textbf{Equation 2.7}$$

Solving simultaneously with known polar and dispersive values for both testing liquids yields the respective components. The values for γ^{d}_{L}, γ^{h}_{L} and γ_L were 21.8, 51.0, and 72.8 mN/m for water, and 49.5, 1.3, and 50.8 mN/m for diiodomethane (MI) respectively.[11]

Contact angle measurements were conducted using a sessile drop technique. Profile extraction was conducted within 10 seconds of droplet formation and averaged over three individual measurements. The contact angle resolution was ±0.01 degree.

2.3.7 Gas Chromatography-Mass Spectroscopy (GCMS)

This technique is capable of measuring the relative molecular mass of molecules enabling the associated molecular weight to be obtained.[12] The fragmentation of the excited species produced by ionisation of the molecule offers insightful information into the composition of the intact molecule.[12] The basics of mass spectroscopy was first demonstrated by Wien in 1898.

Individual molecules of a sample are bombarded with high energy electrons which cause the ejection of one or more electrons from the sample (called electron impact ionisation). This interaction with the molecule causes all electrons associated with it to be removed causing its ionisation to a radical cation. The resulting positively charged ions are accelerated (by an electrical potential) through an analyser which causes their deflection due to the magnetic field (Note: degree of deflection is dependent upon the charge of the molecule and magnetic field strength) and resultant collection at the detector.

2.3.8 Secondary Ion Mass Spetroscopy (SIMS)

Secondary ion mass spectroscopy (SIMS) involves the bombardment of a sample surface with a primary ion beam followed by mass spectroscopy of the emitted secondary ions. SIMS is widely used for analysis of trace elements in solid materials, especially semiconductors and thin-films. During SIMS analysis, the

sample is slowly sputtered away resulting in ion fragmentation patterns which contain information useful for identifying molecular species. The bombarding primary ion beam produces monatomic and polyatomic particles of the sample material and resputtered primary ions, along with electrons and photons. The secondary particles carry positive, negative, and neutral charges which possess kinetic energies ranging from zero to several hundred eV.[13]

Two primary beam species, O_2^+ and Cs^+, were used to investigate the organic semiconductor, which increase the ion yield of positive and negative secondary ions respectively. The O_2^+ incident ion had a beam energy of 250 eV and c.a. 40 nA with take-off angles of 0° and 45°. The Cs^+ ion source had a beam energy of 500 eV and c.a. 17 nA with a take-off angle of 45°. A scan area of 400 x 400 μm was studied for all samples. A quadrupole mass spectrometer is used to detect specific mass-to-charge (m/z) ratios of the secondary ions produced from the sample.

Monitoring of the secondary ion count rate of selected elements as a function of time with continuous ablation of the sample can provide depth profiles when combined with height profile data of the resultant crater. Interpretation of the SIMS data can lead to erroneous depth profiles if the sample consists of several different materials. Sputter rates in SIMS vary between 0.5 and 5 nm/s which depends on the primary beam intensity, sample material, and crystal orientation. This can lead to inaccuracies in the depth profile if fluctuations in the sputter rate occur. Several other reasons can cause issues when creating such profiles. Sputtering effects can cause atoms from the surface to be driven into the sample (c.a. 10 nm) causing elongation of the SIMS analysis profile over time. The polycrystalline nature of the organic semiconductor studied in this thesis can cause rough crater bases (formed from the impinging primary beam) due to the differential sputter rates that depend on crystal

orientation. Additionally, the ion yield (i.e. the fraction of sputtered atoms that become ionised) can vary over several orders of magnitude for various elements. Due to variability in ionisation efficiencies for different elements tailored analysis conditions are required which is determined by the chemical composition of the sample. As a result of this depth profiling was not adopted to explain the results in this thesis.

Preparation of the sample material under ambient conditions leads to the heightened likelihood of atmospheric contaminants present at interfaces within the sample. The presence of oxygen in the sample can enhance positive ion yields for most elements, while fluorine exhibits anomalously high positive ion yields in nearly all samples. This leads to irregularities in the ionisation potential with secondary ion yield when using O_2^+. Due to these reasons and the presence of fluorine in the sample (i.e. fluorinated thiols) Cs^+ was adopted as the primary ion beam.

Ultralow energy SIMS measurements were carried out using an Atomika 4500 quadrupole instrument (similar to other Atomika/Cameca) conducted at the University of Warwick.[14]

2.3.9 X-ray Diffraction (XRD)

X-ray diffraction (XRD) provides information on crystal structure properties, orientation, and molecular spacing for both single-crystal and polycrystalline materials. Crystals are periodically arranged in unit cells forming a lattice, where the distance between atoms (or molecules) within the array can be resolved into atomic planes as a result of this interplanar spacing, which is defined as the d-spacing (shown in **Fig.2.9**). Diagrammatically, atoms are used in the below representation as scattering points, although Bragg's Law applies to scattering centres consisting of

any periodic distribution of electron density (e.g. molecules or collection of molecules).

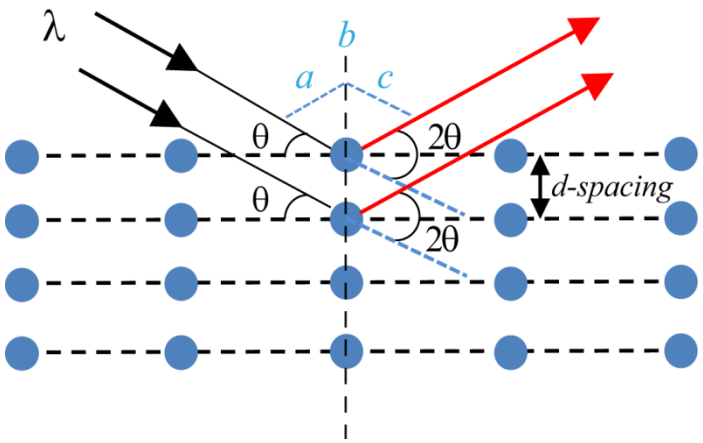

Figure 2.9: Schematic representation of Bragg diffraction. Atoms are represented by blue circles, and lattice planes by horizontal dashed lines. θ is the scattering angle, λ is the wavelength of the incident light (where $\lambda = 2d\sin\theta$).

The exact electron wavelength for bulk diffraction in crystals with perfect periodicity is sensed in the direction normal to the surface with the reciprocal lattice rods becoming associated with discrete intensity maxima. When the impinging x-rays satisfy Bragg's Law (**Eqn.2.8**), constructive interference occurs and a peak intensity appears.

$$n\lambda = 2d\sin\theta \qquad \textbf{Equation 2.8}$$

In three-dimensional crystals, Bragg diffraction is satisfied simultaneously in the x-, y-, and z-directions, where the path length difference (ab + bc) of two parallel waves from the same lattice plane equates to an integer multiple of the wavelength of the incident radiation. This is defined mathematically in **Eqn.2.8** by the integer *n* which represents the order of the diffraction peaks. The dimensions of the unit cell are described by three axes: the lengths a, b, c, and the angles between

them alpha, beta, and gamma (shown in **Fig.2.10**). The points at which the plane lengths intercept the unit cell axes can also be defined by Miller indices (*hkl*) represented by three integers $1/h, 1/k, 1/l$. Only crystallites having reflecting planes (h, k, l) parallel to the specimen surface will contribute to the reflected intensities.[6] The peak positions, intensities, line-widths (i.e. area under the peak) and peak shape provide information regarding the dimension of the unit cell when the d-spacing and indices h, k, l are known. The d-spacing can be extracted by using Bragg's law as it is a function of 2θ and subsequently the crystal structure can be resolved.

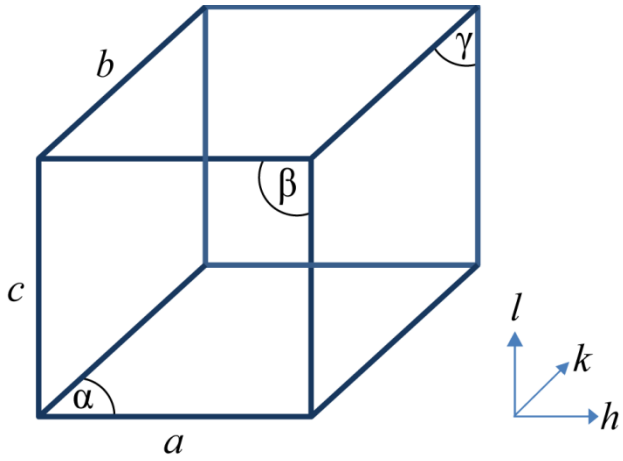

Figure 2.10: Lattice parameters of a unit cell with lengths (a,b,c) and angles (α, β, γ), alongside the corresponding Miller indices (*hkl*).

Powder XRD in reflection geometry was used for all diffractograms discussed in this thesis. Due to most organic thin-films displaying polycrystalline features when processed from solution, this leads to randomly orientated crystalline domains of varied sizes and various molecular orientations within the bulk of the material. XRD diffractographs were taken using a Philips PANalytical x'pert Pro

MPD diffractometer. The x-ray detector was rotated at an angle 2θ (the glancing angle) for collection of the diffracted x-rays (typical angles from ~ 5° to 70°).

2.4 References

[1] J. Zaumseil, H. Sirringhaus, *Chemical Reviews*, (2007) **107**, 1298.
[2] D. B. Mitzi, L. L. Kosbar, C. E. Murray, M. Copel, A. Afzali, *Nature*, (2004) **428**, 299.
[3] D. E. Bornside, R. A. Brown, P. W. Ackmann, J. R. Frank, A. A. Tryba, F. T. Geyling, *J. Appl. Phys.*, (1993) **73**, 585.
[4] C. Vericat, M. E. Vela, G. Benitez, P. Carro, R. C. Salvarezza, *Chem. Soc. Rev.*, (2010) **39**, 1805.
[5] J. Xu, Y. Diao, D. Zhou, Y. Mao, G. Giri, W. Chen, N. Liu, S. C. B. Mannsfeld, G. Xue, Z. Bao, *J. Mater. Chem. C.*, (2014) **2**, 2985.
[6] G. A. Attard, C. J. Barnes, Surfaces, Oxford University Press, (1998).
[7] R. Schlaf, B. A. Parkinson, P. A. Lee, K. W. Nebesny, N. R. Armstrong, *J. Phys. Chem. B.*, (1999) **103**, 2984.
[8] D. Cahen, A. Kahn, *Adv. Mater.*, (2003) **15**, 271-277.
[9] G. Binnig, C. F. Quate, C. Gerber, *Phys. Rev. Lett.*, (1986) **56**, 930.
[10] W. N. Hansen, G. J. Hansen, *Surf. Sci.*, (2001) **481**, 172.
[11] G. Strom, M. Fredriksson, P. Stenius, *Journal of Colloid and Interface Science*, (1987) **119**, 352.
[12] L. M. Harwood, T. D. W. Claridge, (1997) *Introduction to Organic Spectroscopy*, Oxford University Press.
[13] P. Williams, *Ann. Rev. Mater. Sci*., (1985) **15**, 517.
[14] R. J. H. Morris, M. G. Dowsett, R. Beanland, A. Dobbie, M. Myronov, D. R. Leadley, *Anal. Chem*., (2012) **84**, 2292.

Chapter 3

Characterisation of Self-Assembled Monolayers of Aromatic Thiols on Silver

This chapter explores the changes in work function, surface energy, and surface composition of aromatic thiols on Ag in relation to their time for self-assembly and post-treatment processes. Particular emphasis is focussed on pentafluorobenzenethiol (PFBT) due to its widespread use in OTFTs and 4-fluorothiophenol (4-FTP) owing to its excellent OTFT performance achieved in this work as discussed in **Chapter 4**. There are significantly few studies discussing the electronic and chemical characteristics for short immersion times and how low coverage of benzenethiol derivatives affects the electronic-state of the molecule-metal interface, therefore this chapter primarily focuses on immersion times of 1 minute for comparative purposes. A general consensus for SAM preparation is the implementation of long immersion times to ensure self-assembly has sufficient time to achieve reasonable coverage of the target surface or the completion of a monolayer. A timescale in excess of 24 hours is commonly adopted but such longer assembly times are unfeasible for industrial and R&D purposes and is subsequently a major focal point. Additionally, post-treatment processes after self-assembly are discussed regarding their influence on the interface energy and electronic and chemical properties through annealing at temperatures above 100 °C. The impact of these process parameters will be discussed in this chapter.

3.1 Introduction

Achieving an ohmic contact between a metal and an organic semiconductor is ideal for unimpeded charge-injection. This type of interface can be defined as ideal when current flows with a negligible voltage drop. Enhanced charge-injection has been measured for polymers,[1] and evaporated thin-films,[2] through matching of the work function of the electrode to the associated frontier molecular orbital of the semiconductor. This approach appears simplistic but in OTFTs this energetic arrangement can be dependent upon the electronic properties of the organic semiconductor, device configuration and environmental conditions (e.g. bias, light, temperature, humidity). Organothiols used as SAMs can aid in controlling this energy alignment at the metal/organic semiconductor interface to a certain extent. A thiol which possesses an intrinsic dipole moment can be covalently bonded to a metal surface for systematic modulation of the vacuum level, E_{vac}, represented pictorially in **Fig.3.1(a)**. The directional nature of the dipole moment results in an interfacial electric field formed at the electrode surface in which the total dipole moment (μ_{NET}) increases (i.e. μ_{NET} directed towards the substrate) or decreases (i.e. μ_{NET} directed away from the surface) the E_{vac} outside of the electrode relative to the Fermi level, E_F. This is depicted in **Fig.3.1(b)**, where the dipole moment points away from the surface leading to an increase in work function and vice versa. A monolayer can be visualised as a 'tightly bound' dipole sheet at the metal surface as, for fluorinated thiols, a sheet of positive charges reside close to the substrate surface and a sheet of negative charges reside towards the monolayer/air interface. This represents an increase in the work function, where the opposite polarity leads to a decrease in the work function.[3] The total dipole moment, μ_{NET}, can be divided into

two constituent parts. The first is the residual surface dipole or bond-dipole, μ_{BD}, which is due to the chemical bonding of the modifier, and the second is the

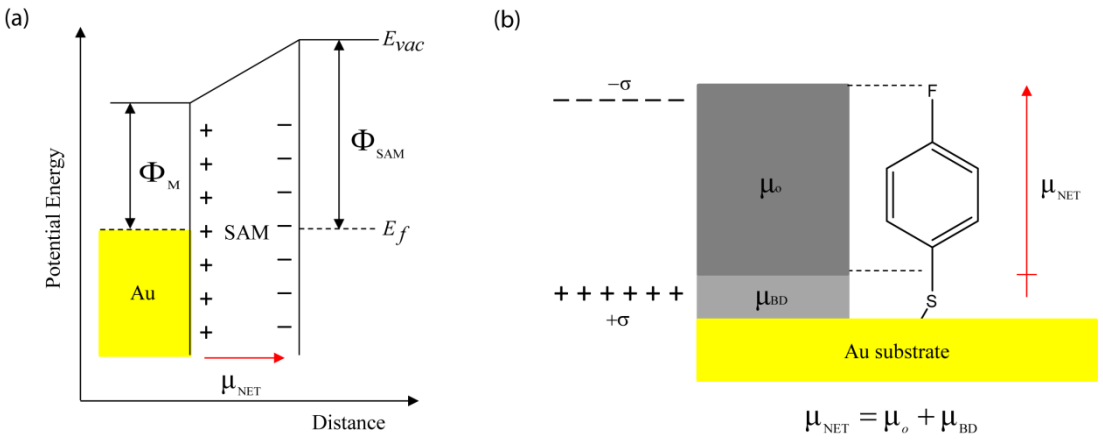

Figure 3.1: (a) Schematic diagram of the work function shift due to the formation of a SAM and (b) schematic representation of a thiol as a charged double layer.

molecular dipole, μ_0, which is induced by the attached modifier and dictated by its auxiliary and terminal-group. The geometric rearrangement of the bound modifier can also be classified as a third dipole component as changes in the surface geometry after chemisorption can influence the magnitude and direction of the dipole, which contributes to the extent of the work function modulation. A variation in angular tilt relative to the electrode surface influences the packing density of the monolayer, where different auxiliary groups will present different orientational properties due to their size and length. The magnitude and directional properties of the dipole are known to be dependent upon the degree of polarity which is strongly influenced by the charge distribution within the molecule.[4]

The surface density of thiolates covering the electrode surface is an important parameter in determining the magnitude of the work function shift ($\Delta\Phi$) and the interfacial surface tension (IFT). The work function shift associated with the thiolate

can be directly related to the net component of the molecular dipole moment (μ_{NET}) normal to the surface by the following equation:

$$\Delta\Phi = \frac{\mu_{NET}}{\varepsilon\varepsilon_o A} \qquad \textbf{Equation 3.1}$$

where A is the surface area per molecule, ε is the relative permittivity of the monolayer (e.g. an effective dielectric constant of ~5 is estimated for aromatic molecular monolayers)[5] and ε_o is the vacuum permittivity of free space.[6] The change in work function is related to the sign of the dipole moment where an increase in work function is associated with a $\mu_{NET} > 0$, and vice versa.

3.2 Results and Discussion

3.2.1 Work Function Influence of Self-Assembled Monolayers

The chemical structures of the organothiols used in this work are presented in **Fig.3.2**. Due to the interest of charge-injection, auxiliary groups formed of aromatic moieties were chosen due to their conductive conjugated nature as opposed to aliphatic thiols which exhibit insulating properties, particularly at long chain lengths. The organothiols studied in this work are all derivatives of thiophenol (TP) with varying degrees of electron withdrawing behaviour, which as a result present a range of different intrinsic dipole moments and subsequent work function shifts. All experimental work within this chapter was done using Ag. The head-group (e.g. -SH) and auxiliary group were kept the same with only variations in the electron withdrawing component of the functional terminal-group. As a comparative study, TP was also investigated and used as a reference to other aromatic thiols due to its similar fundamental properties. Due to the electron donating nature of TP it is

undesirable for achieving efficient hole-injection in *p*-channel OTFTs as its μ_{NET} points towards the metal surface corresponding to a decrease in the work function.

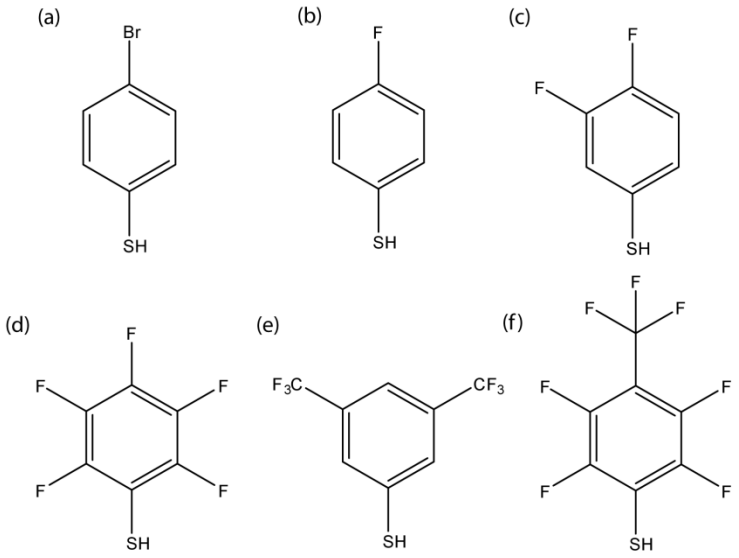

Figure 3.2: Chemical structures of thiols used: (a) 4-bromothiophenol (4-BTP), (b) 4-fluorothiophenol (4-FTP), (c) 3,4-difluorothiophenol, (d) pentafluorobenzenethiol (PFBT), (e) 3,5-Bis(trifluoromethyl)benzenethiol (BTFMBT), (f) 2,3,5,6-Tetrafluoro-4-(trifluoromethyl)benzenethiol (TFTFMBT).

Fig.3.3 shows the experimentally measured variation in work function conducted by Kelvin probe and the direct influence of post-treatment annealing of the functionalised surface. A summary of all work function values alongside density functional theory (DFT) calculated free molecule dipole moments for each organothiol are tabulated in **Table 3.1**. There appears to be no trend between the work functions of 4-bromothiophenol (4-BTP) and 4-FTP with their associated dipole moment, as the increased electronegativity of the fluorinated polar molecule should induce a larger work function shift. Instead, the work function shift of 4-BTP was ~0.2 eV higher than 4-FTP. It is important to note that $\Delta\Phi$ is not directly

proportional to μ_{NET} and such correlations will become influenced by external factors as previously discussed. It is plausible that variation in the orientation of the organothiol normal to the surface could lead to changes in molecular tilt, causing deviations between the corresponding work functions. This would be expected for a disordered SAM as differences in packing and structural formation of the thiolate on the Ag surface may have an overriding influence.

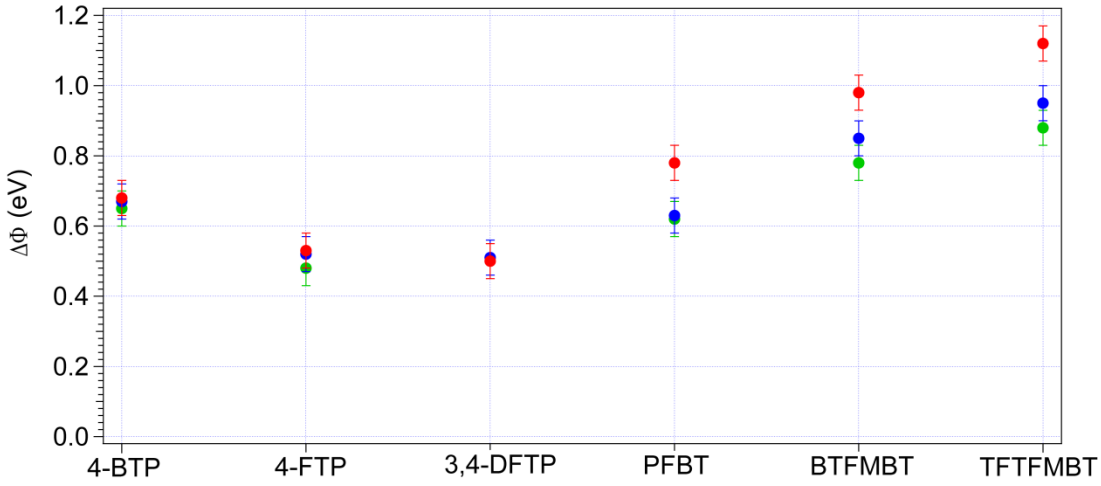

Figure 3.3: Experimentally measured work function shifts of six different organothiols after post-treatment steps of rinsing of the electrode (green) and two annealing treatments of 100 °C (blue) and 140 °C (red) All values are referenced to oxidised Ag (Φ = 4.7 eV).

Due to the high potential for Ag to oxidise measurements were conducted to investigate the $\Delta\Phi$ of the bare Ag surface with exposure to atmospheric conditions. A shift in the Ag work function was observed from exposure to the atmosphere, as shown in **Fig.3.4**. An initial value of 4.25 eV was measured for non-exposed Ag surface stored and measured under N_2 environment, where this value increased to a constant value of 4.70 eV when measured after 15 minutes, with no change in its

value with further exposure. Oxygen-induced changes on Ag(111) surfaces has been detected to increase the surface work function, with associated changes in work function dependent on the relative coverage.[7] Due to this oxidation period, freshly

Table 3.1: Dipole moment (from DFT calculations) compared with the experimental work function shift. Calculation Method (RB2LYP); Basis set (6-311+G(d,p)). [8,9]

Sample	Dipole Moment (D)	Φ_{RT} (eV)	$\Phi_{100\,°C}$ (eV)	$\Phi_{140\,°C}$ (eV)
Ag (bare)	-	4.72	4.72	4.72
TP	-1.88	0.32	0.30	0.24
4-BTP	1.02	0.68	0.69	0.68
4-FTP	1.09	0.48	0.52	0.52
3,4-FTP	1.23	0.50	0.50	0.50
PFBT	1.77	0.68	0.70	0.78
BTFMBT	2.70	0.78	0.86	0.96
TFTFMBT	3.11	0.88	0.94	1.12

evaporated polycrystalline Ag samples which spent only a few minutes in atmospheric conditions displayed slightly lower work functions shifts (~0.2 eV) compared with longer atmospheric exposed samples, causing discrepancies when referring to the exact work function of the reference sample. The presence of contamination may affect the adsorption of modifiers since they are occupying adsorption sites.[10] Post-treatment annealing under atmospheric conditions displayed increased variations in the work function for all organothiols investigated. Subtle increases in work function of < 0.1 eV for 4-BTP, 4-FTP and 3,4-DFTP were observed with more substantial rises of > 0.1 eV in work function for PFBT, BTFMBT, TFTFMBT. Continuous observation of the work function for samples measured immediately after heat treatment displayed drift in the oscilloscope signal, which revealed higher than normal work functions that decreased, stabilising close to their expected values after a period of ~5 minutes. Cooling of the sample after

annealing may have influenced this gradual decrease in the work function. It is probable that the process of annealing caused instability in the surface work function. With this considered all values stated in **Fig.3.3** displayed no drift in the oscilloscope signal and were assessed as stable before the reading was taken. All samples were transferred after annealing in air to a nitrogen filled glove box and left

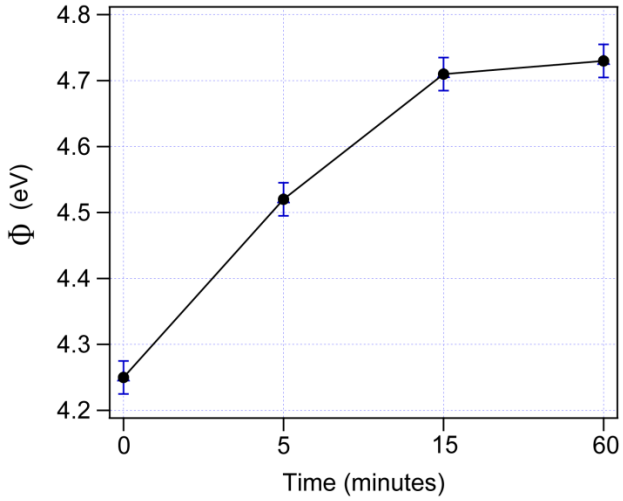

Figure 3.4: Work function shift of bare Ag with exposure to atmospheric conditions. A time of zero minutes implies no exposure to air. All measurements were conducted under N_2 environment using a Kelvin probe.

for more than 10 minutes before being measured. Additionally, repeat measurements conducted in 15 minute intervals showed minimal deviation from the initial result and were averaged over at least three regions on the substrate.

Work conducted by Kang *et al*. studied the effects of annealing PFBT while in solution which enhanced its packing density on Au(111) surfaces at temperatures < 100 °C for periods of up to 2 hours.[11] Furthermore, the rate of adsorption has shown to increase by this approach at temperature below the boiling point of the solvent.[10] Due to the short annealing period it is unrealistic to assume the thermal energy will significantly influence the surface reorganisation of the thiolate to induce

such an increase in work function. Contributing factors may be more closely related to increased oxidation of the Ag surface, the increased presence of oxidised sulphur, desorption of multilayers or residual solvent, or removal of adventitious carbon and the pillow-effect it induces on the electron cloud at the metal surface. Multilayer formation may disrupt the molecular dipole at the interface causing charge traps and decreased charge transfer across the interface.[10]

The work function was also measured by ultraviolet photoelectron spectroscopy (UPS) determined from the width of the corresponding UP-spectra (i.e the difference between the secondary electron cut-off, E_{SECO}, and the Fermi level). The organothiols PFBT and 4-FTP were measured by UPS and referenced to Ag, with their corresponding spectra plotted in **Fig.3.5**. The results from UPS show minmal fluctuation in the work function for 4-FTP from 1 minute to 16 hours, although a relative decrease in work function was observed for PFBT with longer immersion. The trend observed for 4-FTP measured by UPS matches with measurements conducted by Kelvin probe showing little change in its work function with time. The result for PFBT is surprising as the work function was seen to increase with longer immersion time by Kelvin probe. Immediately after the UPS measurements all samples were measured by Kelvin probe for comparision. The 4-FTP samples produced a work function value of 5.23 eV for both 1 minute and 16 hours, whereas the PFBT samples gave values of 5.37 eV and 5.78 eV for 1 minute and 16 hours, respectively. A summary of all results measured by UPS and Kelvin probe are tabulated in **Table 3.2**.

The static water contact angle was also investigated for PFBT and 4-FTP with varied immersion times. The 4-FTP modified surfaces displayed contact angles consistently < 90° with no discernible difference between time scales, although

PFBT fluctuated with contact angles displaying values > 100° with longer immersion times compared with 1 minute samples which were mainly < 90°. This appears to signify a longer surface reorganisation time for PFBT. Insightful work conducted by Azzam *et al.* has shown by STM a long transitional period associated with PFBT in saturating Au(111) surfaces.[12] Immersion times of 190 hours produced well-ordered, defect-free surfaces, whereas below this time interval different or multiple superlattice structures were present, with no observable molecular order in the PFBT formed layer prior to 4 hour immersion times. Coverage dependence of work function has been observed for TP and 4-FTP within the first ~300 seconds of assembly time with stable values after this period.[13]

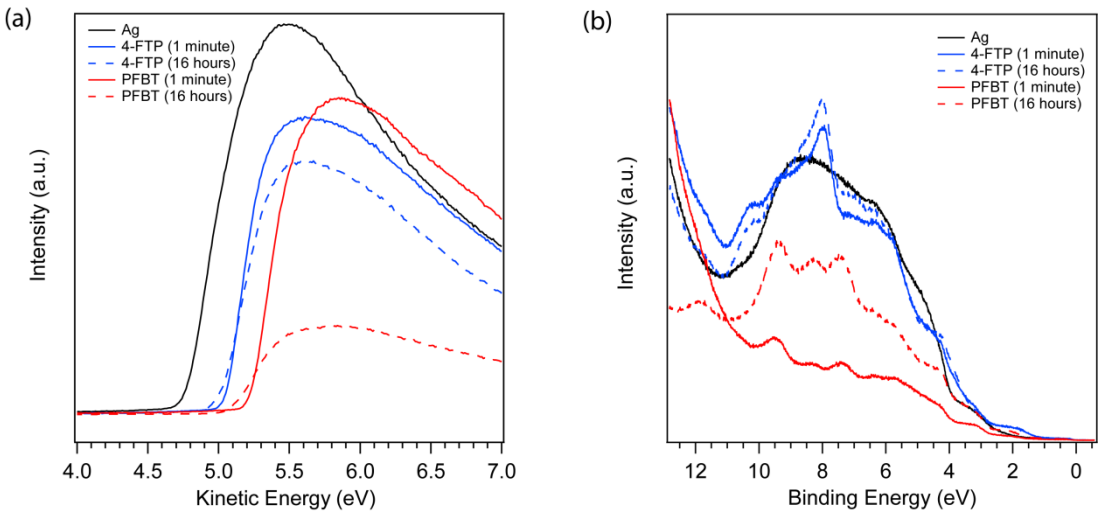

Figure 3.5: UPS spectra of PFBT and 4-FTP after immersion times of 1 minute and 16 hours, both referenced to polycrystalline Ag. (a) SECO region and (b) E_f edge.

The signal from the valence band states for PFBT after 16 hours displays an increased signal from the individual electronic excitations structures between 10 – 15 eV, which can be associated to an increase in the effective coverage of the adsorbate. Changes in the valence band onset for both 4-FTP and PFBT was not observed for

longer assembly times, although the signal from PFBT after 1 minute was

Table 3.2: Summary of work function values extracted from UPS and Kelvin probe with associated change in work function ($\Delta\Phi$). All Kelvin probe measurements were conducted after UPS measurements.

Sample	Φ_{UPS} (eV)	$\Delta\Phi_{UPS}$ (eV)	Φ_{KP} (eV)	$\Delta\Phi_{KP}$ (eV)
Ag	4.72	-	4.70	-
PFBT (1 minute)	5.20	0.48	5.37	0.67
PFBT (16 hours)	4.96	0.24	5.78	1.08
4-FTP (1 minute)	5.02	0.30	5.23	0.53
4-FTP (16 hours)	5.00	0.28	5.20	0.50

significantly weaker and made its assessment difficult. Variations in the valence band onset have been related to changes in geometric rearrangement and/or the bond-dipole, therefore it can be inferred that there is no significant influence from either of these effects.[10] Minimal variations in the UPS spectra for 4-FTP may indicate a lower degree of disorder in the layer or less surface reorganisation of the thiol compared to PFBT. It must be noted that both Ag reference samples for UPS and Kelvin probe measurements were rinsed with anhydrous IPA and blown dry with N_2 to match the process conditions for all other samples.

The change in work function over time for PFBT and 4-FTP was studied at specific intervals during the initial period of self-assembly. Noticeable increases in the work function for PFBT were observed within the first 1 hour of surface modification, however in contrast to this 4-FTP displayed minimal deviation in work function (see **Fig.3.6**). The drop in work function after the initial immersion for PFBT (reaching a minimum of 5.2 eV at 1 minute immersion) is likely to be due to minimal order to the orientation of the molecules given the low coverage, and hence no significant molecular dipole pointing away from the surface. Adsorption of

material to the sample surface will impact upon the intrinsic electron cloud spilling out of the surface, thus reducing the work function due to the pillow-effect. These

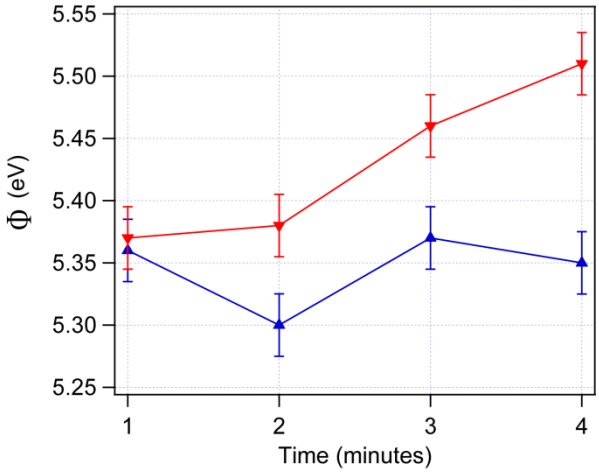

Figure 3.6: Variation in work function with increasing immersion time for 4-FTP (blue) and PFBT (red) measured by Kelvin Probe. Samples were rinsed with anhydrous IPA and dried by a stream of N_2.

results match closely with the trends observed by UPS although the decrease in the work function of PFBT after 16 hours detected by UPS can be associated with changes due to the surface reorganisation or increased uptake of contaminants to the surface.

A work function increase of 0.3 eV was measured for TP modified Ag surfaces which did not correlate with reports for this thiol on Ag, as a reduction in the work function is known to occur.[14] The increase may be coming from the bond-dipole of the sulphur as this thiol is known to orientate flat on the surface at the early stages of growth.[6,15] Increased assembly times may lead to a reduction in the work function as the contaminants from the Ag are removed and the influence from the sulphur becomes less prominent as the tilt angle of the thiol increases. Additionally,

different solvents were investigated for dissolving the organothiol such as ethanol, toluene, and acetone. IPA was chosen as the primary solvent choice due to its innocuous nature although no significant fluctuations in work function and static water contact angle were observed when preparing PFBT formulations with these solvents.

The final formation of the SAM is determined by the surface reconstruction and phase transition of the absorbate.[16] This transition period is known to change the work function and electronic structure of the thiol film, as at low coverage (i.e < 0.25 ML) a loosely packed film forms a recumbent or 'lying down', orientation, while at high coverage (~1 ML) a phase transition occurs where the film structure becomes densely packed with molecules adopting a supine or 'standing up' geometry.[13] This has been discussed by recent studies conducted with TP and 4-FTP on Cu(111).[17,18] The change in work function for PFBT measured in this work with longer assembly time could be attributed to the behaviour related to the phase transition from supine to an upright orientation. The molecular component of the overall surface work function can be approximated as having a contribution from the adsorbate metal bond (μ_{CHEM}), plus the dipole polarisation due to the molecular bond (μ_{SAM}).[13] At low coverage, if the molecule organises in a lying-down geometry, the associated dipole projection normal to the surface is small, leading to the adsorbate metal bond providing the dominant source of polarization (since no molecular component perpendicular to the surface exists). However, as the coverage increases, the adsorbate begins to assume a standing-up orientation, thus the molecular dipole contribution plays a more influential role on the work function. Studies described in literature have combined the molecular dipole with effects such as charge

redistribution, 'push-back' effects due to Pauli repulsion, and electrostatic interactions between dipoles.[19,20]

The work function change for PFBT appears to be more strongly related to the molecular density of the surface over time compared with 4-FTP. The packing density is known to vary between these SAMs as gas phase studies on Cu(100) surface show 4-FTP adopts a *c*(6 x 2) phase with two molecules per unit cell which is densely packed, and PFBT adopts a *p*(2 x 2) with one molecule per unit cell which is less densely packed.[4]

3.2.2 Energetic Arrangement at the Metal/Semiconductor Interface

Fig.3.7 show the change in work function of the TIPS:P4MS layer formed by spin-coating onto (a) 4-FTP and (b) PFBT modified Ag surfaces. Continual exposure of the sample to UV light with repeat scans showed a gradual increase in E_{SECO} which

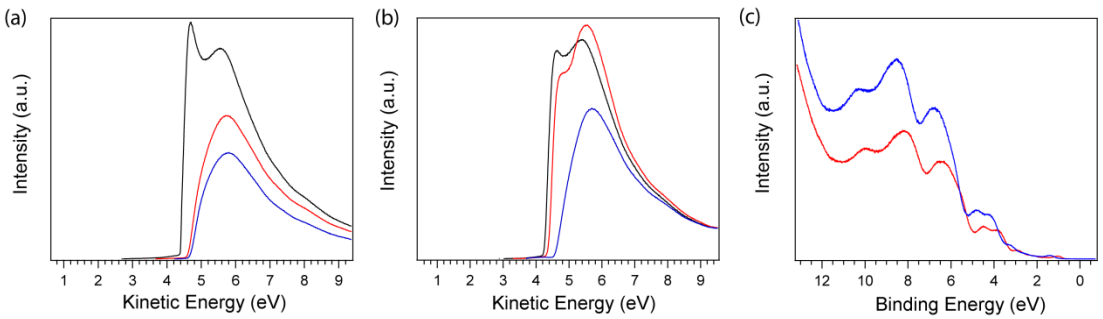

Figure 3.7: UPS spectra of TIPS/P4MS deposited on Ag electrodes modified by (a) 4-FTP (b) PFBT and (c) the HOMO onset formed on 4-FTP (red) and PFBT (blue). The spectra of (a) and (b) show the gradual shift in work function with repeat scans of the sample from the initial (black), secondary (red) and ternary (blue) scans.

may relate to damage to the organic semiconductor. **Fig.3.7(a)** display an increase in the E_{SECO} by 0.2 eV (from 4.4 to 4.6 eV) and **Fig.3.7(b)** an increase of 0.25 eV (from

4.25 to 4.5 eV). Each individual measurement was conducted on a different section of the sample. The HOMO onset did not shift with repeat scans for both samples, however, comparisons between 4-FTP and PFBT displayed an increase in the BE by 0.3 eV, respectively, as shown in **Fig.3.7(c)**. A HOMO onset of 0.7 eV and 1 eV was detected for 4-FTP and PFBT, respectively. Using the initial scan only, an IP of 5.1 eV and 5.15 eV was detected for TIPS/P4MS thin-films formed on 4-FTP and PFBT modified Ag surfaces, respectively. The relative HOMO position extracted from the UPS data matched closely with literature values for TIPS-pentacene.[14]

The energy level diagrams shown in **Fig.3.8** were constructed using the data from **Fig.3.5** for each thiol and **Fig.3.7** for the active layer blend. The main difference between the two systems is the interface dipole barrier (Δ) which for

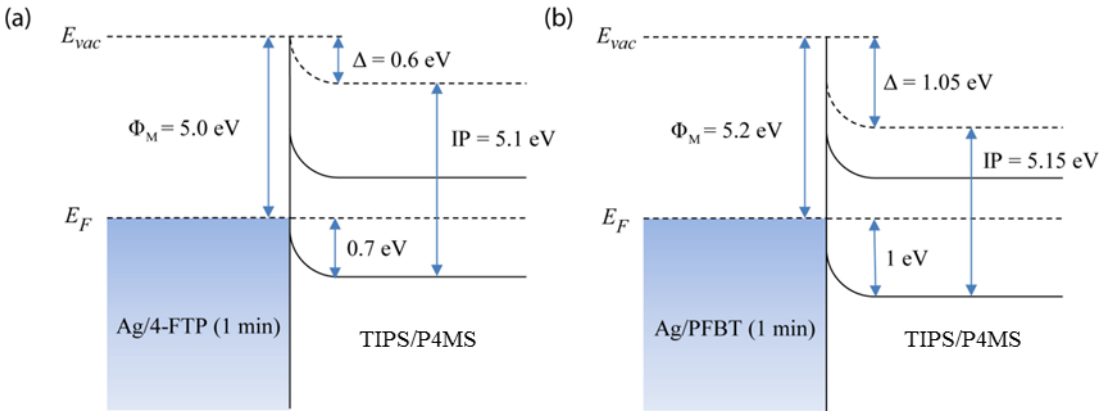

Figure 3.8: Energy level diagram of (a) Ag/4-FTP/TIPS-P4MS and (b) Ag/PFBT/TIPS-P4MS.

PFBT/TIPS-P4MS was 0.45 eV larger than 4-FTP/TIPS-P4MS. This large shift in the vacuum level relates to the same increase in the charge-barrier height which is related to contact resistance in OTFTs. The presence of this interface dipole barrier can be explained by the 'push-back' effect where the electron density extending from

the metal free surface into vacuum (which forms a dipole pointing at the metal bulk) has its surface dipole reduced by the deposition of molecules onto the surface. This results in a subsequent decrease in the work function of the metal. Although the E_{SECO} is shifted to higher binding energies with repeat scans (see **Fig.3.7**), this leads to a reduction in the measured Δ which would subsequently increase the IP due to no changes observed in the HOMO onset. Such effects could relate to beam damage, charging of the sample, rough or incomplete topography features exposing the underlying substrate, and errors from the data fitting process.

The discrepancy in work function between Kelvin probe and UPS can be associated to the reference sample used for each technique. Referencing of air-exposed Ag can vary between 4.2 to 4.8 eV which will directly contribute to the differences observed. Additionally, there is a fundamental difference in how the two techniques measure work function. The work function measured by UPS is a threshold value representing the lowest energy electrons able to escape the film surface upon excitation with UV light, therefore UPS represents the work function as the lowest value for a measured area.[22] Alternatively, Kelvin probe measures the average work function beneath the probe area.[22] Consequentially, if the surface is non-uniform, as would be the case for SAM treatments with 1 minute immersion times, the work function measured would be of higher value than that of UPS. Additionally, the vacuum conditions required for UPS measurements may reduce the quantity of volatile surface adsorbates on the films, resulting in a subsequent work function difference.

3.2.3 Surface Energy Study of Organothiols

The surface energy characteristics for a selected number of thiols shown in **Fig.3.2** were investigated to understand the potential wetting properties of the surface after SAM modification. Particular interest was given to 4-FTP and PFBT modified Ag surfaces for which results are tabulated in **Table 3.3** and **Table 3.4**, respectively. The modified surfaces were studied over a range of annealing temperatures to investigate changes in surface wetting conditions due to the application of thermal energy. SAM treatment was prepared using 1 minute immersion times with 10 mM concentrations. The results for 4-FTP functionalised surfaces displayed a decrease in the observed contact angle with diodomethane (MI) as the probing liquid with increasing temperature. A similar behavioural pattern was observed for PFBT modified Ag surfaces (see **Table 3.4**). In both circumstances the static-water contact angle did not deviate significantly under these process conditions. Similar observations have been reported by Ishida *et al.* where the MI values reduced considerably after prolonged annealing in air of terphenyl derivatised

Table 3.3: Surface energy results of 4-FTP modified Ag electrodes studied over a range of annealing temperatures.

Sample	Water (°)	MI (°)	γ_D(mN/m)	γ_P (mN/m)	IFT (mN/m)
Rinsed Only	82.2	40.0	37.0	3.3	40.3
110 °C	83.8	39.6	37.6	2.7	40.2
120 °C	83.7	39.4	37.6	2.7	40.3
130 °C	82.2	36.5	38.9	2.9	41.8
140 °C	87.4	35.5	40.5	1.4	41.8
150 °C	84.0	36.0	40.0	2.2	42.3
180 °C	81.8	32.2	41.0	2.7	43.7
200 °C	82.0	24.2	41.3	2.6	43.9

thiols on Au(111) surfaces up to temperatures of 180 ^{o}C.[15] Through annealing the electrode surface by incremental increases in temperature, the IFT and dispersive component (γ_D) increased. No discernible trend in the polar component (γ_P) was observed by this approach, but remained between 2 - 3 mN/m for most conditions concerning 4-FTP, and between 1 - 2 mN/m for PFBT. These results were highly reproducible for PFBT and 4-FTP modified Ag surfaces displaying similar trends throughout.

Table 3.4: Surface energy results of PFBT modified Ag electrodes studied over a range of annealing temperatures.

Sample	Water (°)	MI (°)	γ_D(mN/m)	γ_P (mN/m)	IFT (mN/m)
Rinsed Only	84.9	39.7	37.7	2.4	40.1
110 °C	85.0	40.3	37.4	2.4	39.8
120 °C	85.0	36.6	39.4	2.1	41.5
130 °C	85.0	34.7	40.4	1.9	42.3
140 °C	86.3	32.7	41.6	1.5	43.1
150 °C	85.0	31.2	42.1	1.7	43.8
180 °C	85.0	27.3	43.8	1.5	45.3
200 °C	82.0	23.9	44.6	2.1	46.7

Other organothiols were studied under similar conditions and their surface energies are tabulated in **Table 3.5**. These particular thiols did not display such a significant reduction in their respective MI values with increasing post-treatment annealing. A subtle reduction in the MI contact angle was apparent for TFTFMBT modified surfaces but were less significant in comparison. Changes in the static MI contact angle always enhanced with increased electronegativity of the SAM by which TP < 4-BTP < 4-FTP < PFBT < BTFMBT < TFTFMBT. It is commonly stated that the size of the static water contact angle is dependent on the functional group of the thiol, where increasing electronegative counterparts will result in

increased contact angles. The deionised water contact angle did increase largely for BTFMBT and TFTFMBT signifying the enhancing hydrophobicity of these surfaces, whereas all other thiols were between 80 – 90 degrees, therefore this trend was not observed, in particularly between TP, 4-BTP, 4-FTP and PFBT. Irregularity in the static water contact angle was observed for this particular investigation with significant variations measured between samples prepared on different days. This effect can result from changes in the atmospheric conditions of the laboratory which can result in subsequent fluctuations. Increases in humidity caused larger static water contact angles with results 3 - 4 degrees high than average, which directly impact the calculated polar and dispersive components. All contact angle measurements stated in this thesis are taken from repeat readings conducted on the same day to avoid any misrepresentation.

Table 3.5: Surface energy results for other investigated SAMs under selected annealing conditions.

Sample	Water (°)	MI (°)	γ_D(mN/m)	γ_P (mN/m)	IFT (mN/m)
TP (Rinsed)	81.9	9.3	48.6	1.6	50.2
TP (140 °C)	83.5	12.0	48.4	1.3	49.7
TP (180 °C)	85.4	10.1	49.5	0.8	50.1
4-BTP (Rinsed)	91.0	13.9	49.7	0.2	49.9
4-BTP (140 °C)	89.0	17.6	48.3	0.4	48.7
4-BTP (180 °C)	91.6	15.2	49.5	0.1	49.7
BTFMBT (Rinsed)	97.3	50.6	33.6	0.4	34.0
BTFMBT (140 °C)	88.8	48.6	33.2	2.1	35.3
BTFMBT (180 °C)	90.5	48.4	33.7	1.6	35.3
TFTFMBT (Rinsed)	101.1	55.8	31.0	0.2	31.2
TFTFMBT (140 °C)	95.1	53.1	31.6	0.9	32.5
TFTFMBT (180 °C)	97.3	48.3	35.1	0.3	35.4

A noticeable trend was the consistently larger polar constituent associated with 4-FTP modified Ag contacts compared with other thiols investigated in this study. This result is significant as the combination of a polar surface and an active layer blend consisting of a dispersive small molecule and a polar binder can aid phase separation between the two components. This result will be discussed in further detail in **Chapter 4** in relation to OTFT device performance.

Investigation into the surface energy conditions of the non-functionalised Ag surface are tabulated in **Table 3.6**. The surface energy conditions of the electrode surface change depending on if the surface has been rinsed with solvent or studied directly after thermal evaporation. These changes may relate to the uptake of atmospheric contaminants during and after the rinsing stage. This effect was also observed when measured on glass when treated in the same manner. Freshly cleaned glass substrates provided static-water contact angles of c.a. 8 degrees with values < 5 degrees after annealing. After rinsing of the glass surface with the surfactant solution or IPA led to increases in the contact angle. This will be discussed in detailed in **Chapter 4**.

Table 3.6: Surface energy calculations for Ag samples 'rinsed' with anhydrous IPA and 'Bare' samples measured immediately after evaporation.

Sample	Water (°)	MI (°)	γ_D(mN/m)	γ_P (mN/m)	IFT (mN/m)
Rinsed Only	88.0	25.1	42.2	1.1	43.3
140 °C	89.0	20.8	43.9	0.7	44.7
180 °C	83.5	21.6	45.5	2.0	44.5
Bare	90.8	8.1	50.8	0.1	50.9
Bare (140 °C)	83.8	11.5	48.6	1.2	49.8
Bare (180 °C)	90.0	15.5	49.1	0.3	49.4

It is assumed that the MI contact angle decreases due to molecular desorption after annealing at relatively high temperatures. Annealing above 200 ^{o}C for PFBT and 4-FTP produced contact angles which matched the reference sample when rinsed with anhydrous IPA (see **Table 3.6**) implying complete desorption. It may be inferred from these results that complete desorption of all thiols investigated does not occur until above 180 ^{o}C. Annealing temperatures above 120 ^{o}C to the point of complete desorption may result in oxidation of the sulphur head-group, partial desorption and reorganisation of the thiolates which could contribute to changes in the surface energy.

3.2.4 X-ray Photoemission Spectroscopy (XPS) of Thiol Modified Electrodes

The elemental and chemical composition of polycrystalline Ag and Au surfaces after thiol modification were investigated by XPS. These measurements were performed on PFBT and 4-FTP modified samples with designated immersion times of 1 minute and 16 hours. These two distinctly different preparation times were used to elucidate how the thiol interacts with the metal surface with time. The experimental and computational data of the atomic distribution at the surface of polycrystalline Ag for both 4-FTP and PFBT are discussed below (see **Fig.3.9**).

The S 2p spectra shown in **Fig.3.9** reveal three sulphur species which display $2p_{3/2,\ 1/2}$ doublets. A scheme is used to illustrate the three associated sulphur regions, which have been denoted alphabetically for each corresponding doublet (see **Fig.3.10**). The S 2p spectrum consists of a strongly attenuated doublet with the $2p_{3/2}$ peak at a binding energy (BE) of ≈162.5 eV (Peak B), a second doublet (Peak A) shifted to higher BE ($2p_{3/2}$ peak between 163 - 164 eV) and a third doublet (Peak C) which has the lowest intensity and is shifted to lower BE (S $2p_{3/2}$ peak at 161.0 eV).

The dominant sulphur species, Peak B, is associated with thiolates (Ag-S-R) in its bound state and its appearance has been linked with closely packed and well-ordered SAMs.[23] The S 2p sub-spectra of Peaks A and C are in close agreement with experimental and theoretical data for other thiolates on Ag, which can be ascribed to unbound and bound sulphur species, respectively.[24,25] The appearance of Peak C is commonly observed in SAMs with low surface coverage or disordered phases.[23]

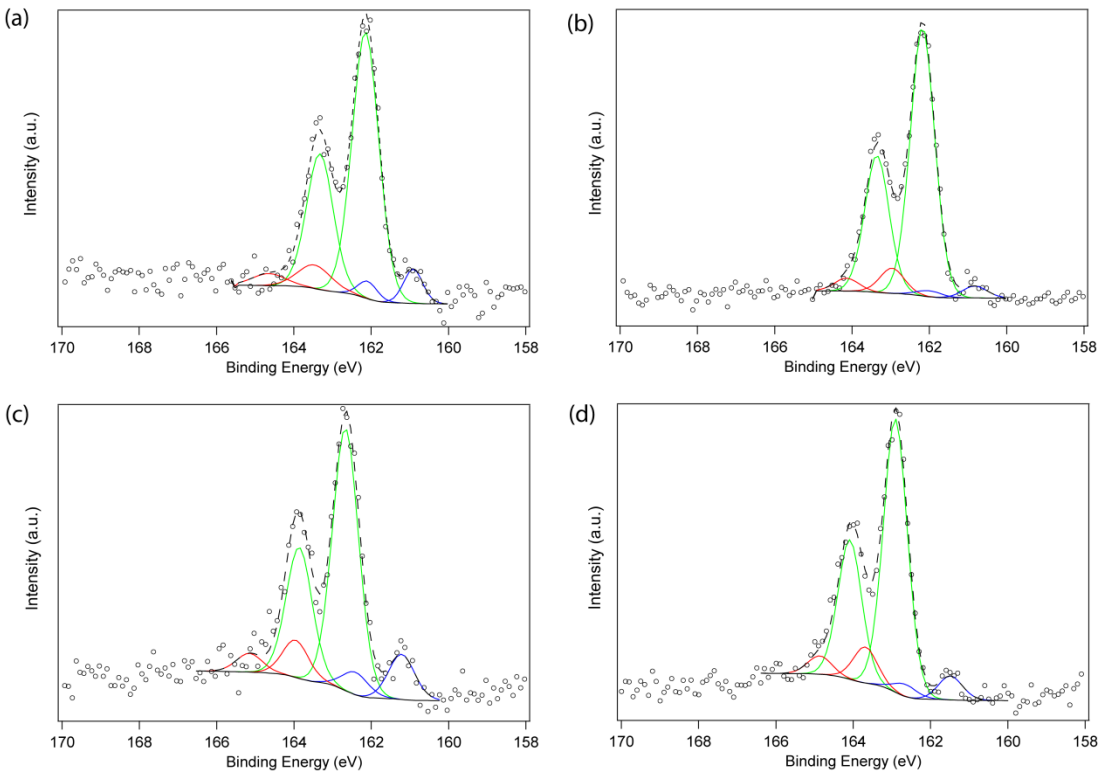

Figure 3.9: XPS spectra of the S 2p region for 4-FTP and PFBT on polycrystalline Ag after varied immersion times of (a, c) 1 minute, (b, d) 16 hours, respectively. The red, blue and green lines represent different sulphur species, the dashed black line shows the fitting envelope, the circles indicate the experimental data, and the continuous black line is the Shirley background.

The BE of the aromatic thiol bound to the Ag surface via the sulphur atom is expected to be lower than that of an unbound aromatic thiol, because the formation

of a covalent bond is accompanied with charge transfer from the Ag to the sulphur atom.[26] No evidence for disulphides, alkylsulfides or oxidative products (sulphinite/sulphonate) were found in these spectrums. Commonly, conjugated thiols are known to be reactive towards oxidation, therefore the results show good stability of the layer.[27] All data analysis assumed a spin-orbit splitting of 1.18 eV and an intensity ratio between ($2p_{3/2}$) and ($2p_{1/2}$) signals of 2:1.[28] These constraints are valid for atomic sulphur and represent good approximation for core levels of bound sulphur.[26] The same FWHM was applied for each sulphur species within their associated S 2p spectrum. Quantitative analysis of each spectra are tabulated in **Table 3.7**.

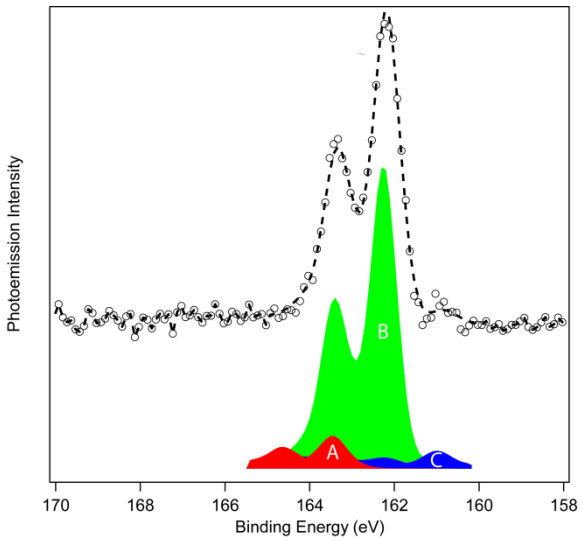

Figure 3.10: S 2p XPS spectrum of three sulphur species detected in this work together with the fit analysis underneath. The S 2p component of the unbound species (A) is shifted to higher binding energies compared to that of bound species (B). The low energy component (C) stems possibly from sulphur with higher coordination to Ag atoms, atomic sulphur, or another sulphur without C-S cleavage (e.g. molecular decomposition).

Table 3.7: Summary of binding energy values for S $2p_{3/2}$ species with associated relative coverage of each sulphur species for both PFBT and 4-FTP for 1 minute and16 hours immersion times.

Sample	$S2_{p3/2}$ (eV)	Area (%)	$S2_{p3/2}$ (eV)	Area (%)	$S2_{p3/2}$ (eV)	Area (%)	Ag : F_{1s}	F_{1s} (eV)	FWHM (eV)
	Peak A		**Peak B**		**Peak C**				
4-FTP (1 min)	163.5	2.9	162.2	89.2	160.9	7.9	16.0 : 1	687.2	0.81
4-FTP (16 hours)	163.0	8.2	162.2	87.9	160.8	3.9	11.1 : 1	687.2	0.74
PFBT (1 min)	164.0	10.9	162.7	76.0	161.2	13.1	4.0 : 1	688.0	0.79
PFBT (16 hours)	163.7	10.8	162.9	82.0	161.5	7.2	2.6 : 1	688.2	0.73

Fitting of Peak A for both 4-FTP (**Fig.3.9(a)**) and PFBT (**Fig.3.9(c)**) after 1 minute immersion proved problematic due to the applied modelling constraints. It is possible that a reduced spin-orbit splitting or removal of the FWHM constraint may accommodate a better fit for this sulphur species. The spectral fitting for 16 hour immersion for 4-FTP (**Fig.3.9(b)**) and PFBT (**Fig.3.9(d)**) displayed a shift to lower BE for Peak A. It is plausible that this associated unbound sulphur species may lead to a BE shift caused by a difference in interaction between the molecule and the metal surface, even in the case of physisorbed constituents.[29] The long reorganizational time associated with thiols on noble metal surfaces may be the contributing factor to this BE shift. It is possible that disulphides (R-S-S-R) may assemble on Ag where its photoemission would overlap with the S 2p contribution from the thiolate giving rise to inconsistencies in the $2p_{3/2}$ and $2p_{1/2}$ core level intensity ratios.[30] This appears plausible in the XPS spectra for 1 minute immersion times as deconvolution of the S 2p spectra shows inexact spin-orbit splitting (≠2:1)

ratios suggesting that disulphide species may be present. This outcome may not come as a surprise, as the GCMS results (discussed in section 3.4) show a high percentage of dimers within the surfactant solution for both PFBT and 4-FTP formulations. Peak A is commonly assigned to an unbound –SH group but has also been associated with degradation of sulphur by X-ray exposure.

The relative ratios of Ag : F for PFBT were extracted as 4.0 : 1 and 2.6 : 1 for 1 minute and 16 hours, respectively, relating to a 61% increase. Studying the same relative ratios for 4-FTP displayed a similar change in its stoichiometry, leading to increases in the presence of fluorine measured as 16.0 : 1 and 11.1 : 1 for 1 minute and 16 hours, respectively, relating to a 59% increase. The trend clearly shows that the longer the immersion time, the higher the fluorine signal. The XPS confirms immediate adsorption of the thiolate to the Ag surface, followed by a decrease in adsorption rate as the availability of binding sites decreases, which follows the Langmuirian adsorption model.[10] The BE peak positions for F1s of PFBT is shifted by c.a. 1 eV relative to 4-FTP due to its increased electronegativity.

The F/C ratio can aid in estimating the film quality of the layer, as since each molecule has six carbon atoms per one fluorine atom for 4-FTP, and five fluorine atoms for PFBT, a stoichiometry of F/C ~ 0.16 and ~ 0.83 for 4-FTP and PFBT, respectively, can help assess the purity of the formed layer. The F/C for 4-FTP are 0.05 (1 minute) and 0.11 (16 hours), and for PFBT are 0.34 (1 minute) and 0.61 (16 hours).

An expected trend is observed from modelling of the sulphur region, where increased atomic percentage in S 2p indicates a higher surface composition of sulphur associated with longer assembly time. The higher intensity (i.e. percentage area) of Peak B associated with 4-FTP may be related to the formation of closely

packed and ordered surface as confirmed by STM for this thiol when compared with PFBT.[17] Research by Wong *et al.* has shown STM studies of 4-FTP which display regular arrays from low coverage surfaces at 80 K, as well as for bromo- and chloro-para-substituted TP molecules on Cu(111).[17] In the case of TP and PFBT surfaces, the molecular surface ordering was irregular at low coverage which increased in uniformity at higher coverage. The larger FWHM of the S $2p_{3/2,1/2}$ at short immersion times (i.e. 1 minute) can be attributed to the inhomogeneity of the surface. Studying the relative intensities for the bound sulphur species (Peak B/Peak C), this indicates an increase of 66% for both PFBT and 4-FTP from 1 minute to 16 hours displaying similar growth kinetics. It appears that much lower amounts of the sulphur species assigned to Peak C are observed over longer assembly times. It is possible that excessive immersion times (e.g. > 16 hours) may completely remove this species or leave trace amounts within the SAM layer.

PFBT and 4-FTP were investigated for their thermal stability by annealing under ambient conditions. The spectra for heat treatment at 140 °C are shown in **Fig.3.11** with tabulated data in **Table 3.8**. The annealed samples were treated for 1 minute under ambient conditions and stored under nitrogen until transferred to the analysis chamber. In the case of annealing 4-FTP, the disappearance of the unbound sulphur state (Peak C) occurs and the appearance of oxidative sulphur states (sulphinite/sulphonate species) is observed between 166 – 170 eV, which is strongly related to the annealing process. This correlates with the presence of a clear oxygen (1s) emission at 532.5 eV. The oxidised sulphur component constitutes 19% of the detected sulphur species. The appearance of oxidation is likely to disrupt the molecular ordering and alter the chemical and electrical properties of the thiolates. Annealing of PFBT (see **Fig.3.11(a)**) did not display any oxidation but a significant

increase in Peak C was observed alongside a drop in Peak B. This indicates increased disorder in the layer with larger amounts of atomic sulphur present. The adsorption rate did not increase with temperature but proved to hinder the formation of the layer.

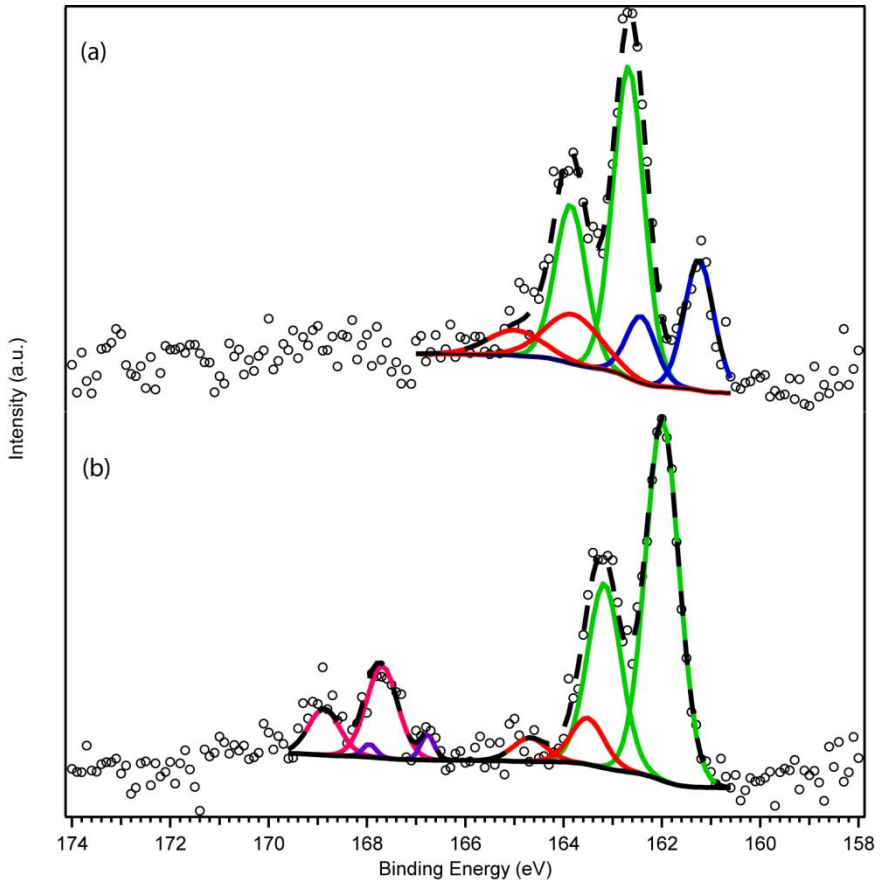

Figure 3.11: XPS spectra of the S2p region for (a) PFBT and (b) 4-FTP annealed at 140°C on polycrystalline Ag. Theses spectra are normalised to allow a better comparison between different systems.

The S 2p spectra of all films in **Fig.3.9** suggest the presence of an additional sulphur species (Peak C). This signal was not detected for both 4-FTP annealed at 140 °C after 1 minute immersion (see **Fig.3.11(b)**) and additional PFBT samples after 16 hours immersion which were measured on different samples. This particular

sulphur species has a low spectral weight (~10%) which decreases with longer immersion time. This feature can be ascribed to atomic sulphur or a thiolate-type bound sulphur with a different binding chemistry and/or geometry as compared to Peak B.[31] The doublet at ~161.0 eV has been discussed in literature as to appear only at the early stage of the molecular assembly. This may be coherent with these results, with removal occurring after annealing or excessive assembly times.[32] The effects of annealing in vacuum and air at high temperatures has also lead to its appearance. Cleavage of the C-S bond by annealing (at 415-490K) of alkanethiolate

Table 3.8: Summary of binding energy values of S $2p_{3/2}$ species with determined relative rations for both PFBT and 4-FTP after annealing at 140 °C in air.

Sample	$S2_{p3/2}$ (eV)	Area (%)	$S2_{p3/2}$ (eV)	Area (%)	$S2_{p3/2}$ (eV)	Area (%)	$S2_{p3/2}$ (eV)	Area (%)	Ag : F_{1s}	F_{1s} (eV)
	Peak A		Peak B		Peak C		Oxidised			
4-FTP (1 min)	163.5	9.2	162.0	71.7	-	-	166-169	19.1	16.8 : 1	687.1
PFBT (1 min)	163.8	16.8	162.7	59.6	161.3	23.6	-	-	3.1 : 1	688.1

SAMs on Au has shown a shift of the thiolate-related doublet to ≈161.0 eV.[14] This particular peak has been associated with decomposition of the thiol on Au surfaces.[32] An XPS reference scan of unmodified Ag detected the presence of common atmospheric contaminants from mainly carbon and oxygen (see **Fig.3.12**). Surprisingly, previously conducted XPS experiments of unmodified Ag detected the existence of atmospheric sulphur, with a dominant doublet component at peaks at 161.2/162.4 eV, shown in **Fig.3.12(a)**. The presence of fluorine was not detected on this sample, eliminating the possibility of cross contamination by the fluorinated thiol, therefore we associate this with atmospheric sulphur. More sulphur species

exist on the Ag surface due to the shoulder of the S $2p_{1/2}$ at higher binding energy. Due to modelling constraints associated with sulphur, defining this sulphur species at higher binding energy proved troublesome, but we expect the doublet to be positioned close to 162.2/163.4 eV. Repeat measurements of freshly prepared Ag did not detect the presence of sulphur, therefore all measurements were conducted utilising these samples. Adventitious carbon and oxygen species were detected on all reference polycrystalline Ag surfaces. Species related to contamination are gradually removed from the surface by thiol modification of the surface, observed by the reduction in the C1s associated with adventitious carbon and reduction in oxygen signal. There is also a possible overlap at these binding energies with Peak C with atmospheric sulphur as mentioned.

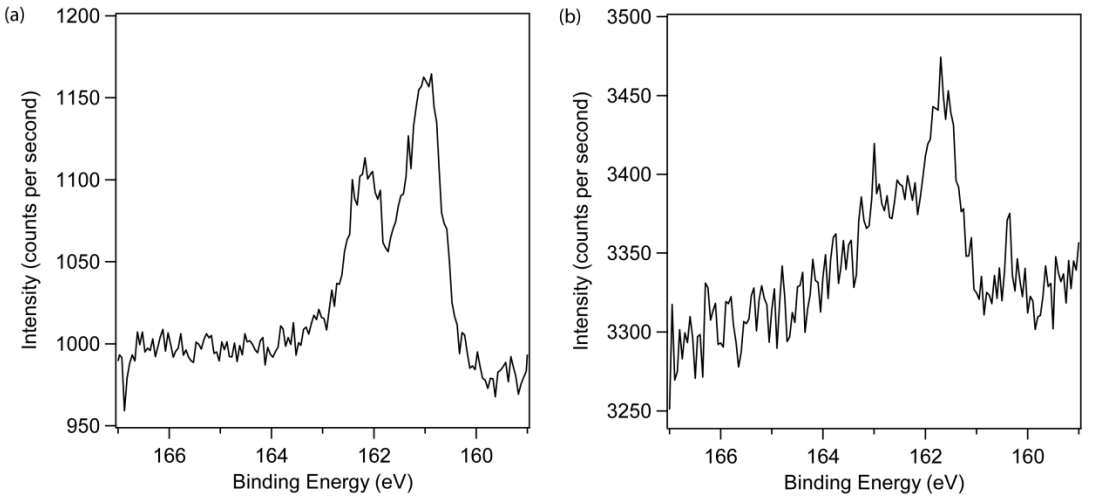

Figure 3.12: XPS spectra of the S 2p region of unmodified polycrystalline (a) Ag and (b) Au.

The peak positions for PFBT and 4-FTP on Au are tabulated in **Table 3.9**. The peak assignments for PFBT are in close agreement with work published on Au(111).[11] The major doublet is c.a. 0.8 eV higher compared to other literature

values.[11] This may be related to the experiment being conducted on polycrystalline Au surface and not Au(111). Again, the appearance of atmospheric sulphur was detected on the surface, shown in **Fig.3.12(b)**. As a relatively inert metal towards chemisorption (oxygen, carbon monoxide, water, and hydrocarbons) at 300 K, Au

Table 3.9: Peak assignment for 4-FTP and PFBT on polycrystalline Au substrates.

Sample	$S2_{p3/2}$ (eV)	$S2_{p3/2}$ (eV)	$S2_{p3/2}$ (eV)	F_{1s} (eV)
Au (bare)	160.4	161.8	-	-
4-FTP (1 min)	161.8	162.6	-	687.1
4-FTP (16 hours)	161.8	162.5	-	687.0
PFBT (1 min)	161.9	162.8	164.3	687.7
PFBT (16 hours)	161.9	162.7	-	687.8

doesn't form a stable oxide under ambient conditions and is reported to be resistant towards atmospheric contamination.[28,30] However, we found exposure of the sputtered polycrystalline Au surfaces resulted in emission from carbon (1s) at c.a. 284 eV, a broad asymmetric oxygen (1s) peak at 532-533 eV, and the presence of sulphur (2p) as a doublet at 160.4/161.8 eV. XPS analysis has elucidated the extent of substrate contamination prior to self-assembly and the amount of oxygen, and excess carbon and sulphur with the PFBT and 4-FTP layers. The carbon detected on the surface is composed of hydrocarbons and oxidised organic species from the atmosphere, present within the solvent, and apparatus which comes into contact with the sample.

The XPS results clarify that the aromatic thiols interact with the surface and other adsorbates, either with (bound) or without (unbound) loss of the hydrogen at

the head group, forming a SAM with a composition comprising of intact thiols and thiolates.

3.2.5 Detection of Sulphides Present in Surfactant Solution

The thiol-thiol interaction within the surfactant solution was shown to lead to the formations of disulphides. The occurrence of dimers are also known to occur within the monolayer which can lead to the partial desorption of the thiolates as disulphides. The formation of disulphides (R-S-S-R) was investigated in this thesis by Gas Chromatography-Mass Spectroscopy (GC-MS). The formation of dimers was investigated by the variation in molar concentration between 10 mM and 1 mM stock solutions, and the impact of solution degradation between fresh and 6 month old formulations.

The mass spectrums in **Fig.3.13** are of 4-FTP solutions with molar concentrations of (a) 10 mM and (b) 1 mM, with the latter diluted from the stock solution of the former. Both solutions were prepared using 4-FTP mixed with

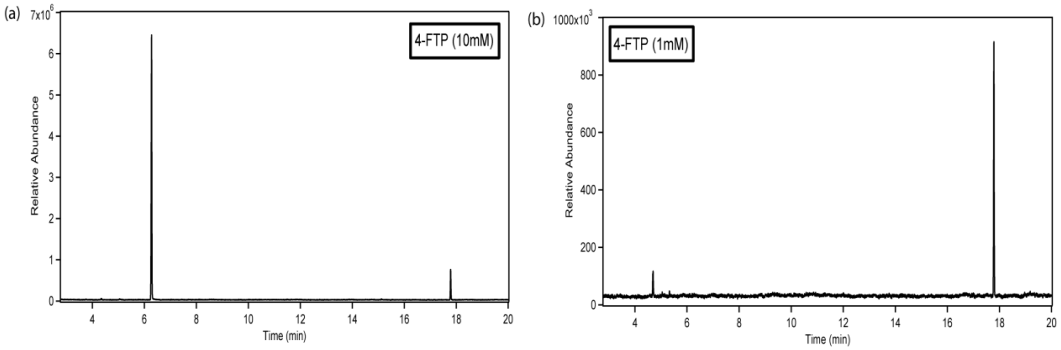

Figure 3.13: Mass spectra of 4-FTP prepared at concentrations of (a) 10 mM and (b) 1 mM.

anhydrous IPA. The peak at ca. 6 minutes in **Fig.3.13(a)** is associated with the monomer where the peak at ca. 18 minutes is related to the dimer. Through dilution of the surfactant solution an expected drop in the relative abundance is seen, decreasing from 10^6 to 10^3, but a significant reduction in the presence of the monomer, being almost undetectable in **Fig.3.13(b)**, occurs with only a small decrease in the amount of dimers present in the solution after dilution. Similar behaviour in terms of a reduction in the amount of monomer present after dilution were seen for all other thiols investigated (i.e. 4-BTP; TP; PFBT; BTFMBT). Dilution of the surfactant solution to 0.1 mM caused the previously discernable peaks to be lost in the noise although a small dimer associated signal could be determined.

The impact of time on the stability of the surfactant solution was also investigated. The surfactant solution was prepared in a sure-seal bottle of Anhydrous IPA and the concentrated thiol purchased from Sigma Aldrich after opening was no older than 4 weeks and stored in a fridge. Extraction of the solution was prepared by insertion of a nitrogen filled balloon to ensure that the bottle remained purged and to avoid any unwanted influences from oxygen. The stock solution used in **Fig.3.13(a)** was investigated after 6 months and the results are shown in **Fig.3.14**. This measurement showed that the stock solution had formed a significant amount of dimers outweighing the presence of the original monomer. Again, similar behaviour was seen for all other thiols previously mentioned.

The effect of heat on the properties of the surfactant solution was also investigated. The solution was extracted from the stock solution and heated within an open vial on a hot-plate under ambient conditions. This was investigated due to improvements in OTFT performance which will be discussed in **Chapter 4**. A range

of temperatures between 80 °C and 140 °C were studied. No apparent changes in the monomer or dimer signals were seen by annealing the solution.

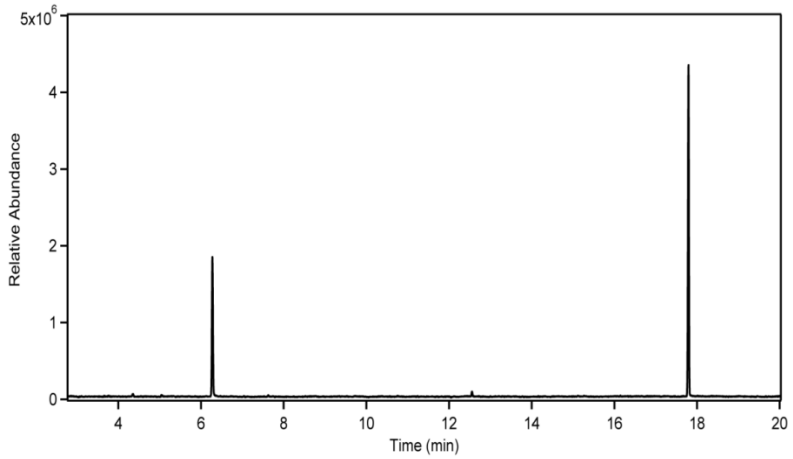

Figure 3.14: Mass spectrum of the stock solution (10 mM) of 4-FTP after 6 months.

The presence of dimers in the surfactant stock solution was investigated further in which to study the existence of dimers on the electrode surface. Raman spectroscopy using Ag SERS substrates was undertaken to investigate changes in the vibrational states associated with the sulphur group between the diluted 1 mM and freshly prepared 10 mM solutions. A comparative study between the two solution concentrations showed no comparable differences. Additionally, preparation of fresh 4-FTP and bis(trifluorophenyl) disulphide 10 mM solutions showed no differences in their corresponding spectrums.

3.3 Raman Spectroscopy Study of PFBT and 4-FTP Modified Ag Surfaces

Raman spectroscopy is a surface sensitive technique for verifying the presence of thiol-metal bonding, as well as deducing molecular orientation of adsorbed molecules on metallic surfaces. This technique is highly qualitative due to the sensitivity of the wavelength of light when interacting with organic materials, but

the SERS signal depends on both the analyte amount and the localised plasmonic resonance.

The Raman spectra of TP, 4-FTP, and PFBT formed on polycrystalline Ag SERS substrates were studied between 300 and 3200 cm^{-1}. The relative intensities and peak assignments discussed herein are taken from literature. Shifts associated with most modes from the neat spectrum of the associated thiol are due to changes in the electron density caused by bonding of the thiol with the metal surface. Changes in intensity between the free thiol (with the S-H bond present) and the thiolate (removal of hydrogen from the sulphur atom) can be related to the greater degree of freedom associated with the thiolate. Due to the thiol being partially negatively charged (i.e. slightly polar) when chemisorbed to the Ag surface ($RS^{-\delta}Ag^{+\delta}$) shifts to lower frequencies can occur due to the presence of this negative charge. The simplest aromatic thiolate, TP, has been extensively studied in literature [33-35] and was used as a comparative study to 4-FTP and PFBT. Work conducted by Abduaini *et al*. regarding molecular orientation of TP from aqueous solutions displayed temperature related changes in orientation once chemisorbed to polycrystalline Au surfaces.[36] The phenyl ring stands perpendicular to the substrate plane at room temperature, where upon heating the phenyl ring becomes tilted in the layer.[36] Within this work, Raman spectroscopy was adopted to investigate the thermal stability of the thiol over a range of annealing temperatures and to study characteristic peaks associated with its bonding to the metal surface.

The Raman spectra for TP after different post-treatment steps are shown in **Fig.3.15**. The results for TP from an aqueous solution are in agreement with other work conducted on Ag.[37,38] No significant variation in each respective spectra is observed when annealing up to 140 °C. A gradual reduction in the peak at ca. 3100

cm^{-1} was observed with increased post treatment annealing. The peak centred at 1000 cm^{-1} and the peaks at 1576 and 1589 cm^{-1} (commonly observed as a single peak in literature at 1580 cm^{-1}) are due to the benzene ring vibration, whereas the peaks at 1023 and 1080 cm^{-1} are characteristic of the benzenethiol group, $C_6H_5S^-$.[39,40] The peak at 1080 cm^{-1} presented the strongest signal from this investigation but was dramatically reduced after annealing at 180 °C and above, with a small residual signal remaining from other characteristic peaks. The ring-stretching vibration at 1580 cm^{-1} was still present at 180 °C although the vibrational peaks at 1023 and

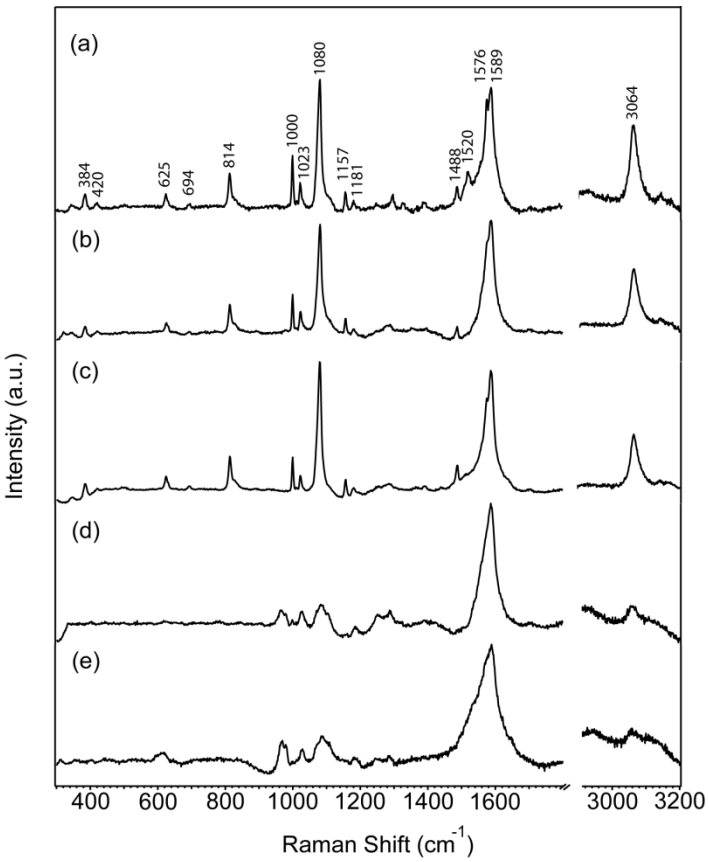

Figure 3.15: Principal Raman spectra of TP at (a) RT (not annealed); (b) 100 °C; (c) 140 °C; (d) 180 °C; and (e) 220 °C.

1080 cm^{-1} were significantly reduced and broadened in the SERS spectra at 180 °C

and 200 °C, indicating possible desorption or decomposition of the thiol. The strong signal of the υ1 primary ring mode at 1080 cm^{-1} and the ν(C=C) band split at 1576 and 1589 cm^{-1} was greater than any other modes, indicating a more upright orientation.[6,41,42] This is also supported by the strong in-plane (ip) modes (1000, 1023, 1072, 1573 cm^{-1}) relative to the weak/non-existent 468 and 735 cm^{-1} out-of-plane (oop) modes when compared to the neat spectrum of TP.

The Raman spectra of 4-FTP measured over a range of annealing temperatures are shown in **Fig.3.16**. The thiol was observed on the surface at 180 °C although the signal intensity was significantly reduced and displayed a large amount of noise in the response. No discernible features were detected at 220 ^{o}C displaying strong signal-to-noise in the spectra. There appeared to be little change in the intensity of the peak between 2900 and 3100 cm^{-1} with increased temperatures.

The 4-FTP spectra matches closely with work from literature on Ag with dominant peak matching at 624, 817, 1076, 1157, 1488 cm^{-1} (detected at 1491 cm^{-1} in literature), and 1589 cm^{-1} (detected at 1592 cm^{-1} in literature).[40,43] Blue shifts in the spectra were observed at 1488 and 1588 cm^{-1} by 1 and 2 cm^{-1} respectively after annealing, with a red shift at 1160 cm^{-1} by 2 cm^{-1}. The presence of the peak at 1000 cm^{-1} for TP is not observed for 4-FTP, but both thiols share a peak at 1076 cm^{-1} which represents a stretching mode of the aromatic ring.[44] The peak at 1076 cm^{-1} has its intensity enhanced with increased annealing when measured between RT and 140 °C relative to the peak at 1589 cm^{-1}. Para-substituents of TP have been shown to change its molecular packing due to differences in interactions between the functional terminal group of the thiol.[45-47] Work conducted by Khodabakhsh *et al*. has suggested a bond angle of 97.20° (H-S-C) for 4-FTP with this organothiol standing upright on Au surfaces.[48]

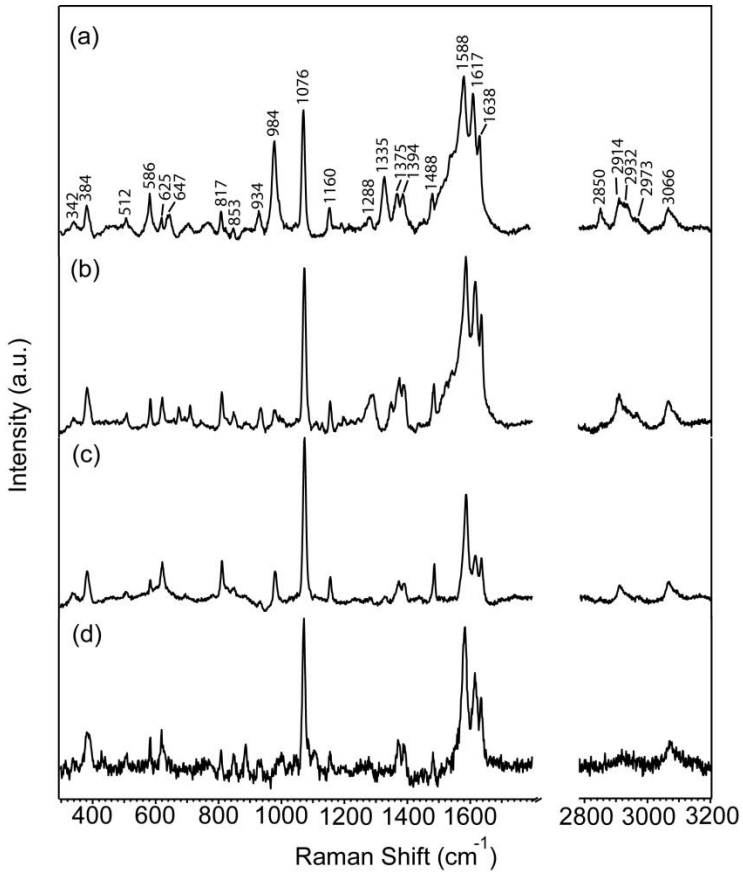

Figure 3.16: Raman spectra of 4-FTP at (a) RT (not annealed); (b) 100 °C; (c) 140 °C; and (d) 180 °C.

The Raman spectra for PFBT over a range of annealing temperatures are shown in **Fig.3.17**. A strong signal was detected at 180 °C in comparison to TP and 4-TTP signals at this temperature. Again, no signal was detected after annealing 220 °C. The signal at 2900 cm^{-1} is gradually diminished after annealing at higher temperatures. The peaks at 586 (υ_8, $\delta(C\text{-}C\text{-}C)_{ip}$), 859 ($\upsilon_7$, $\upsilon(C_6F_5\text{-}S)$), and 1287 cm^{-1} (υ_5, $\upsilon(C\text{-}F)$) are blue-shifted (i.e. upshifted) by 1, 2, and 4 cm^{-1}after annealing at 140 °C.[6] It is common to associate downshifts of ring modes as evidence that the aromatic ring lies flat on the surface, although this is known to neglect the effect that bonding to the metal through the sulphur can have on the ring mode vibrational

frequencies.[40] It is probable that oxidation of the sulphur may have occurred (although this wasn't detected by our XPS measurement) which will influence the vibrational modes of the thiol. Changes in *ip* and *oop* modes relative intensities were

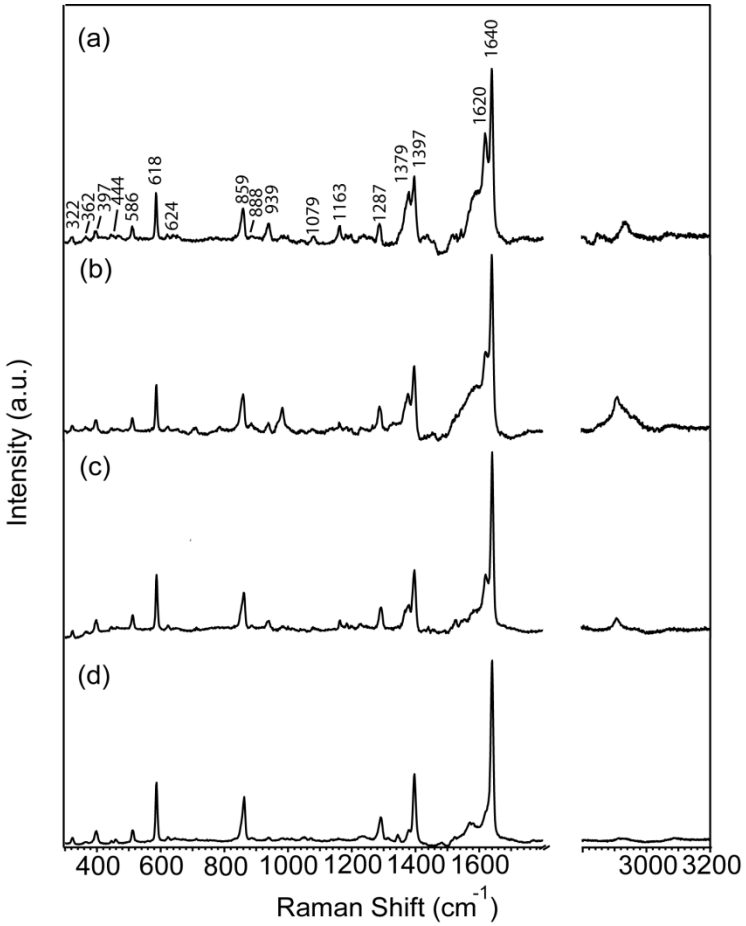

Figure 3.17: Raman spectra of PFBT at (a) RT (not annealed); (b) 100 °C; (c) 140 °C; and (d) 180 °C.

observed for annealing PFBT samples. Relative changes in the peaks at 939 cm^{-1} (which has been tentatively assigned to the δ(C-S-surface)$_{ip}$ mode) and 859 cm^{-1} (assigned to the $\upsilon(C_6F_5\text{-}S)$) may indicate alterations in the molecular orientation of the thiol. An increase in the 859 cm^{-1} signal after annealing at 180 °C lead to a decrease in the 939 cm^{-1} peak when compared against a rinsed PFBT modified Ag

surface, as shown in **Fig.3.18**. All shifts in modes reported here are likely to be result of changes in polarizability and electron density of PFBT molecule bound to Ag and may infer changes in the orientation of the thiol.

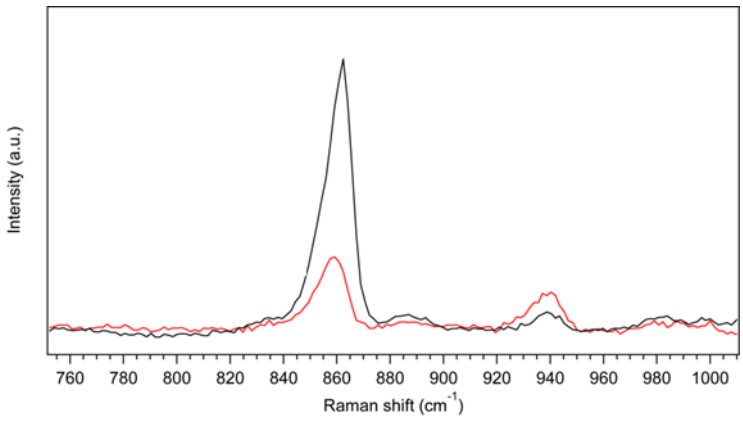

Figure 3.18: Variation in peaks at 859 cm^{-1} and 939 cm^{-1} after rinsing (red line) and annealing at 180 °C (black line).

The presence of water, atmospheric contaminants and residual solvent on the surface, with addition to the formation of multilayers are likely to influence the average molecular orientation of the adsorbate. The detection of solvent (i.e. toluene) on PFBT modified Ag SERS substrates has been observed by Mosier-Boss *et al* although the limit of detection for chloroform was discussed as being much higher due to it being a poor Raman scatterer.[49] It is unclear if residual IPA exists on the surface of the samples investigated. There is evidence for the presence of IPA in TP (**Fig.3.15**) and 4-FTP (**Fig.3.16**) results due to the appearance of the peak at 814 and 817 cm^{-1}, respectively. These peaks match closely with the very strong signal for IPA at 817 cm^{-1} discussed by Green *et al*.[50] These peaks are unassigned frequencies for TP and 4-FTP which were not detected in other literature studies. Both peaks are still present in their respective films when annealed at 100 °C and 140 °C, therefore

it would be surprising to detect IPA on the surface after such high temperature treatments due to its boiling point at 82.5 °C. The influence of the solvent on adsorption has been questioned in literature, where the solvent may be incorporated into the adsorbed monolayer (e.g. interpenetration when geometrical matching between solvent and the adsorbate is present, such as, long hydrocarbon chains and hexadecane),[51] and interactions between head group of adsorbate and solvent (e.g. hydrogen bonding). The nature of the solvent is known to influence the structure and properties of pure monolayers adsorbed from solution.[52]

3.3 Conclusion

Self-assembly of halogenated organothiols on Ag is an effective method for modifying the metals work function and surface energy properties. Reduction of the injection barrier by tuning the Ag electrodes work function to match the HOMO level of the OSC, alongside changing the hydrophobicity of the surface to influence preferential molecular growth of active layer, are the two major benefits of using SAMs. We have shown systematic variations in the both the work function and surface energy using a varied range of aromatic halogenated thiols, which can be beneficial to OSC materials with varied ionisation potentials.

Annealing of PFBT and 4-FTP functionalised Ag surfaces present resistance against desorption at post-treatment temperatures of 180 °C, as studied by Raman spectroscopy. Changes in surface energy were observed with annealing above 100 °C with the surface becoming more dispersive, resulting in increased IFT. Additionally, XPS showed oxidation of 4-FTP when studied after annealing at 140 °C, which signifies degradation of the thiol at this temperature, although no such effects were observed for PFBT.

The effect of SAM treatment on OTFT performance characteristics will be discussed in **Chapter 4** for all organothiols mentioned previously, with particular focus on PFBT and 4-FTP. The thermal stability of the SAM and subsequent changes in the chemical and electrical properties after annealing will used to understand the associated device performance. Herein, a 1 minute immersion time is deemed sufficient for self-assembly and will be adopted for the fabrication of all OTFTs unless otherwise stated. Additionally, the use of freshly prepared surfactant solutions will be implemented to reduce the presence of dimers, as shown by mass spectroscopy results.

3.4 References

[1] K. A. Singh, T. L. Nelson, J. A. Belot, T. M. Young, N. R. Dhumal, T. Kowalewski, R. D. McCullough, P. Nachimuthu, S. Thevuthasan, L. M. Porter. *ACS Appl. Mater. Interfaces*, (2011) **3**, 2973.

[2] M. Kitamura, Y. Kuzumoto, S. Aomori, M. Kamura, J. H. Na, Y. Arakawa, *Appl. Phys. Lett.*, (2009) **94**, 083310.

[3] S. D. Evans, E. Urankar, A. Ulman, N. Ferris, *J. Am. Chem. Soc.*, (1991) **113**, 4121.

[4] C. Schmidt, A. Witt, G. Witte, J. Phys. Chem. A, (2011) **115**, 7234.

[5] M. Bruening, E. Moons, D. Yaron-Marcovich, D. Cahen, J. Libman, A. Shanzer, *J. Am. Chem. Soc.*, (1994) **116**, 2972.

[6] M. C. Schalnat, J. E. Pemberton, Langmuir, (2010) **26**, 11862.

[7] H. A. Engelhardt, D. Menzel, *Surf. Sci.*, (1976) **57**, 591.

[8] Gaussian 98 Software, Gaussian Inc, Carnegie Office Park, Building 6, Pittsburgh, PA, 15106, USA.

[9] A. D. Becke, *J. Chem. Phys.* (1993) **98**, 5648.

[10] S. A. Panjagua, E. L. Li, S. R. Marder, *Phys. Chem. Chem. Phys.*, (2014) **16**, 2874.

[11] H. Kang, N.-S. Lee, E. Ito, M. Hara, J. Noh, *Langmuir*, (2010) **26**, 2983.

[12] W. Azzam, A. Bashir, P. Ulrich Biedermann, M. Rohwerder, *Langmuir*, (2012) **28**, 10192.

[13] S.-Y. Hong, P.-C. Yeh, J. I. Dadap, R. M. Osgood, *ACS Nano.*, (2012) **6**, 10622.

[14] J.-P. Hong, A.-Y. Park, S. Lee, J. Kang, N. Shin, D. Y. Yoon, *Appl. Phys. Lett.*, (2008) **92**, 143311.

[15] T. Ishida, H. Fukushima, W. Mizutani, S. Miyashita, H. Ogiso, K. Ozaki, H. Tokumoto, *Langmuir*, (2002) **18**, 83.

[16] G. E. Poirier, E. D. Pylant, *Science*, (1996) **272**, 1145.

[17] K. L. Wong, X. Lin, K. Y. Kwon, G. Pawin, B. V. Rao, A. Liu, L. Bartels, S. Stolbov, T. S. Rahman, *Langmuir*, (2004) **20**, 10928.
[18] P. A. Agron, T. A. Carlson, *J. Vac. Sci. Tech.*, (1982) **20**, 815.
[19] D. M. Alloway, M. Hofmann, D. L. Smith, N. E. Gruhn, A. L. Graham, R. Colorado, V. H. Wysocki, T. R. Lee, P. A. Lee, N. R. Armstrong, *J. Phys. Chem. B.*, (2003) **107**, 11690.
[20] H. Li, Y. Duan, P. Paramonov, V. Coropceanu, J.-L. Brédas, *J. Electron. Spectrosc. Relat. Phenom.*, (2009) **174**, 70.
[21] C. Schmidt, A. Wit, G. Witte, *J. Phys. Chem. A.*, (2011) **115**, 7234.
[22] R. J. Davis, M. T. Lloyd, S. R. Ferreira, M. J. Bruzek, S. E. Watkins, L. Lindell, P. Sehati, M. Fahlman, J. E. Anthony, J. W. P. Hsu, *J. Mater. Chem.*, (2011) **21**, 1721.
[23] S.-Y. Lee, Y. Choi, E. Ito, M. Hara, H. Lee, J. Noh, *Phys. Chem. Chem. Phys.*, (2013) **15**, 3609.
[24] D. G. Castner, K. Hinds, D. W. Grainger, *Langmuir*, (1996) **12**, 5083.
[25] A. Shaporenko, A. Terfort, M. Grunze, M. Zharnikov. *J. Electron. Spectrosc. Relat. Phenom.*, (2006) **151**, 45.
[26] K. Kummer, D. V. Vyalikh, G. Gavrila, A. Kade, M. Weigel-Jech, M. Mertig, S. L. Molodstov. *J. Electron. Spectrosc. Relat. Phenom.*, (2008) **163**, 59.
[27] J. M. Tiur, L. Jones II, D. L. Pearson, J. J. S. Lamba, T. P. Burgin, G. M. Whitesides, D. L. Allara, A. N. Parikh, S. V. Atre, *J. Am. Chem. Soc.*, (1995) **117**, 9529.
[28] J. F. Moulder, W. E. Stickle, P. E. Sobol, K. D. Bomben, J. Chastain, *Handbook of X-ray Photo-electron Spectroscopy*, Perkin-Elmer Corp., Eden Prairie, MN, (1992).
[29] G. Kaindl, T.-C. Chiang, D. E. Eastman, F. J. Himpsel, *Phys. Rev. Lett.*, (1980) **45**, 1808.
[30] C. M. Whelan, M. R. Smyth, C. J. Barnes, N. M. D. Brown, C. A. Anderson, *App. Surf. Sci.*, (1998) **134**, 144.
[31] Y.-W. Yang, L.-J. Fan, *Langmuir*, (2002) **18**, 1157.
[32] T. Ishida, N. Choi, W. Mizutani, H.Tokumoto, I. Kojima, H. Azehara, H. Hokari, U. Akiba, M. Fujihira, *Langmuir*, (1999) **15**, 6799.
[33] C. M. Whelan, C. J. Barnes, C. J. H. Walker, N. M. D. Brown, *Surf. Sci.*, (1999) **425**, 195.
[34] S. Frey, V. Stadler, K. Heister, W. Eck, M. Zharnikov, M. Grunze, *Langmuir*, (2001) **17**, 2408.
[35] L.-J. Wan, M. Terashima, H. Noda, M. Osawa, *J. Phys. Chem. B.*, (2000) **104**, 3563.
[36] A. Abduaini, S. Kera, M. Aoki, K. K. Okudaira, N. Ueno, Y. Harada, *J. Electron. Spectrosc. Relat. Phenom.*, (1998) **88-91**, 849.
[37] M. Takahashi, M. Fujita, M. Ito, *Surf. Sci.*, (1985) **158**, 307.
[38] K. B. Biggs, J. P. Camden, J. N. Anker, R. P. van Duyne, *J. Phys. Chem. A.*, (2009) **133**, 4581.
[39] G. Xue, M. Ma, J. Zhang, Y. Lu, *Journal of Colloid and Interface Science*, (1992) **150**, 1.
[40] C. A. Szafranski, W. Tanner, P. E. Laibinis, R. L. Garrell, *Langmuir*, (1998) **14**, 3570.
[41] H. Nichols, R. M. Hexter, *J. Chem. Phys.*, (1981) **75**, 3126.
[42] J. A. Creighton, *Surf. Sci.*, (1983) **124**, 209.

[43] P. Kao, N. A. Malvadkar, M. Cetinkaya, H. Wang, D. L. Allara, M. C. Demirel, *Adv. Mater.*, (2008) **20**, 3562.
[44] E.-C. Lin, J. Fang, S.-C. Park, F. W. Johnson, H. O. Jacobs, *Nat. Comm.*, (2013) **4**, 1.
[45] J. F. Kang, A. Ulman, S. Liao, R. Jordan, C. Yang, G. Liu, *Langmuir*, (2001) **17**, 95.
[46] J. F. Kang, S. Liao, R. Jordan, A. Ulman, *J. Am. Chem. Soc.*, (1998) **120**, 9662.
[47] S. Liao, Y. Shnidman, A. Ulman, *J. Am. Chem. Soc.*, (2000) **122**, 3688.
[48] S. Khodabakhsh, *Use of Self-Assembled Monolayers in Organic Semiconductor Devices.* (2005) Ph.D. Thesis, Imperial College London, U.K.
[49] P. A. Mosier-Boss, S. H. Lieberman, *Analytica Chimica Acta.*, (2003) **488**, 15.
[50] J. H. S. Green, *Trans. Faraday Soc.*, (1963) **59**, 1559.
[51] O. Levine, W. A. Zisman, *J. Phys. Chem.*, (1957) **61**, 1188.
[52] C. D. Bain, J. Evall, G. M. Whitesides, *J. Am. Chem. Soc.*, (1989) **111**, 7155.
[53] Q. Jin, J. A. Rodriguez, C. Z. Li, Y. Darici, N. J. Tao, *Surf. Sci.*, (1999) **425**, 101.

Chapter 4

Small Molecule/Polymer Binder Organic Thin-Film Transistors Utilising 6,13-bis(triisopropylsilylethynyl)-pentacene

This chapter discusses the influence of SAM modification of the source/drain contacts and its relation to device performance in OTFTs, utilising 6,13-bis(triisopropylsilylethynyl)-pentacene (TIPS-pentacene) in conjunction with the polymer binder, poly(4-methylstyrene) (P4MS) in forming an active-blend organic semiconductor. The impact on morphology of the active-blend thin-film associated with the properties of specifically selected aromatic thiols discussed in **Chapter 3** is investigated. Correlations between OTFT device parameters and the influence of surface energy properties of the underlying substrate on the resulting active-blend morphology, alongside the energetic properties relating to charge-injection associated with the work function of the charge injecting electrode are discussed. Particular emphasis on electrode functionalisation by PFBT and 4-FTP are made throughout this chapter.

4.1 Introduction

The field of carbon-based electronics is focussed towards the achievement of solution-processable organic semiconductors with high charge-carrier mobility and minimal degradation issues. The study of polycyclic aromatic hydrocarbons (a.k.a. linear acenes or oligoacenes) composed of laterally fused benzene rings, has led to extensive research into small molecule organic semiconductors. Although this field of research is gradually expanding, the major focus of this area is towards optimising the device-to-device uniformity and operational stability which hinders OTFT

performance. Widely studied soluble small molecules such as TIPS-pentacene and 2,8-difluoro-5,11-bis(triethylsilylethynyl)anthradithiophene (diF-TES-ADT) have been reported as producing some of the highest field-effect mobilities when processed from solution. Commercially available organic semiconductors have reached mobility values > 5 $cm^2\ V^{-1}s^{-1}$ which is sufficient to satisfy 1st and 2nd generation developments, but fabrication processes compromise achieving such mobilities in OTFTs. Several fabrication steps have major implications on the performance of OTFTs, such as the preparation of the semiconductor (e.g. solvent properties, weight percentage, and processing temperature) to how it is deposited onto a substrate. A critical limitation of OTFTs is the ability to control the charge injection at the metal/organic semiconductor interface, where concentrated efforts are being made to improve upon such issues. Increases in I_{off} after long term exposure of the device to atmospheric conditions can severely degrade device performance, where such undesirable increases result in extreme difficulties in switching off the OTFT. In this instance, the semiconductor is known to become doped due to exposure to atmospheric contaminants or light (i.e. photo-oxidation) leading to alterations in the electronic properties of the material. A brief description of the organic semiconductors used in this work will now follow.

4.1.1 Organic Semiconductors - Pentacene and TIPS-pentacene

Thermally evaporated films of pentacene have been widely studied due to its relatively high field-effect mobility (< 1.5 $cm^2\ V^{-1}s^{-1}$).[1] This planar polycyclic hydrocarbon formed of five fused benzene rings (see **Fig.4.1**) arranges into a herringbone structure with a triclinic single crystal orientation ($a \neq b \neq c$, $\alpha \neq \beta \neq \gamma$) with two molecules per unit cell.[2] Pentacene can condense into two crystal phases

that are closely related, but not perfectly matched.[3] This results in polymorphic crystal growth which severely limits mobility through the layer, related to the misalignment between grains. Additionally, pentacene is insoluble and prone to oxidation, specifically at the 6 and 13 positions which disrupts its crystallisation and

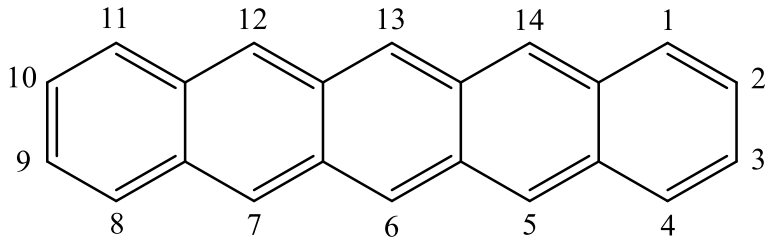

Figure 4.1: Chemical structure of pentacene with allocated numerical ordering of bond positions.

transport properties. These caveats resulted in the synthetic design of TIPS-pentacene (see **Fig.4.2(a)**), a solution-processable organic semiconductor with excellent solubility in a range of organic solvents. Soluble derivatives of pentacene were first synthesised by Anthony *et al.* with the objective of reducing the ease of oxidation, constraining the crystallisation into a single highly favourable phase, and forming a soluble alternative for cheaper and faster deposition.[4] In the case of TIPS-pentacene, bulky functional trialkylsilyl side-groups (e.g. trimethylsilyl (TMS), triethylsilyl (TES)) are substituted at the 6,13-positions of the pentacene backbone, which aid in imparting solubility. These substituents are separated from the pentacene core by a rigid alkyne spacer to allow the closest possible contact between the aromatic rings, and positioned in such a way to minimise their effect on diminishing the electronic properties of the material and benefit crystal packing.

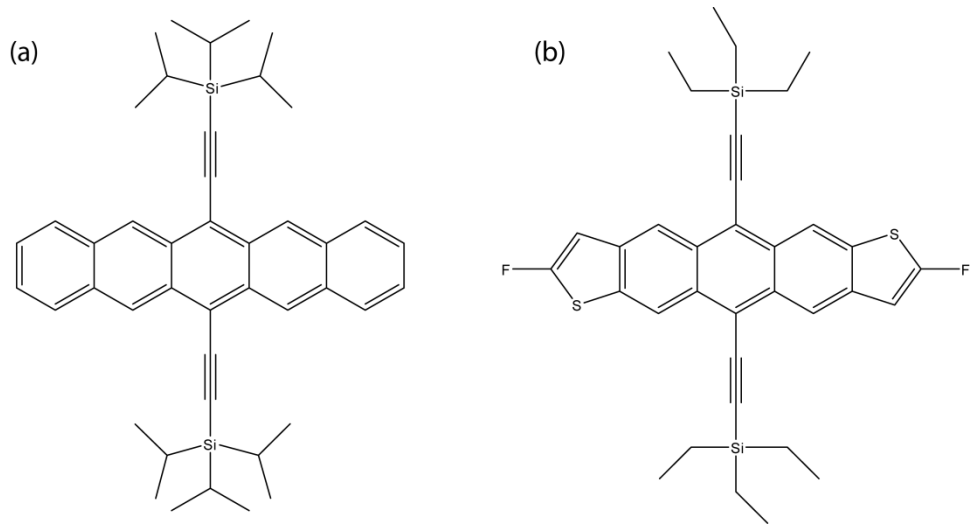

Figure 4.2: (a) 6,13 bis (triisopropyl-silylethynyl) pentacene (TIPS-pentacene) and (b) 2,8-difluoro-5,11-Bis(triethylsilylethynyl)anthradithiophene (diF-TES-ADT).

The adopted structure of TIPS-pentacene forms a lamellar structure with a 2D 'brick-like' motif which has a general ascendancy over that of 'slipped stacked' structuring.[5] This 2D columnar array has a large overlap between the aromatic rings of neighbouring molecules, which provides increased overlap between the pentacene backbone in neighbouring adjacent molecules due to the face-to-face motif, rather than a face-to-edge. Leading research by Anthony *et al.* has shown the importance of close molecular packing of acene-based organic semiconductors and its effectiveness in π-stacking.[5] The molecular orientation of the organic semiconductor can be greatly influenced when forming an interface with the underlying substrate, preferentially orientating parallel (i.e. face-on) or perpendicular (i.e. edge-on) to the substrate, of which the latter of these orientations is known to provide higher field-effect mobility.[5]

The organic semiconductor diF-TES-ADT, shown in **Fig.4.2(b)**, has a similar molecular configuration to TIPS-pentacene and adopts a 2D π-stacking motif which

offers high single-crystal mobilities in the order of 1 - 6 $cm^2 V^{-1}s^{-1}$ and 0.5 – 1.5 $cm^2 V^{-1}s^{-1}$ in thin films processed from solution.[6] This small molecule will be discussed in **Chapter 5** following similar processing methods optimised herein for TIPS-pentacene.

4.2 Results and Discussion

4.2.1 Morphology of Pentacene Thin-Films

Organic semiconductors formed from the vapour phase by vacuum deposition have been widely investigated in terms of understanding film morphology and molecular ordering.[5] The structural properties of such films are strongly dictated by their bulk and interfacial properties, therefore the ability to control the molecular growth of an organic semiconductor is advantageous for improving device performance. Pentacene thin-films are known to form highly ordered polycrystalline films displaying dendritic structuring. Displayed in **Fig.4.3** are AFM micrographs of evaporated pentacene thin-films (c.a. 40 nm) deposited on glass (i.e. the channel region of the OTFT) and Ag (i.e. source/drain electrodes) surfaces. AFM micrographs of pentacene deposited onto non-modified Ag and glass are shown in **Fig.4.3(a)** and **Fig.4.3(b)**, respectively. Alternatively, pentacene deposition onto a heated substrate held at 60 °C formed on functionalised Ag with PFBT and glass are shown in **Fig.4.3(c)** and **Fig.4.3(d)**, respectively, which present the characteristic dendritic grain structuring of pentacene. The formation of large pentacene grains is strongly influenced by the surface properties of the substrate, therefore methods such as SAM treatment and elevated substrate temperatures can help induce preferential molecular crystal ordering in the deposited film. The structural ordering of pentacene is highly crystalline, displaying a herringbone structure which offers minimal π-

stacking. Due to this structuring poor dispersion of the electronic bands between pentacene molecules occurs, leading to charge transport properties being limited by crystal orientation. Research conducted using vacuum deposited pentacene has shown pentacene molecules to stand almost perpendicular to the substrate when deposited onto hydrophobic (i.e. non-polar) surfaces, alternatively hydrophilic (i.e. polar) surfaces tend to cause the pentacene molecule to orientate parallel to the substrate.[7] There are significant variations in the pentacene morphology between **Fig.4.3(a)** and **Fig.4.3(c)** formed on Ag, where the static water contact angle

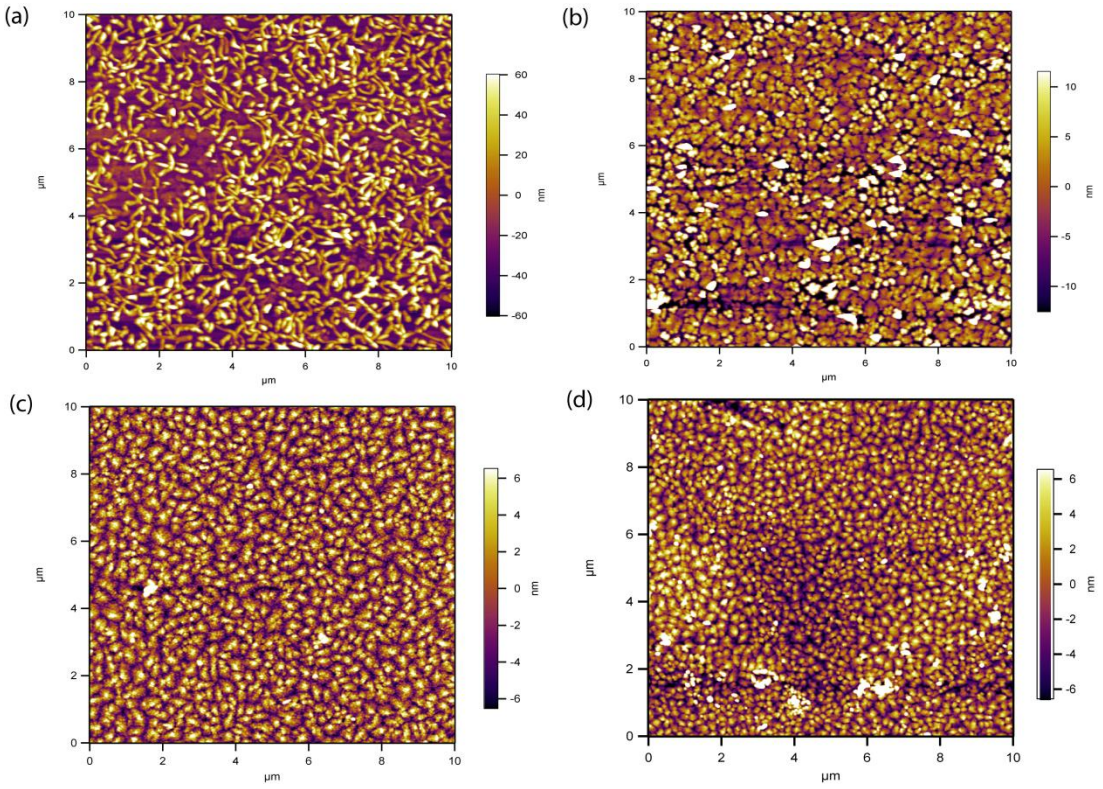

Figure 4.3: AFM micrographs of pentacene (~20 nm) thermally evaporated on (a) bare Ag electrode surface and (b) the respective glass substrate between source/drain, (c) 4-FTP modified Ag, and (d) its respective glass substrate.

measurements of the Ag surface gave an increase of 11 ± 1° after thiol modification, producing a more hydrophobic surface. Minimal fluctuations in the glass contact

angle was observed for **Fig.4.3(b)** and **Fig.4.3(d)** although the morphology appears subtly different, with much smaller grains formed after SAM treatment of the electrodes. Hydrophobic surfaces have been shown to benefit pentacene OTFT devices favouring higher mobility,[8] associated with the resulting perpendicular orientation, ensuring delocalised intermolecular states are formed in the direction parallel to the substrate which is in the transport direction of the OTFT.[9] In relation to field-effect mobility, increases in charge-transport were also associated with larger grain size and increased molecular surface mobility, which is a dominant feature in **Fig.4.3(c)**. The mobility of pentacene thin-films strongly depends on film morphology which can be controlled by substrate temperature, evaporation rate, and sticking coefficients associated with the target surface. Solution-processing of pentacene is very difficult due to its reluctance to solubilise but mobility values ranging between 0.1 – 0.3 cm^2 $V^{-1}s^{-1}$ have been reported for soluble pentacene precursors.[10]

Vacuum deposition of such organic materials is undesirable if low-cost device fabrication of OTFTs is to be achieved. Solution-processing methods for large-area, cost-effective production at low temperature and ambient conditions is required. The remaining focus of this chapter is towards solution-processing of OTFTs by spin-coating.

4.2.2 Formulation and Device Performance of Active-blend OTFTs

This section discusses the influence of SAMs on the device performance of TIPS-pentacene/polymer binder OTFTs. The surface morphology of the deposited layer was investigated and molecular ordering within the device was also studied.

The organic solvent 1,3,5-trimethylbenzene (aka. mesitylene) was chosen for all OSC formulations due to its good solubility of TIPS-pentacene and polymer binders used in this study. Solvents with minimal toxicity levels and the presence of non-halogenated elements were a major consideration for all solution-processed layers with particular emphasis on the active-blend layer and SAM in this study. The chemical properties of the solvent are of key importance in controlling the crystal growth of the thin-film active-blend layer. Good device performance and thin-film morphology was achieved through utilising mesitylene by spin-coating, therefore this formulation parameter was not changed and applied throughout this work. The relatively moderate boiling point for mesitylene at 165 °C bodes well for spin coating preparation of active-blend formulations, as high boiling point solvents aid in reducing evaporation rates and allow time for vertical phase separation to occur.[11] High mobility OTFTs using TIPS-pentacene have been reported with 1,2-dichlorobenzene and 1,2,3,4-Tetrahydronapthalene (aka. tetralin) relating closely to the high boiling point for these organic solvents, particularly in the case of tetralin. The slow evaporation rate of which facilitates the growth of highly crystalline films.[12,13] The important properties of the solvents which play a critical role in the structural ordering of the active-blend layer relies not only on the boiling point, but the vapour pressure and miscibility of the organic semiconductor.

A total solid content of 2% was adopted for all studies at a ratio of 4:1 in favour of TIPS-pentacene, giving a weight loading of 1.6 wt% for the small molecule constituent. The formulation was completed by the addition of mesitylene (relative density = 0.86 g/mol) and left shaking for several hours under ambient conditions to aid solvation. No particulates were observed in the solution proving good miscibility of both materials. Associated spin-coating parameters for

processing of the active-blend layer were 1500 rpm for 30 seconds (acceleration = 1000 rpm/s) with 1 minute post-treatment annealing at 100 °C. Formulations consisting solely of TIPS-pentacene provide poor transfer characteristics (i.e. large subthreshold swing and high $I_{on/off}$ ratios) and mobility values < 0.1 $cm^2 V^{-1} s^{-1}$. The ratio of small molecule to binder was investigated which showed lowering the ratio below 2:1 in favour of the small molecule gave uncharacteristic I-V curves, as shown in **Fig.4.4**. Increased solution viscosity is expected by the inclusion of P4MS therefore a critical amount may be required to form a continuous thin-film at such spin-speeds.[11,14]

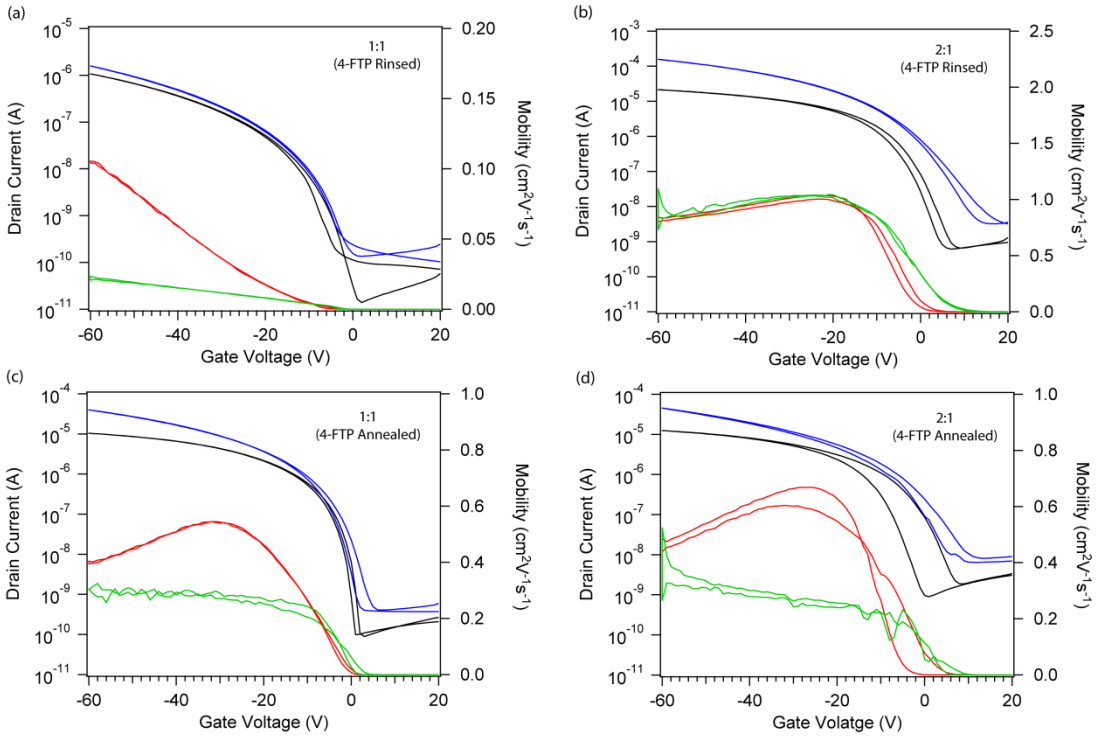

Figure 4.4: I-V characteristics of TIPS:P4MS devices at ratios of 1:1 and 2:1 prepared on (a, b) 4-FTP rinsed and (c, d) 4-FTP annealed at 140 °C electrodes, respectively.

The following section will discuss the influence of SAM modification of the source/drain contacts and how this processing step can be used to optimise OTFT performance.

4.2.3 Influence of Thiol Assembly Time on OTFT Performance

The formation and surface structuring of thiols on noble metals are highly dependent on the assembly time required for complete saturation of the surface as well as other preparation parameters as discussed in **Chapter 3**. The formation of a monolayer can involve an extensive assembly time where the occupation of all active binding sites on the electrode surface is dependent on the surface conditions of the metal, the surfactant properties, and environmental conditions. As discussed previously, the charge-injection current in an OTFT is dominated by hole-carrier conduction due to the poor electron transporting properties of TIPS-pentacene, therefore sweeping negative gate-biases were applied.

The device performance between the two immersion times for both PFBT and 4-FTP show a common trend where the I-V characteristics are reduced with increased thiol treatment, shown in **Fig.4.5**. This result indicates that a significantly long immersion times did not aid in improving the charge-injection properties at this interface but in fact had a negative impact on the overall device performance. A summary of device parameters are tabulated in **Table 4.1**. Theoretically, the completion of a monolayer would provide uniform surface properties in terms of minimising fluctuations in surface energy and work function (discussed in **Chapter 3**). It is possible that although such surface characteristics are advantageous, effects such as solvent trapping, multilayer formation, and unfavourable reactivity of the surfactant solution with the metal over longer immersion times may present

unfavourable surface properties at the electrode/semiconductor interface. The bright

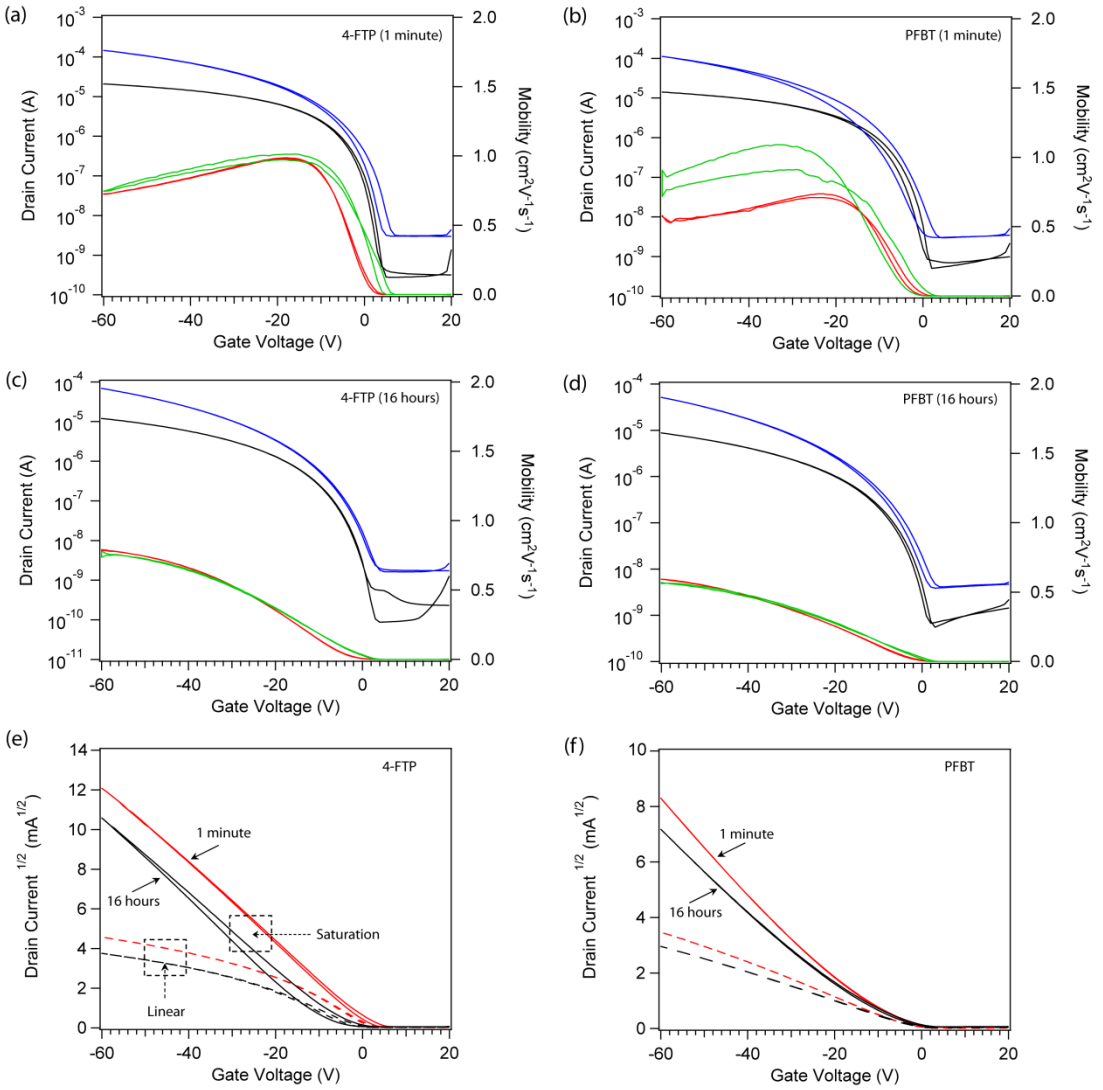

Figure 4.5: Transfer characteristics of 4-FTP and PFBT modified electrodes after immersion times of 1 minute and 16 hours. (a) 4-FTP 1 minute; (b) PFBT 1 minute; (c) 4-FTP 16 hours; (d) PFBT 16 hours; and respective linear curves of (e) 4-FTP and (f) PFBT.

field optical microscope images of the TIPS/P4MS thin-film, shown in **Fig.4.6(a)**, displays etching of the Ag electrode along its edge and the appearance of pin-hole defects in the active-blend layer for 4-FTP 16 hour immersed substrates. **Fig.4.6(b)**

shows significant dewetting of the TIPS/P4MS active-blend layer on a PFBT modified electrode.

Table 4.1: Summary of device performance after SAM immersion time of 1 minute and 16 hours.

Sample	μ_{lin}	μ_{sat}	$I_{on/off}$	S_{lin}	S_{sat}	V_T	V_{on}
4-FTP (1 min)	0.99	1.01	10^4	1.39	2.32	4	4
4-FTP (16 hours)	0.79	0.78	10^4	1.96	3.56	-6	3
PFBT (1 min)	0.81	0.79	10^5	1.11	2.29	-1	3
PFBT (16 hours)	0.59	0.57	10^4	2.52	4.45	-5	2

These variations in device performance for PFBT modified surfaces are associated to an increase in the static water contact angle by 10±1°. This may cause unfavourable surface conditions associated with PFBT when spin-coating due to the increased hydrophobicity. In comparison to 4-FTP the contact angle only varied by 3±1° after 16 hours, displaying no obvious dewetting features. These results correlate with the work discussed in **Chapter 3**. The appearance of pin-hole defects in the active-blend layer appeared to result from etching of the Ag surface by the thiol and may have been exaggerated by the low adhesion of the metal electrode to the glass substrate. **Table 4.2** shows the change in contact angle from 1 minute to 16 hours. The immersion process has clear implications resulting mainly in the removal of the metal contacts and potential erosion of the underlying substrate. Long immersion times of aromatic thiols have clear implications on the integrity of the source/drain contacts. Consequentially, the continuation of this thesis concerns only 1 minute assembly times for all SAM treatments.

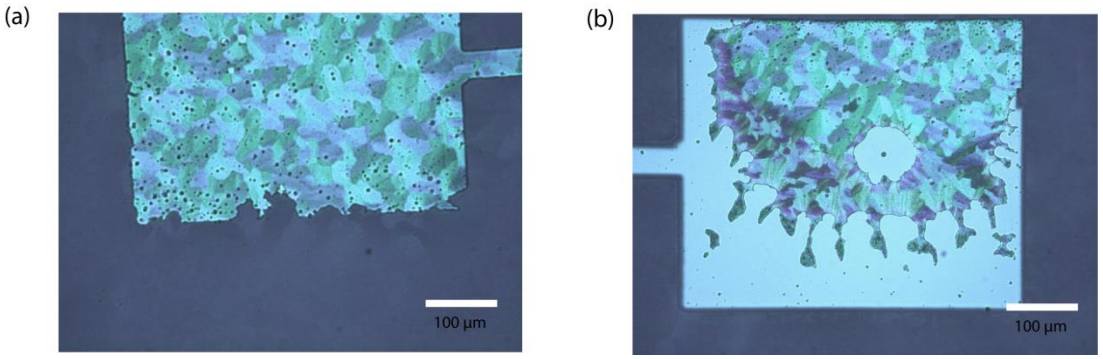

Figure 4.6: Optical microscope images of TIPS/P4MS spin-coated onto SAM treated Au electrodes after 16 hour immersion times with (a) 4-FTP and (b) PFBT.

Dewetting of the semiconductor layer with respect to the underlying substrates also varied considerably due to uncontrollable changes in atmospheric conditions. A noticeable reduction in the yield of working OTFTs occurred with increased humidity (> 60%), leading to dewetting of the semiconductor on the substrate. Non-continuous film formation under such atmospheric processing conditions was frequently observed which suggests unfavourable changes in the surface energy of the substrate. Following these results the continuation of this thesis discusses only 1 minute SAM treatments.

Table 4.2: Static water contact angles for PFBT and 4-FTP over designated immersion times

Time	PFBT (°)	4-FTP (°)
1 minute	99±3	87±1
15 minutes	107±1	90±2
16 hours	109±1	89±2

4.2.4 Influence of Source/Drain Post-Treatment on OTFT Performance

The source/drain electrodes were investigated under two different post-treatment steps by rinsing of the substrate with solvent (i.e. anhydrous IPA) or heating of the substrate at 140 °C for 1 minute as an additional process. All post treatment occurred with a time period of 5 minutes after thiol treatment of the source/drain electrodes. The transfer and output curves for PFBT treated electrodes after solvent rinsing and annealing are displayed in **Fig.4.7(a)** and **Fig.4.7(b)**, respectively. Additionally, the transfer and output curves for 4-FTP modified contacts after solvent rinsing and annealing are shown in **Fig.4.7(c)** and **Fig.4.7(d)**, respectively.

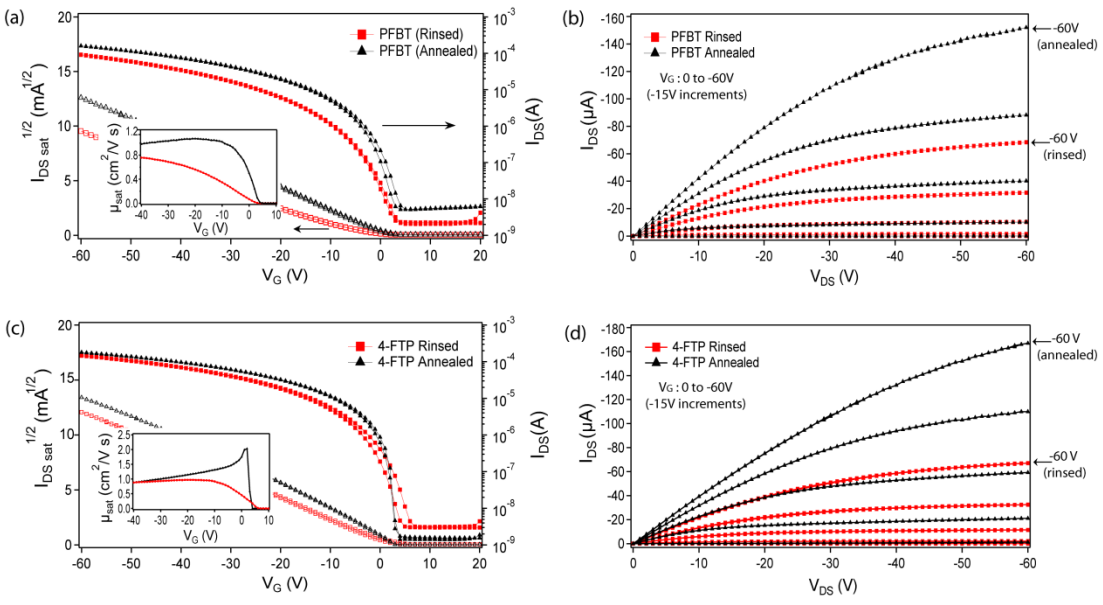

Figure 4.7: Transfer (saturation regime) and output characteristic for (a, b) PFBT and (c, d) 4-FTP, respectively. Saturation mobility curves (forwards scan only) included as insets.

Post-treatment annealing of the modified electrode displayed beneficial results for both respective thiols. An increase in peak saturation mobility from 0.8

$cm^2\ V^{-1}\ s^{-1}$ to 1.1 $cm^2\ V^{-1}\ s^{-1}$ (inset **Fig.4.7(a)**) was observed for PFBT rinsed and annealed devices, respectively, with similar behaviour seen for 4-FTP with peak saturation mobility reaching 0.9 $cm^2\ V^{-1}\ s^{-1}$ and 2 $cm^2\ V^{-1}\ s^{-1}$ (inset **Fig.4.7(b)**). Improvements in device performance by annealing manifested itself in the transfer curve through lower sub-threshold swing and higher field-effect mobility. Additionally, the resulting output curves displayed enhanced drain-currents for annealed devices indicating a more conductive channel. This is highly beneficial in terms of device stability and would be ideal in backplanes for AMOLEDs. Annealing at such temperatures is still viable for most low-cost plastic substrates, such as polyethylene terephthalate (PET) or polyethylene naphthalate (PEN), which are commonly restricted to temperatures below their glass transition temperature (T_g) around 100 °C.[15]

The shape of the mobility curve for PFBT devices displayed good characteristic behaviour with closely matched linear and saturation mobility. Similar behaviour was observed for 4-FTP rinsed devices, but a significantly different mobility profile was observed for 4-FTP annealed device, specifically in the saturation regime (inset **Fig.4.7(c)**). A sharp rise in saturation mobility (trace curve) occurred at low gate voltages ($V_{GS} \approx 2V$), whereas the saturation mobility (retrace curve) followed a similar profile but presented no characteristic peak as displayed in the trace curve. This was an inherent feature to the shape of 4-FTP annealed saturation mobility curve, which was reproducible with repeat measurements and highly representative of these devices.

The shape of the saturation mobility curve in **Fig.4.7(c)** displays characteristic features of gate-voltage dependence due to the gradual reduction in mobility with increasing gate bias. This is commonly a result of defects acting as

charge-trap sites in the semiconductor layer.[16] The initial rise in mobility has been described in several theoretical models which associate this behaviour to the filling of trap-sites as the gate-voltage increase or the presence of the localised states existing at the band-edge. This variation in mobility is tentatively assigned to influences in the bulk of the semiconductor and accumulation of charges at the gate-dielectric interface, hence a possible increased mobility in the bulk of the semiconductor but lower mobility at the conducting channel. At low gate voltages the saturation mobility curve indicates a possible thermal activation of charge-carriers. The shape of the mobility curve is influenced by a competing phenomenon, where the filling of the Gaussian distribution of states is controlled by the gate bias, thus increasing the charge-carrier mobility, and subsequently the series resistance, which resultantly decreases the mobility in the device.[17] It can be assumed that at higher temperatures (> 300K) the channel resistance decreases, leading to the series resistance becoming increasingly detrimental to device performance, thus resulting in charge-carrier mobility decreasing with increasing gate voltage.

Increased μ_{sat} values over μ_{lin} is commonly ascribed to effects such as contact resistance which is less likely to limit the drain current in the saturation regime than in the linear regime. This is expected as at high gate voltages, as the ratio of the channel resistance to contact resistance decreases, therefore the current depends more heavily on the contact properties.[18] This assumption is reasonable as contact resistance is not accounted for in the linear (**Equation 1.3**) and saturation (**Equation 1.4**) equations, although efforts to correct for this effect still lead to discrepancies between the two regimes.[18] This higher mobility for 4-FTP annealed OTFTs may relate to enhanced inter-grain connectivity which will be discussed in *Section 4.6*. Another contributing factor is the degree of vertical phase segregation in

the thin-film which commonly occurs for small molecule/polymer blends. Both these influential features will be discussed in the following sections.

Two mechanisms possibly occurring at the interfaces between the OSC formed with the metal and the substrate are the interaction between residual solvent present within the SAM, and secondly, the intrinsic dipole moment related to the polarity of the solvent. Solvent may remain on the metal and glass surface after both post-treatments rinsing for the devices discussed in **Fig.4.7** which may explain the reduction in mobility observed. Interaction of the thiol or residual solvent with the exposed underlying substrate could cause a disturbance in the formation of the OSC. It is speculated that remaining traces of thiols or solvent could aggregate on the glass or dielectric surface (in the case of BG devices) causing hindrance at the dielectric/semiconductor interface where the channel forms. Static contact angle measurements indicate a small change in surface wettability which is discussed in *Section 5.2* of **Chapter 5**.

4.2.5 Molecular Ordering of Active-Blend Layer

The molecular ordering of TIPS-pentacene thin-films and its crystal alignment across both the electrode and substrate surface relate closely with OTFT device performance. Optimisation of processing procedures and formulation parameters can aid in improving assembly of the organic semiconductor leading to enhanced conductive pathways for charge-carriers. Whether the backbone of the TIPS-pentacene molecule is lying-down or positioned upright normal to the electrode surface, can heavily influence charge-transport in OTFTs. In-plane source/drain electrodes rely on charge transport parallel to the substrate, therefore ideal alignment providing the strongest π-π stacking is in the direction parallel to the current flow within the channel. Surface modification of the electrode through the

introduction of SAMs or a passivation layer with regards to the substrate can help to change the surface energy properties of the underlying surface, promoting enhanced crystal structuring of the active-blend layer under optimised conditions.

TIPS-pentacene single crystals form a triclinic structure with two-dimensional π-stacking, forming a unit cell whose parameters are a = 7.5650 Å, b = 7.7500 Å, c = 16.835 Å, α = 89.15 °, β = 92.713 °, γ = 83.63 °.[19] The XRD response shown in **Fig.4.8** confirms the TIPS/P4MS films to be highly ordered with the diffraction peaks corresponding to an intermolecular spacing (i.e. d_{001}-spacing) of 17.31 Å (2θ = 5.1 °). This result indicates good vertical periodicity but the measured spacing is slightly higher than the c-lattice axis of 16.84 Å of TIPS-pentacene.[16,20] This result is likely to be due to the presence of P4MS in the thin-film which has influence its molecular ordering. A drop-cast film of TIPS/P4MS prepared in

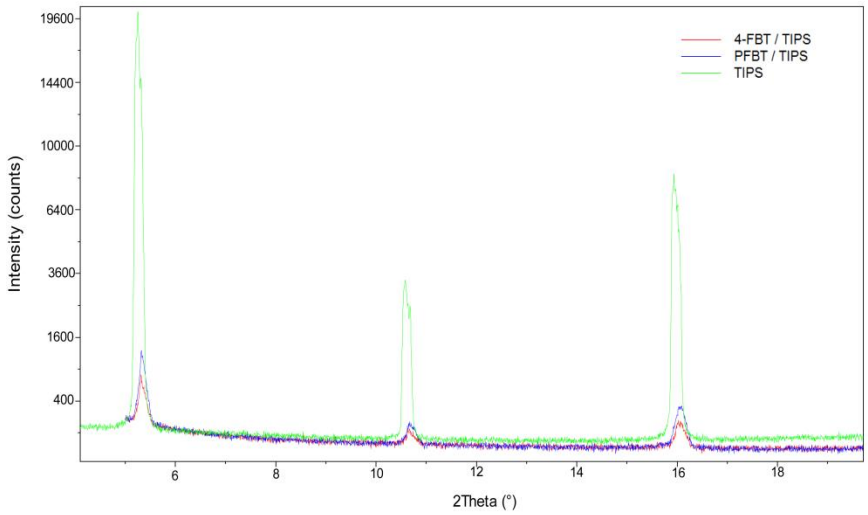

Figure 4.8: X-ray diffractograms of TIPS/P4MS spin coated thin-films formed on PFBT (blue) and 4-FTP (red) modified substrates alongside drop-cast film of TIPS-pentacene (green).

mesitylene was investigated on glass due to dewetting occurring when spin-coating (see green profile in **Fig.4.8**). The highly crystalline nature of this organic semiconductor was seen from the drop-cast due to the enhance relative intensity. The d_{001}-spacing for this film was measured at 17.83 Å (2θ = 4.95 °) which indicates worse vertical molecular packing in the drop-cast film. The spin-cast films display better molecular structuring in the thin-film but deviate slightly from a single-crystal packing.

The spin-cast thin-films of TIPS/P4MS were studied on PFBT and 4-FTP annealed substrates. No discernible differences were observed between the films which both displayed the commonly observed *00l* peaks associated with two-dimensional π-stacking structure in the out-of-plane direction of the film. The enhanced intensity associated with the drop-cast film is related to the increased thickness of this film. The molecular orientation of the TIPS-pentacene molecule is heavily influenced by the metal electrode which leads to its crystal growth and elongation into the channel region from the electrodes. Whether the backbone of the TIPS-pentacene film is lying-down or standing upright normal to the electrode surface can influence charge-transport.

To date, experimental evidence has strongly supported charge-carrier transport and its association with intermolecular π-orbital overlap. Charge transport in OTFTs is critically dependent on the molecular spacing and tilt angles between the semiconducting molecules, with optimum molecular packing being widely studied by computational simulations.

4.2.6 Morphology Study of TIPS/P4MS Blend Thin-Films

Preparation of TIPS-pentacene without the presence of a polymer binder led to inhomogeneous film formation, offering low mobility and uncharacteristic device

switching behaviour. The I-V curves and parameters for this device are presented in **Fig.4.9** and **Table 4.3**, respectively. Additionally, devices prepared without SAM

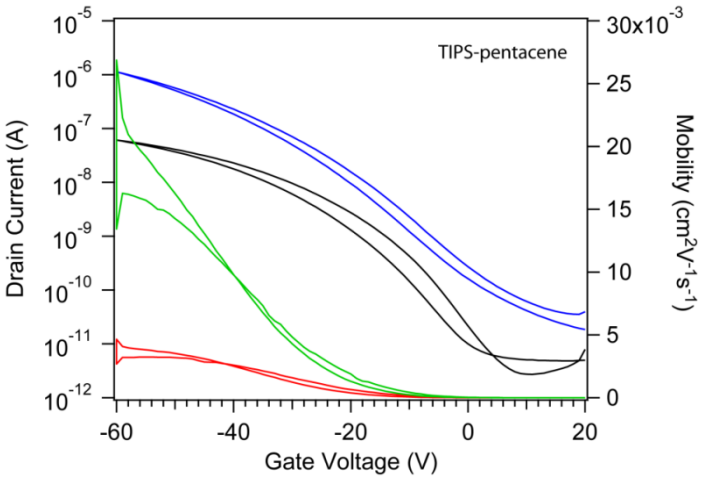

Fig.4.9: Device performance of TIPS-pentacene with no binder. Device prepared using 4-FTP annealed at 140 °C.

Table 4.3: Device parameters of TIPS-pentacene devices with no polymer binder.

Sample	μ_{lin}	μ_{sat}	$I_{on/off}$	S_{lin}	S_{sat}	V_T	V_{on}
TIPS (ONLY)	0.005	0.021	10^4	6.91	10.22	-20	4

modification of the source/drain electrodes, utilising a TIPS/P4MS active-blend layer, led to dewetting of the active-blend layer during spin-coating due to unfavourable substrate conditions. The polarised optical microscope images of the active-blend thin-film are shown in **Fig.4.10.** for PFBT (a, b) and 4-FTP (c, d) rinsed and annealed substrates, respectively. All images were captured before subsequent deposition of the dielectric and gate electrode. The PFBT modified electrodes under both post treatments display the formation of large crystals within and across the channel region. The 4-FTP modified electrodes display clear differences between rinsed and annealed post-treatment shown in **Fig.4.10(c)** and **Fig.4.10(d)**,

respectively. Strong birefringence is observed for TIPS/P4MS thin-films on 4-FTP annealed electrodes which suggests the crystals form a common orientation amongst

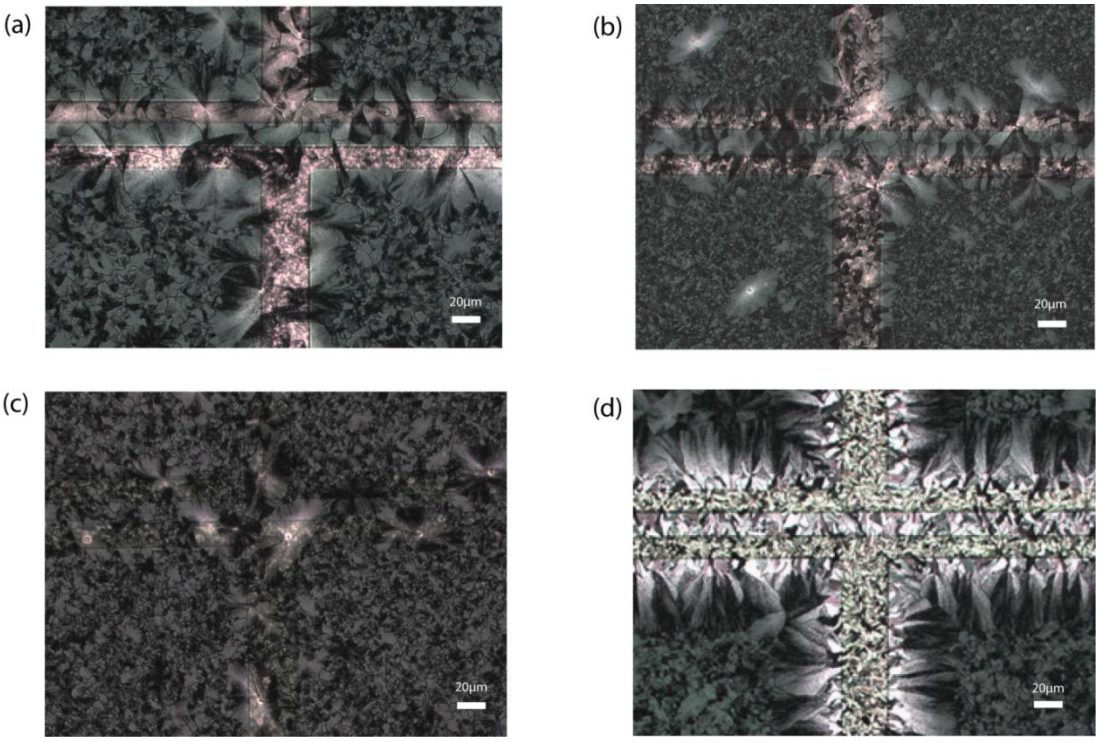

Figure 4.10: Polarised optical microscope images of TIPS/P4MS blends on (a, b) PFBT and (c, d) 4-FTP rinsed and annealed substrates respectively. The channel lengths in all images are 20µm.

the crystalline domains. In contrast, the absence of such birefringence in **Fig.4.10(c)** implies the active-blend is highly amorphous. All devices offered good I-V characteristics with high mobility but samples displaying strong birefringence from the thin-film active-blend layer produced higher peak saturation mobility and much steeper parabolic slope to their transfer curves as discussed previously.

Fig.4.11. displays AFM micrographs of the active-blend layer within the channel region after (a) rinsing (b) and annealing of 4-FTP modified devices. The thin-film microstructure for both images display small elongated grain structures

across the source/drain electrodes and within the channel region formed on the glass substrate. The structuring of the grains in **Fig.4.11(a)** appears to be unevenly distributed within the channel and irregular directional orientation between grains. When the 4-FTP electrode is annealed these grains appear more closely packed and display better directional ordering within their domains as seen in **Fig.4.11(b)**. The

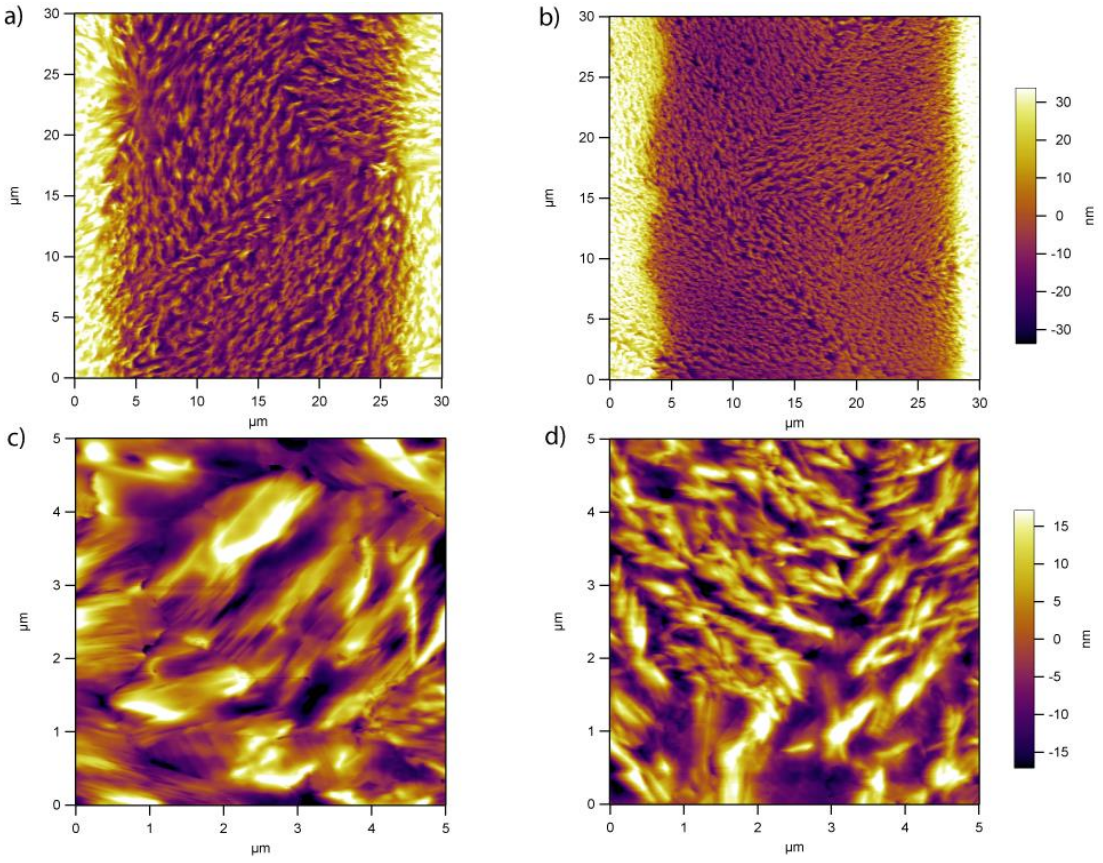

Figure 4.11: AFM micrographs of TIPS/P4MS topography within the channel region for (a) 4-FTP rinsed and (b) 4-FTP annealed substrates. Source/drain electrodes appear either side of the channel in both images. Smaller scans of the electrode regions are shown in (c) and (d) for rinsed and annealed surfaces, respectively.

electrode region scans of 4-FTP rinsed devices, shown in **Fig.4.11(c)**, display closely packed crystal formation with low root mean square (R.M.S) roughness of 4.6 nm,

whereas 4-FTP annealed devices, shown in **Fig.4.11(d)**, appears more disordered with an increase in R.M.S roughness to 8.4 nm. The formation of needle–like topography of TIPS-pentacene thin-films have been identified as main cause of hampered charge-transport across the channel region.[20,21] This would be expected of such small grains to severely limit the device performance due to the irregular nucleation of the OSC layer. With this considered, we see excellent subthreshold swing with increased mobility after annealing of the 4-FTP electrode, as well as very low threshold voltage, which indicates a reduced influence from trap-sites at grain boundaries. The shape of the mobility curve for 4-FTP annealed devices may be explained by morphological effects. A rougher semiconductor surface close to the conducting channel can lead to increased gate voltage dependence with charge-carrier mobility.[22] Additionally, smaller grains forming closer to the electrode edge may help to increase uniformity and packing at this interface leading to better charge-injection and extraction from the edges of the contacts. Heightened surface roughness of the underlying substrate, particularly the electrode surface, can cause hindrance of charge-injection/extraction, as the occurrence of voids or non-uniformity in the subsequently deposited organic semiconductor can lead to surface scattering at the dielectric/semiconductor interface. The charge transport within the channel region of the device typically occurs in the first few monolayers of the semiconductor, closest to the dielectric/semiconductor interface, therefore the surface state of the underlying layer prior to completion of this interface has a large impact on charge-carrier mobility.[23,24]

Contrastingly, the PFBT modified devices displayed very different microstructure to what was observed for 4-FTP devices. The morphology of PFBT rinsed transistors, shown in **Fig.4.12(a)**, displays variations in the morphology

formed across both the electrodes and within the channel region. Nucleation of the active-blend on the electrode surface leads to large planar crystalline domains during spin-coating. These crystals grow from the electrode surface, therefore, as they begin to phase segregate and crystallise the interaction between neighbouring grains formed adjacent to one another coalesce leading to the large crystal domains observed. The formation of these crystals are diffusion limited leading to needle-like structures where such crystals are not present, as observed in the centre of the channel.[25] A remarkable change in the active-blend layer morphology is seen after annealing of the PFBT modified electrodes, shown in **Fig.4.12(b)**. Large crystal domains form across the channel region which appear to nucleate and extend from the electrode surface with highly defined directional growth. The active-blend layer surface has much lower morphological uniformity compared to PFBT rinsed electrodes as the crystals are widely separated on both contacts. Although the roughness of the surface is significantly increased, the coalescing and overlapping of the crystals within the channel play a major role in the mobility extracted from this device. To the best of our knowledge, we have not seen this growth behaviour before in other publications with TIPS-pentacene/polymer blend systems. AFM micrographs of the electrode region for PFBT rinsed and annealed are shown in **Fig.4.12(c)** and **Fig.4.12(d)**, respectively. Similar rod-like crystals have been observed for triethylsilylethynyl anthradithiophene (TES-ADT) films after post-thermal annealing at temperatures above 130 °C.[26]

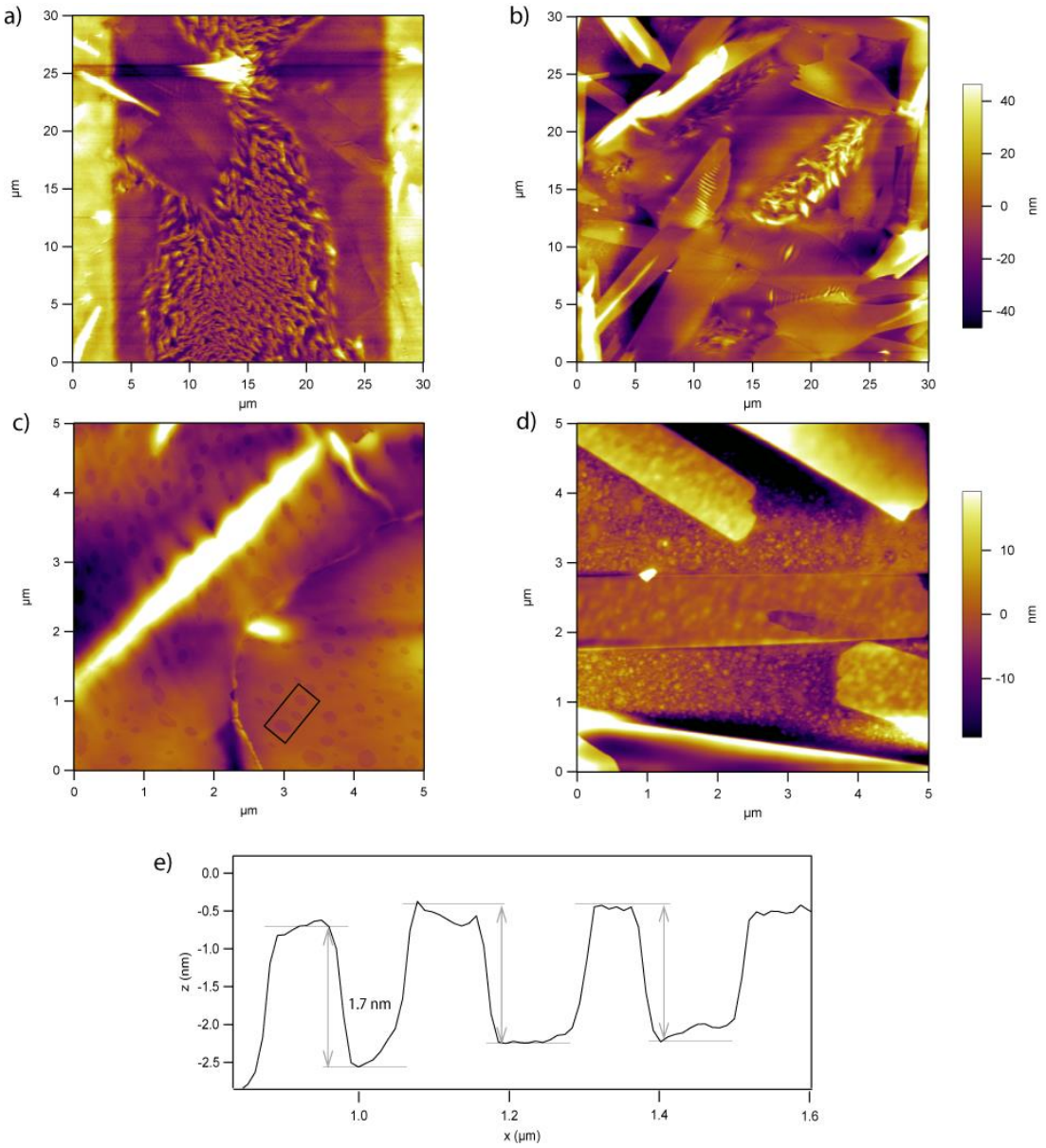

Figure 4.12: AFM micrographs of TIPS/P4MS topography within the channel region of (a) PFBT rinsed and (b) PFBT annealed devices with associated electrode region scans shown underneath in (c) and (d) respectively. The height profile shown in (e) is taken across the micrograph in (c) marked by a rectangular outline.

To investigate the surface composition of the active-blend layer at the air interface static water contact angle measurements were conducted, with all results

summarised in **Table 4.4**. Pure TIPS-pentacene thin-films were prepared on both 4-FTP and PFBT modified Ag surfaces as a comparative study to TIPS/P4MS active-blend layers. Variations in surface coverage of the OSC can influence contact angle values leading to the small disparities. Poorly ordered thin-films of TIPS-pentacene can lead to influences from the underlying substrate, thus decreasing in contact angle values, whereas highly ordered regions may increase the value due to increased concentration and better packing. It is possible that such influences may have contributed to the range of values measured for the pure TIPS-pentacene layers.

Table 4.4: Static contact angle measurements of TIPS-pentacene and TIPS/P4MS thin-films.

Sample	Water (deg)	Standard deviation (deg)
TIPS-pentacene		
4-FTP (Rinsed)	98.7	0.7
4-FTP (Annealed)	106.3	2.1
PFBT (Rinsed)	103.6	0.9
PFBT (Annealed)	107.0	1.8
TIPS/P4MS		
4-FTP (Rinsed)	103.6	1.5
4-FTP (Annealed)	104.9	0.3
PFBT (Rinsed)	103.6	0.2
PFBT (Annealed)	103.5	1.3
P4MS only	71.2	0.5

Averaging over all samples prepared with pure TIPS-pentacene, a contact angle of 103.9 ± 3.8° is obtained which matches very closely with all measurements conducted on TIPS/P4MS thin-films. This provides direct evidence that the TIPS-pentacene forms on the top surface with the P4MS residing below, as the water contact angle of P4MS was measured at 71.8 ± 0.5°.

The static water contact angle values for P4MS and TIPS-pentacene are 71° and 103°, respectively, whereby such distinctive differences in contact angle are

known to favour phase segregation in acene-polymer blends because of differences in surface energy between the two materials. Due to TIPS-pentacene being highly crystalline its proneness to vertically phase segregate is further enhanced by the enthalpic interaction whilst the layer crystallises.[27,28] Due to these effects the TIPS-pentacene segregates to the upper surface whereas the P4MS energetically favours to position itself close to the substrate due to its more polar nature.

The AFM scans present four discernible morphological features present in the thin-film of the TIPS/P4MS active-blend layer. During spin-coating the active-blend nucleates on the thiol-modified electrodes, positioned either side of the channel, where these grains grow laterally along the device surface displaying spherulitic growth (see **Fig.4.12(a)**). Through annealing of the thiol modified electrode as seen in **Fig.4.12(b)**, the grains appear to grow isotropically from a nucleation centre on the electrode, displaying distinctive elongated crystals. The nucleated grains grow in randomised directions until the solvated active material is exhausted. The elongated crystal growth is exclusive to the PFBT modified electrode surface. The domains grow by accretion and are therefore diffusion limited, depending strongly on the proximity of adjacent nucleation sites. There is a tendency for these domains to nucleate towards the electrode edge, with continual growth into the channel until saturation of the solvent.

Fig.4.12(c) displays the formation of large terrace composed of depressions present within the exposed plane, outlined by a boxed region within the image. These morphological features may be a result of fast crystallisation occurring during spin coating, resulting in an incomplete TIPS-pentacene thin-film at the air interface. Annealing of active-blend layer may result in these topological depressions due to the escaping of solvent as the layer phase-separates below.[29] The depths of these

craters correlate closely with the d_{001}-spacing of 1.68 nm associated with the triclinic structuring of the TIPS-pentacene molecules, which is shown by the height profile scan in **Fig.4.12(e)**.[16,20] This indicates that the top surface of the planar crystalline domains forms an incomplete layer of TIPS-pentacene, where the exposure to the layer below signifies that the c-lattice axis in these crystals are positioned normal to the substrate.[20,30] The appearance of such crystals is strong evidence that vertical stratification of TIPS-pentacene has occurred during spin-coating, leading to the semiconductor phase-separating and crystallising at the air interface. The large crystalline regions seen for PFBT modified surfaces are known to assume an 'edge-on' orientation arranging with the TIPS-pentacene long-axis π-π stacking in the [210] direction.[31] However, this crystal orientation is known to severely hinder charge transport, leading to additional conductive pathways in the [120] and [$1\bar{2}0$] directions offering higher charge-carrier mobility.[31]

Fig.4.12(d) displays large extended crystals of the TIPS/P4MS film which have micron sized gaps between themselves. Due to the tendency of this film to produce voids, a reduction in the carrier transport of this device would be expected, although this does not seem to influence the performance, possibly due to potential presence of sufficient conductive pathways.

4.2.7 Structural Ordering of TIPS/P4MS Blend Studied by SIMS

Several insightful techniques have been applied in literature to investigate phase segregation in acene-polymer blends.[32-42] Secondary ion mass spectroscopy (SIMS) has been adopted in this study for examining the structural formation of the TIPS/P4MS thin-film. Local caesium (Cs) ion sputtering of the TIPS/P4MS active-blend layer was used to remove material from the film with the resulting ejected ion species measured by a quadrapole mass spectrometer. The secondary ions of Si^-

were used as a marker for the detection of the silyl group associated with TIPS-pentacene. Due to the P4MS consisting primarily of carbon, detection of isotopes associated with this material was difficult to achieve.

SIMS was conducted on both 4-FTP and PFBT modified surfaces under post-treatment steps of 'rinsed' and 'annealed' substrates, shown in **Fig.4.13**. Associated with all the samples, the Si^- signal from TIPS-pentacene was initially detected showing localised TIPS-pentacene at the air-interface. Comparisons between the Si^- ion distributions for all scans are slightly different when considering the point in which the Si^- signal decays. The broadening of the Si^- signal is due to beam induced segregation of the TIPS-pentacene molecules by the impinging beam and is treated as an artefact. The slight irregular features of the Si^- signal for the PFBT annealed sample (see **Fig.4.13(d)**) may be due to non-uniformity in the active-blend layer. This correlates with the AFM micrograph which displayed voids within the thin-film (see **Fig.4.12(d)**). The sharp decay of the Si^- signal seen for all samples apart from PFBT rinsed (see **Fig.4.13(c)**) may be indicative of better interfacial properties of the blend layer at the electrode/OSC interface. The plateau region of the Si^- signal indicates even distribution of the TIPS-pentacene throughout the layer.

As the signal from the Au surface increases, the Si^- signal decays but begins to rise once the metal has been removed, exposing the glass substrate underneath. The reduction in the Si^- signal between the two Si^- maxima's has been described as being caused by a separation in the film due to a coexisting layer or predominant polymer matrix layer being present, indicating a tri-layer formation.[11] It is quite apparent that this is not the case in these findings due to the detection of the fluorinated thiol (associated with the SAM) and Au (electrode region) prior to the appearance of the second Si^- peak. Charge compensation using a flood gun was

conducted to maintain the detection of the glass substrate for clarification that the Si^- signal originated from the underlying substrate. As all signals drop-off due to all layers being penetrated, the Si^- signal remains indicating the glass substrate has been reached.

It is clear from the AFM and surface energy studies previously discussed that the TIPS-pentacene, when formulated as an active-blend, becomes localised at the air-interface with the P4MS binder residing below, when spin-coated on both PFBT and 4-FTP modified Au electrodes. The SIMS results are inconclusive in showing any structural layering of the active-blend thin-film, but may imply the P4MS coexist within the film below this top-layer of TIPS-pentacene.

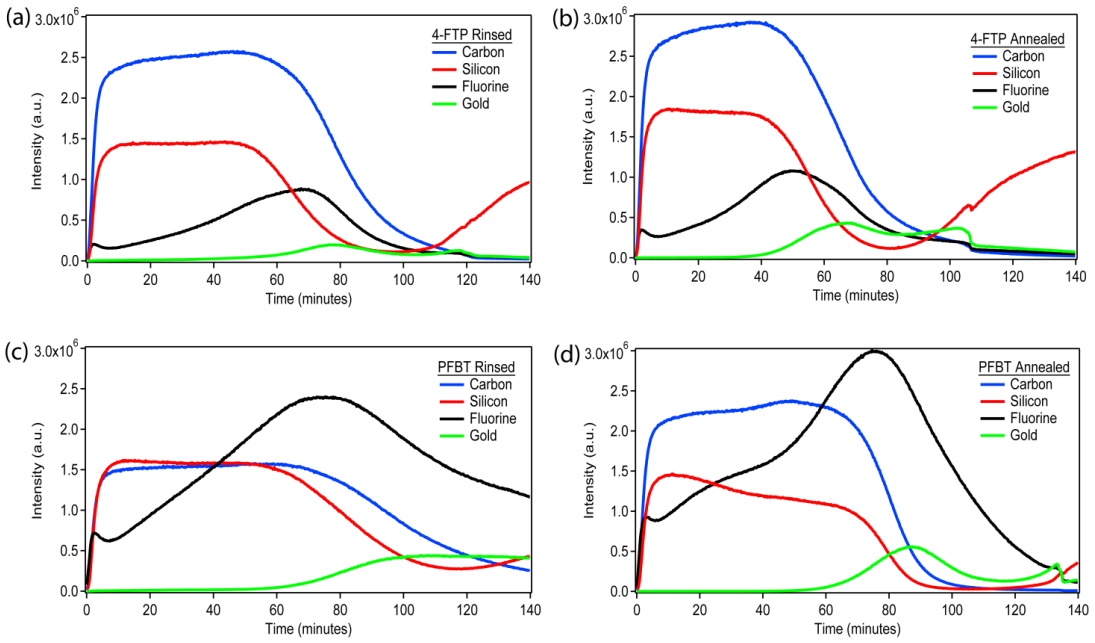

Figure 4.13: Time dependent SIMS response for TIPS/P4MS thin-films on 4-FTP and PFBT modified Au surface (a) 4-FTP Rinsed, (b) 4-FTP annealed, (c) PFBT rinsed, (d) PFBT annealed.

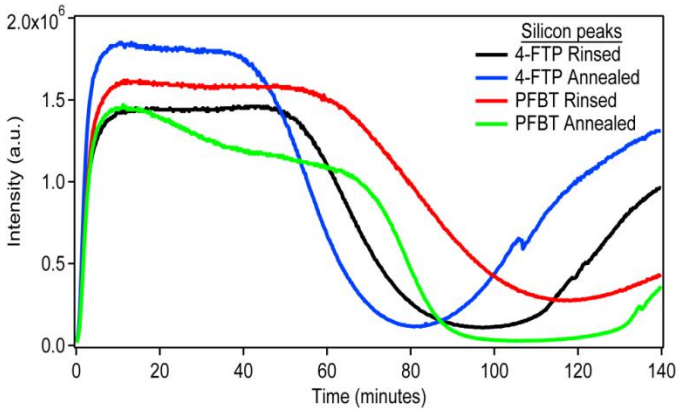

Figure 4.14: Time dependent SIMS response from Si^- signal for all samples.

The broadening in the signal peaks (for Au and fluorine) are due to a combination of variations in the etching rate for each material within the layer and a slight spread in the energy density of the Cs ion beam. The early detection of the fluorine and Au signals may be due to porous regions within the blend. This is highly apparent in the case of PFBT where the fluorine counts are much higher. The initial detection of both fluorine and Au before their respective maxima's is due to the porosity of the layer with both regions of the structure being faintly detected. As the surface of the layer is reached, a peak maximum is formed where a steady reduction in the peak occurs due to the layer being driven into the material below due to the beam.

4.2.8 Raman Mapping of TIPS/P4MS Thin-Films

An underutilised technique for studying topological features of organic semiconductors is Raman spectroscopy. This technique is non-invasive and non-destructive to the sample and capable of 2D mapping profiles of surfaces. Polarized Raman spectroscopy of TIPS-pentacene/polystyrene blends has been investigated in

literature showing its ability to map local changes in molecular structure of the active-blend layer.[43] This research conducted by James *et al.* characterised the local molecular order and orientation of TIPS-pentacene thin-films through angle-dependent analysis, concluding improvements in uniformity and coverage of the active-blend layer correlate with enhanced field-effect mobility.[43]

The Raman modes associated to TIPS-pentacene between 1100 cm^{-1} and 1700 cm^{-1} (see **Fig.4.15**) are from vibrations within the pentacene backbone, and not from the bulky side groups. The peaks in the region between 1140 and 1190 cm^{-1} have been assigned to the in-plane C-H bending mode (from the ends and sides of the pentacene back-bone), whereas the region between 1340 and 1420 cm^{-1} is associated with the C-C aromatic stretching mode, and the peak at 1598 cm^{-1} is assigned to the quadrant stretching mode.[44]. All observed Raman modes in the work were assigned based on quantum calculation by James *et al*.[43] The relative intensity ratio (I_{1158}/I_{1374}) between the C-H bending mode at 1158 cm^{-1} and the C-C ring stretching vibration at 1374 cm^{-1} can be used to characterise the lattice packing variation in the TIPS-pentacene film. According to previous Raman studies on pentacene, an increased intensity of the C-H bending mode at 1158 cm^{-1} implies increased motions (or degrees of freedom) of the H-atoms at the end of the conjugated core for a non-equilibrium film.[45,46]

The result was investigated in the TIPS/P4MS active-blend for devices prepared using 4-FTP after post-treatment rinsing and annealing of the substrate. The Raman map associated with the 4-FTP annealed substrate is shown in **Fig.4.16(a)**. When studying the TIPS-pentacene film formed on Au, a strongly enhanced Raman signal is detected due to the optical enhancement caused by the reflection of laser light from the Au, whereas the signal is significantly diminished within the channel

region due to the formation on glass. Studying the I_{1157}/I_{1374} ratio for the high intensity regions (red pixels) gave a high value of 0.94 (see **Fig.4.16(b)**), where the

(a)

Wavenumber (cm^{-1})	Mode Assignment
1158	C-H bending (ends)
1194	C-H bending (sides)
1374	C-C ring stretch (short axis)
1578	C-C ring stretch (long axis)

(b)

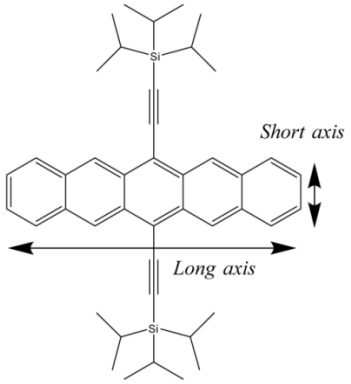

Figure 4.15: (a) Raman mode assignments for the four predominant peaks, and (b) TIPS-pentacene chemical structure.

low intensity regions (black pixels) gave a value of 0.85 (see **Fig.4.19(c)**). An average value for all intensities was taken over a minimum of five pixels. The I_{1157}/I_{1374} ratios are closely matched where it may be inferred that the molecular packing of the active-blend layer has a good degree of uniformity indicating a smaller extent of lattice deviation. The C-C ring stretching mode at 1374 cm^{-1} has been reported in literature as the most dominant peak, although in this work the strongest peak intensity occurred at 1548 cm^{-1} in both pixel defined regions.[43] We are unable to speculate over the cause of this large intensity which is commonly reported as being of a much lower signal. This strongly indicates differences in packing of TIPS-pentacene compared to reports in literature.

The Raman map of 4-FTP rinsed substrate is displayed in **Fig.4.17(a)**. The map shows much larger crystal domains represented by continuous regions of red and black pixels. The I_{1157}/I_{1374} ratio for the high intensity regions (red pixels) is 0.98, whereas for the lower intensity regions (black pixels) it is 0.67. The high intensity

regions have a slightly larger I_{1157}/I_{1374} ratio value compared with the 4-FTP annealed substrate, although the lower intensity areas have a significantly smaller I_{1157}/I_{1374}

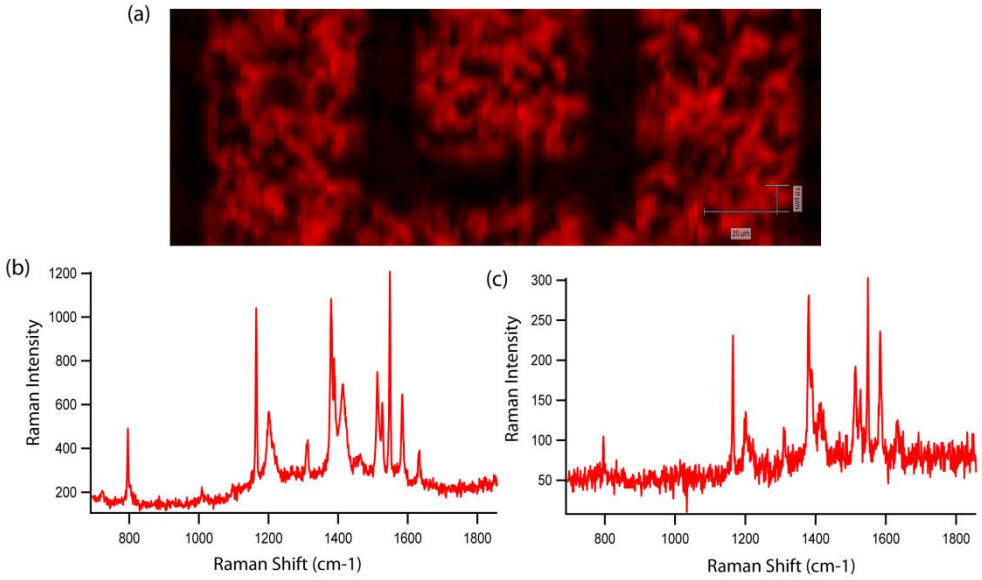

Figure 4.16: (a) Raman map of TIPS/P4MS active-blend layer formed across the electrode and channel region of 4-FTP annealed (140 °C) substrates, (b) Raman spectrum of region with high intensity (red pixels), (c) Raman spectrum of region with low intensity (black pixels). The peak intensity at 1374 cm^{-1} was used to construct the 2D map profile.

ratio which implies a more substantial deviation in the packing between these regions. Such variations may correlate with the lower field-effect mobility associated with this type of morphology. The peak at 1548 cm^{-1}, observed for the annealed substrate, is reduced substantial within the black pixel regions becoming much weaker in intensity relative to 1374 cm^{-1}, with the strongest peak assignment occurring at 1584 cm^{-1}. This highlights a change in the molecular packing between both pixel regions which may be associated to polymorphs of TIPS-pentacene which may correlate with the lower charge-carrier mobility associated with this type of morphology.

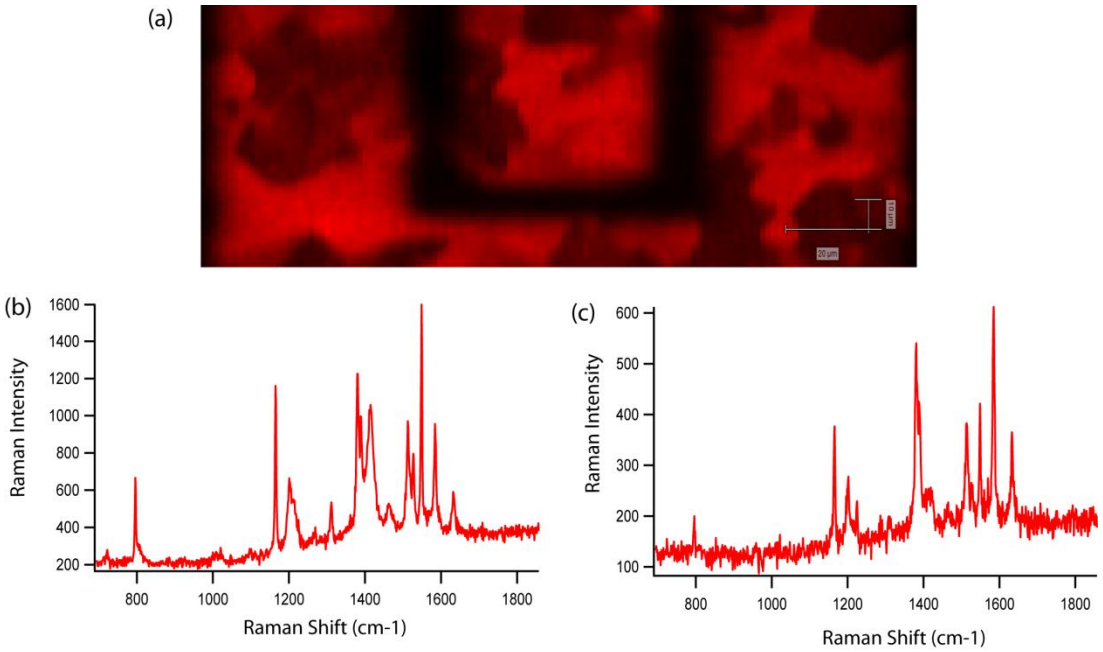

Figure 4.17: (a) Raman map of TIPS/P4MS active-blend layer formed across the electrode and channel region of the device for 4-FTP rinsed substrates, (b) Raman spectrum of regions with high intensity (red area), (c) Raman spectrum of region with low intensity (black area). The peak intensity at 1374 cm^{-1} was used to construct the 2D map profile.

4.2.9 Staggered vs. Planar Device Architectures

Staggered transistors commonly exhibit higher OTFT performance (i.e. higher effective mobilities), while planar devices usually display non-linear characteristics with much lower field-effect mobilities.[49-51] Staggered structures are known to surpass planar configurations in terms of injection efficiency due to the spreading of the gate-effect, where the accumulated regions extends beyond the projection of the gate onto the semiconductor/dielectric interface plane.[52,53] Charge injection is favoured by current crowding effects in staggered configurations.[47] Charge carriers are injected from the top surface of the contact, where the surface

area of the electrode can be significantly large. The devices used in this study have a large overlap of the gate electrode with the source/drain electrode. By doing so, contacts with low injection efficiency per unit area, or conductive pathways from the contact to the accumulated channel with high resistivity, can be compensated for such losses by this approach.[52] This leads to charge-barrier heights at the electrode/organic semiconductor interface being less sensitive compared with planar architectures.[53-56]

Devices were studied using different thiol treatment for rinsed and annealed post-treatment steps, and investigated in both BG/BC and TG/BC devices architectures. The peak saturation mobility for each device is plotted in **Fig.4.18**, with the corresponding I-V curves presented in **Fig.4.19** for TG/BC devices, and in **Fig.4.20** for BG/BC devices, with device parameters tabulated in **Table 4.5** and **Table 4.6**, respectively.

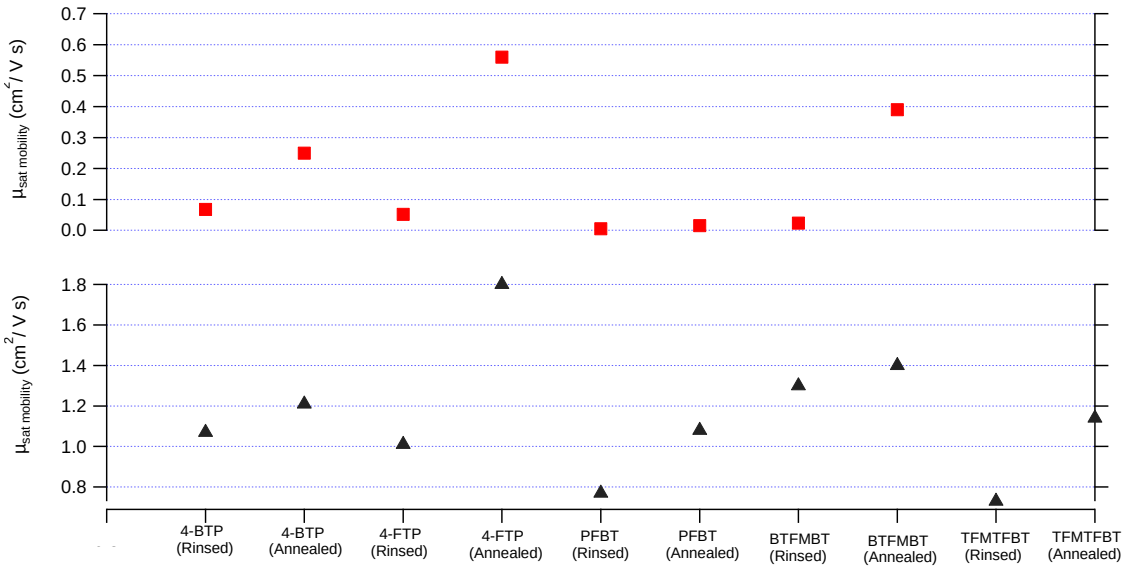

Figure 4.18: Summary of saturation mobility (peak values) for BG/BC (top graph) and TG/BC (bottom graph) devices.

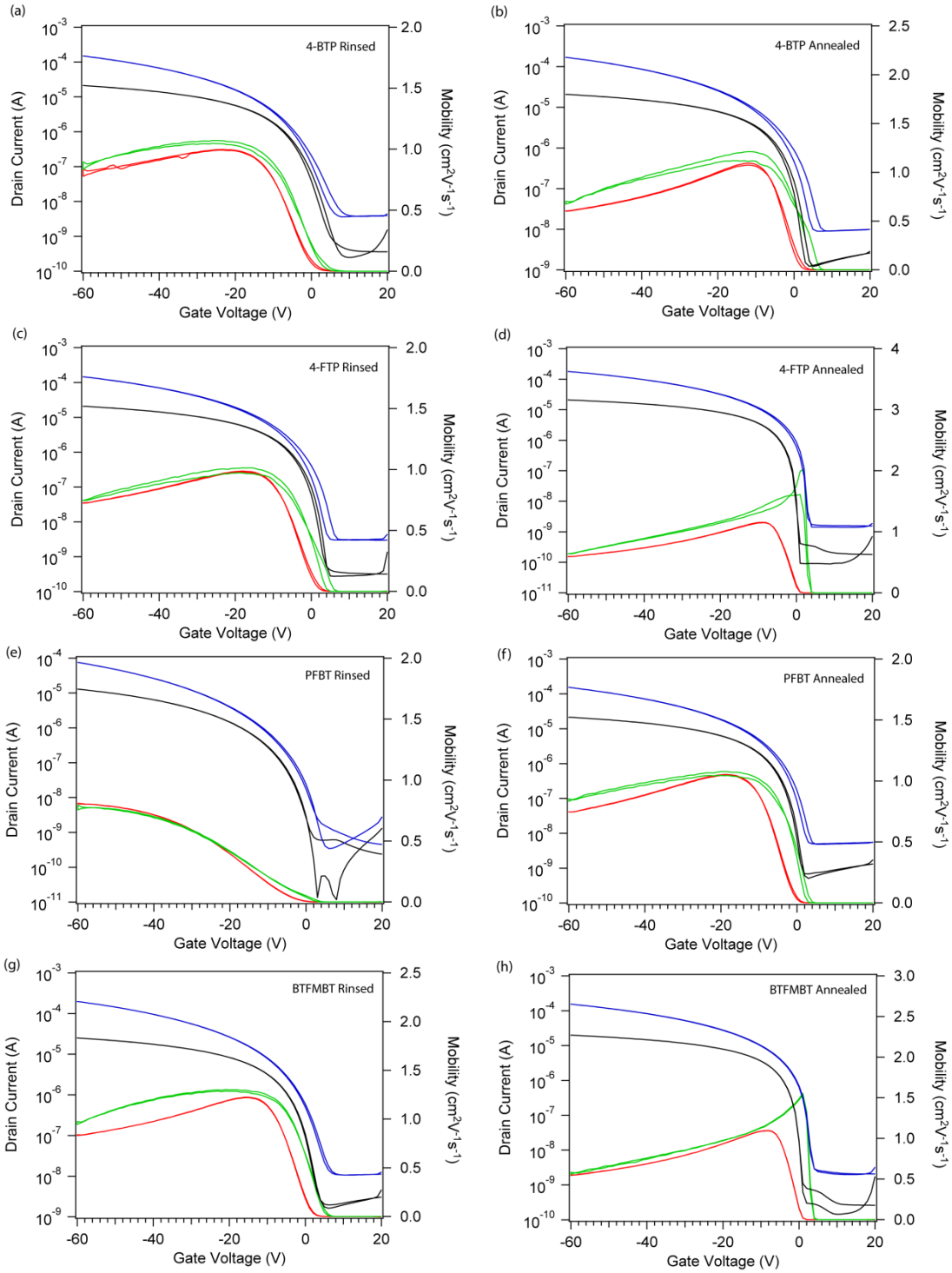
(a)
4-BTP Rinsed
(b)
4-BTP Annealed
(c)
4-FTP Rinsed
(d)
4-FTP Annealed
(e)
PFBT Rinsed
(f)
PFBT Annealed
(g)
BTFMBT Rinsed
(h)
BTFMBT Annealed
Drain Current (A)
Mobility (cm²V⁻¹s⁻¹)
Gate Voltage (V)

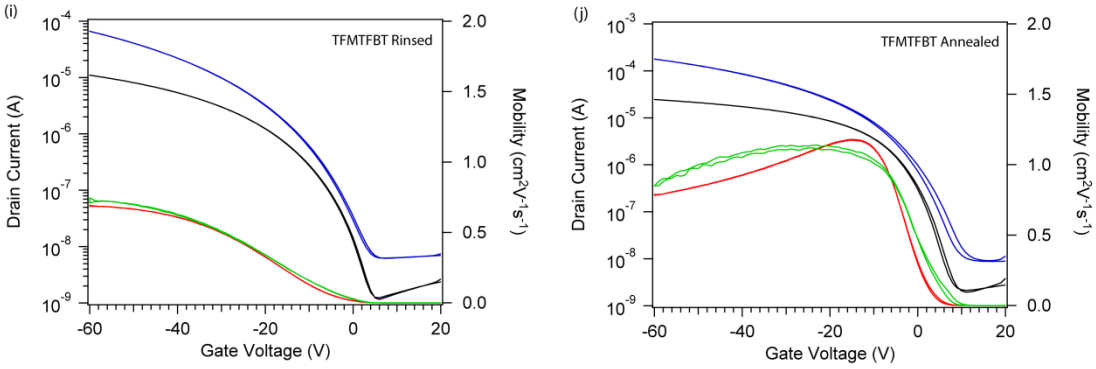

Fig.4.19. Device performance (L = 20 μm) of TIPS/P4MS active-blend layer with different SAM treatments in TG/BC.

Table 4.5: Summary of TG/BC devices investigated with range of SAMs. Samples stated as annealed were heated at 140 °C for 1 minute under atmospheric conditions.

Sample	μ_{lin}	μ_{sat}	$I_{on/off}$	S_{lin}	S_{sat}	V_T	V_{on}
4-BTP (Rinsed)	0.99	1.07	10^4	2.73	4.22	1	6
4-BTP (Annealed)	1.09	1.21	10^4	1.74	2.62	4	4
4-FTP (Rinsed)	0.99	1.01	10^4	1.39	2.32	4	4
4-FTP (Annealed)	1.15	2.03	10^5	0.65	1.02	6	1
PFBT (Rinsed)	0.81	0.79	10^5	1.11	2.29	-1	3
PFBT (Annealed)	1.05	1.08	10^4	1.53	2.33	2	2
BTFMBT (Rinsed)	1.22	1.33	10^4	2.2	3.45	3	5
BTFMBT (Annealed)	1.10	1.55	104	0.87	1.29	4	2
TFMTFBT (Rinsed)	0.69	0.75	104	4.04	5.97	-5	5
TFMTFBT (Annealed)	1.18	1.14	104	3.34	4.65	4	10

All devices prepared by annealing of the SAM modified electrode at 140 °C typically displayed the highest saturation mobility, with temperatures within ± 10 °C occasionally producing higher values when comparing between batches. Additionally, the sharp rise in saturation mobility for 4-FTP and BTFMBT annealed devices was observed in both TG/BC and BG/BC devices, producing the two of the largest peak mobilities of all OTFTs investigated. Additionally, the substhreshold

swing for these devices was very good in both device configurations, with values < 1 V/dec for linear regime measurements. The sudden increase in the saturation mobility which lowered with increasing gate voltage was a reproducible feature of these devices. Strong birefringence in the active-blend was observed by optical microscopy for the BTFMBT functionalised devices after post-treatment annealing, similar to that shown for 4-FTP in **Fig.4.10(d)**. Closer inspection of the BTFMBT morphology by AFM, shown in **Fig.4.22**, displayed similar grain structuring to that of 4-FTP as shown previously in **Fig.4.9** within the channel region of the device.

The birefringence observed for these devices could be associated with the degree of phase segregation within the thin-film during spin-coating. The surface energy of the substrate (i.e. electrode and glass regions) onto which the active-blend is deposited can impart a significant influence on the phase segregation between the small molecule and polymer binder. Phase separation which results in a mixed phase with poor molecular ordering of the small molecule can directly translate to lower charge-carrier mobility. Due to the relatively non-polar nature of TIPS pentacene, a higher polar component associated with the substrate is known to increase the amount of vertical phase separation due to dipolar interactions between the binder and the substrate. The largest polar constituent, as concluded from surface energy measurements discussed in **Chapter 3**, were associated with 4-FTP and PFBT. Consistently higher polar components > 2.0 mN/m were measured for these SAMs before and after annealing, with respect to other thiols investigated. Additionally, a high polar component was measured for BTFMBT modified electrodes after annealing at 140 °C (see **Table 3.5**). It is postulated that the larger polar constituent of the surface may relate directly to the associated high saturation mobility for 4-FTP

and BTFMBT annealed OTFTs, although such small increases in the polar

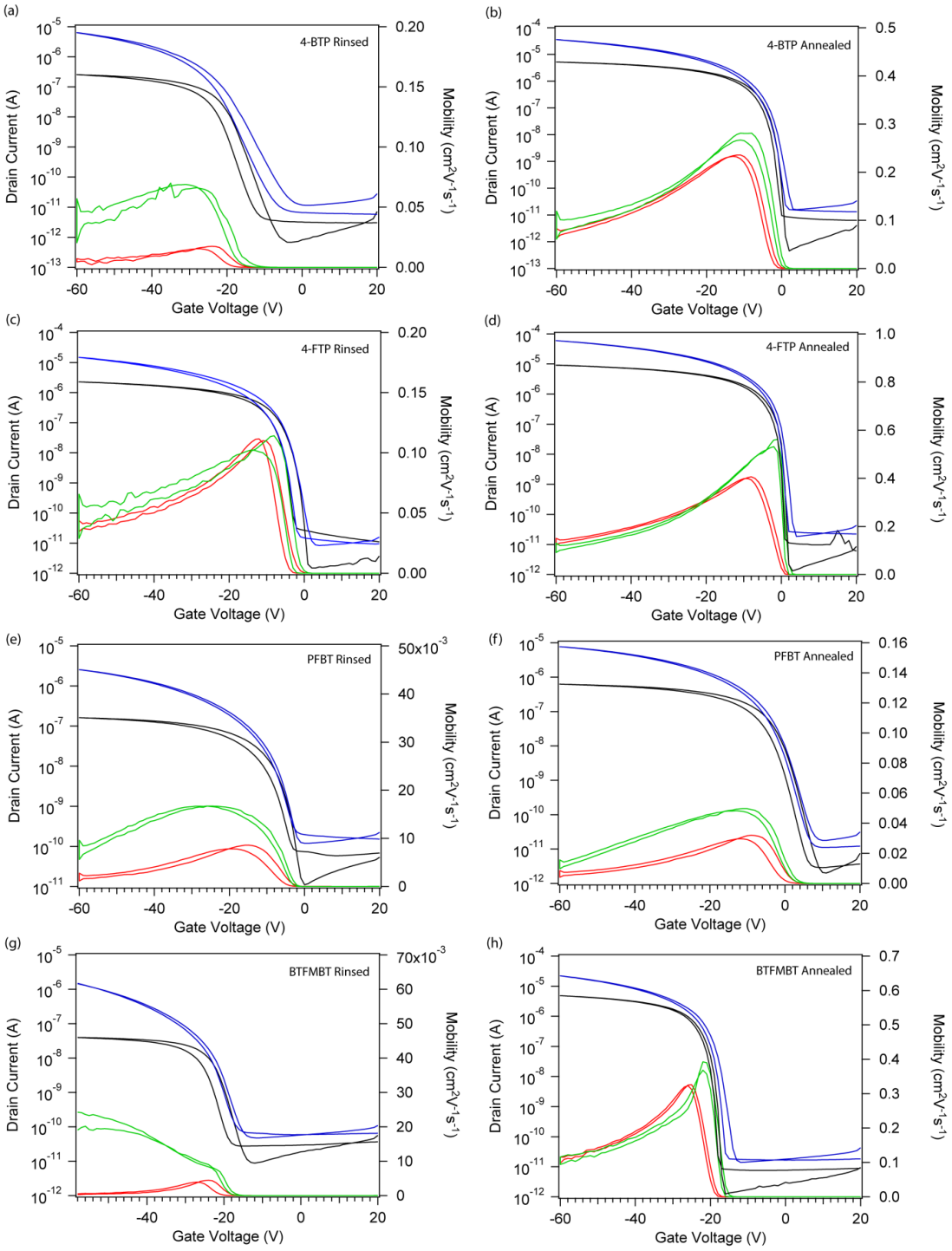

Fig.4.20: Device performance (L = 20 μm) of TIPS/P4MS active-blend layer with different SAM treatments in BG/BC.

Table 4.6: Summary of BG/BC devices investigated with range of SAMs. Samples stated as annealed were heated at 140 °C for 1 minute under atmospheric conditions.

Sample	μ_{lin}	μ_{sat}	$I_{on/off}$	S_{lin}	S_{sat}	V_T	V_{on}
4-BTP (Rinsed)	0.017	0.070	10^6	2.89	4.04	2	-8
4-BTP (Annealed)	0.236	0.281	10^6	0.64	1.27	-1	1
4-FTP (Rinsed)	0.119	0.110	10^6	0.71	1.47	-2	0
4-FTP (Annealed)	0.406	0.562	10^6	0.5	0.85	2	2
PFBT (Rinsed)	0.009	0.017	10^6	1.72	2.62	4	-1
PFBT (Annealed)	0.032	0.050	10^5	2.29	2.59	0	8
BTFMBT (Rinsed)	0.004	0.052	10^4	2.51	2.95	-2	-17
BTFMBT (Annealed)	0.326	0.393	10^6	0.61	1.19	3	-16

component may not have such a major influence on phase segregation in this instance. Annealing of the thiol-modified electrodes clearly indicates changes in surface energy properties in all cases, although disentangling influences on charge-carrier mobility between changes at the electrode and the active-blend layer is challenging.

The effects of the SAMs investigated on the measured hole-injection current display little influence from changes in the associated work function measured in **Chapter 3**. The systematic changes in source/drain work function cannot be easily explained in terms of modification of the energy barrier at the injecting source electrode. The energy barrier for hole-injection is undoubtedly reduced by using a higher work function, although disorder at this interface limits explaining this observed behaviour through thermionic emission, where a linear change in the charge-carrier barrier is expected to yield an exponential change in the injecting current.[57] Disorder at this interface weakens this dependence due to the availability of transport states in the tail of the DOS distribution, but a relatively strong

dependence is still expected for large charge-barrier heights.[58,59] The work function

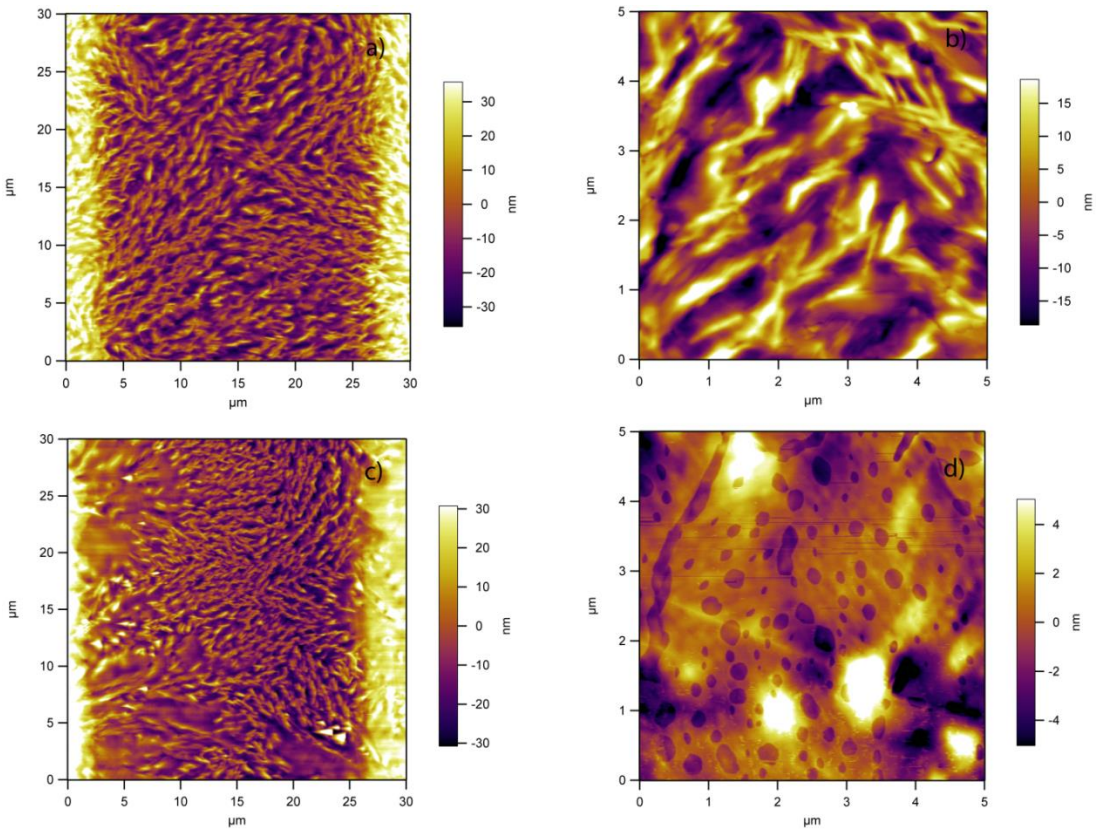

Figure 4.21: AFM micrographs of TIPS/P4MS with BTFMBT functionalised Au electrodes. BTFMBT rinsed (a, b) and annealed (c, d) devices with morphology within the channel region and on the electrode surface, respectively.

of all organothiols used should be aligned with or above the expected HOMO level for TIPS-pentacene, although the extent of the interfacial dipole barrier (discussed in **Chapter 3**) for each thiol formed at the electrode/OSC interface may have an overriding influence on the device performance. This interfacial dipole barrier was measured for TIPS/P4MS prepared on PFBT and 4-FTP modified electrodes by UPS, displaying a large charge-injection barrier present at both interfaces. It must be noted that this was only measured at the surface of the bulk sample and interfacial changes within the first few nanometres of the organic semiconductor were not

investigated due to the difficulty in controlling the thickness by spin-coating from solution. The measured HOMO levels of the OSC should only be used as an estimate and may not represent the true energetics at the metal/OSC interface when considered independently.

The device performance of 4-FTP modified electrodes annealed at temperatures just above 140 °C display a reduction in the charge-carrier mobility after the peak saturation mobility measured at this temperature. Post-treatment annealing of the 4-FTP functionalised electrodes at temperatures of 200 °C showed no severe degradation in device performance (see **Fig.4.22**), although mobility values do continue to drop (see **Table 4.7**). Annealing temperature of 200 °C have shown to remove detectable amounts of the thiol when measured using Raman spectroscopy and Kelvin Probe as discussed in **Chapter 3**, although it is plausible that small traces of the thiol are still present on the source/drain contacts which lead to the device performance shown in **Fig.4.22(d)**. These results highlight the importance of annealing the electrode after SAM treatment but an optimum performance window is seen at temperatures close to 140 °C.

Table 4.7: Summary of device parameters from I-V curves in Fig.4.22.

Sample	μ_{lin}	μ_{sat}	$I_{on/off}$	S_{lin}	S_{sat}	V_T	V_{on}
4-FTP (Rinsed)	0.99	1.01	10^4	1.39	2.32	4	4
4-FTP 100 °C	1.34	1.51	10^4	1.15	2.49	1	2
4-FTP 140 °C	1.15	2.03	10^5	0.65	1.02	6	1
4-FTP 170 °C	1.01	1.67	10^5	0.72	1.07	5	3
4-FTP 200 °C	0.80	1.01	10^4	0.75	1.09	2	2

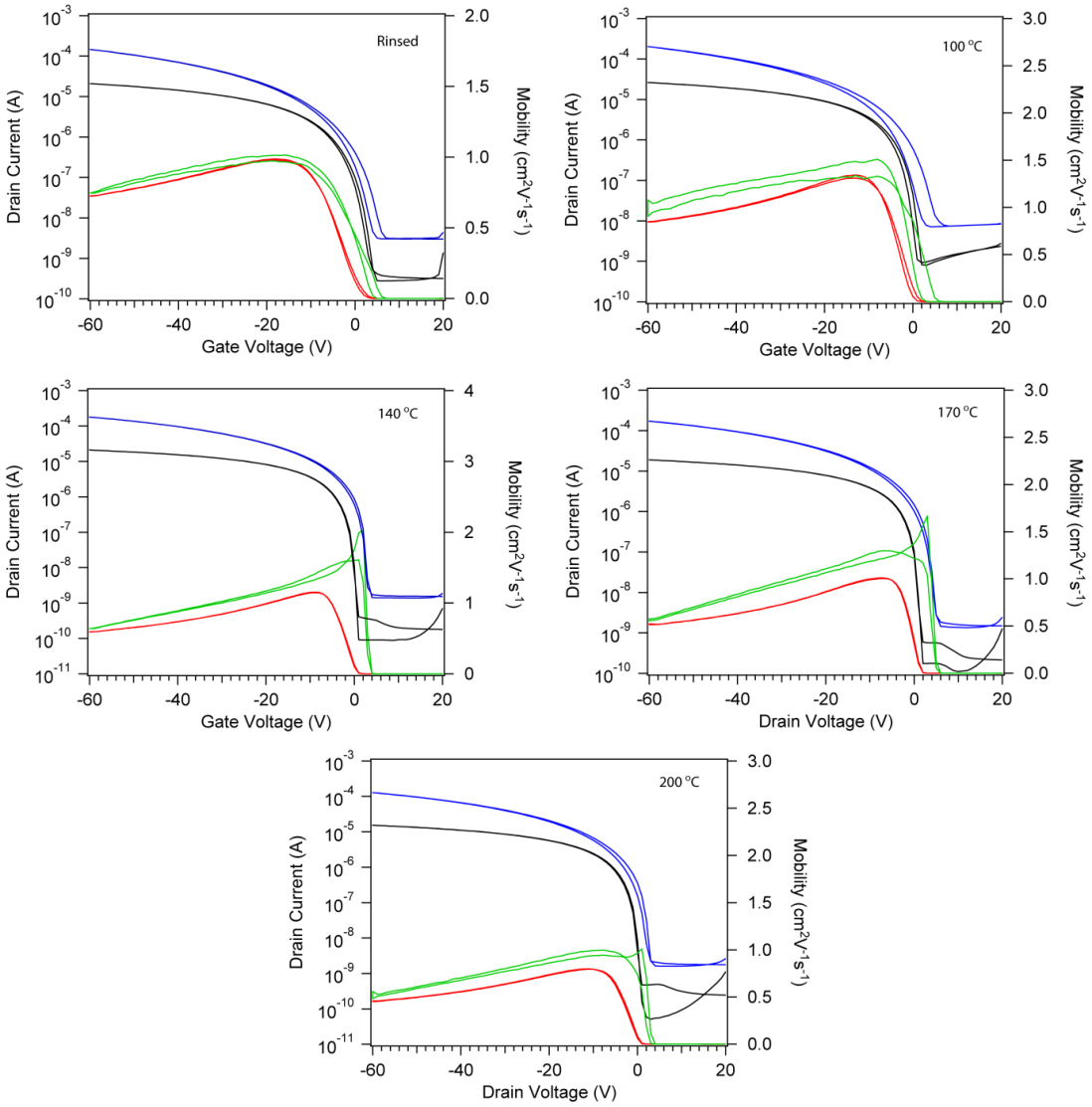

Figure 4.22: I-V performance of 4-FTP functionalised devices with varied annealing treatments.

4.3 Conclusion

This work has shown a significant improvement in I-V device characteristics in all cases when the SAM treated electrode is post-annealed for 1 minute over a temperature range of 100 – 200 °C. This enhancement is attributed to changes in surface energy of the source/drain electrode which improves the conductive

pathways for charge carriers through the OSC. Changes in the morphology of the active-layer after post-treatment annealing of the substrate was observed, although correlating changes in topography to device performance is challenging. This requires distinguishing between the thin-film and bulk properties, specifically the morphology adjacent to the contacts and gate-dielectric, alongside disentangle effects from charge-injection between the metal work function and OSC frontier molecular orbital. Similar behaviour in device characteristics of 4-FTP and BTFMBT modified contacts was seen before and after post-treatment annealing. These devices produced the highest measured mobility of all and similarly matched morphological features, indicating better compatibility between the SAM modified electrodes and the active-layer.

4.4 References

[1] Y.-Y. Lin, D. J. Gundlach, S. F. Nelson, T. N. Jackson. *IEEE Electron Device Letters*, (1997) *18*, 606.

[2] C. D. Dimitrakopoulos, A. R. Brown, A. Pomp, *J. Appl. Phys*., (1996) **80**, 2501.

[3] I. Kymissis, *Organic Field Effect Transistors*. (2009) Springer, 1st Edition, Pg.34-35.

[4] S. Steudel, S. D. Vusser, S. D. Jonge, D. Janseen, S. Verlaak, J. Genoe, P. Heremens, *Appl. Phys. Lett*., (2004) **85**, 19.

[5] J. E. Anthony, *Chem. Rev*., (2006) **106**, 5028.

[6] O. D. Jurchescu, D. A. Mourey, S. Subramanian, S. R. Parkin, B. M. Vogel, J. E. Anthony, T. N. Jackson, D. J. Gundlach. *Phys. Rev. B*, (2009) **80**, 085201.

[7] Y. Zheng, D. Qi, N. Chandrasekhar, X. Gao, C. Troadec, A. T. S. Wee, *Langmuir*, (2007) **23**, 8336.

[8] K. Ihm, B. Kim, T.-H. Kang, K.-J. Kim, M. H. Joo, T. H. Kim, S. S. Yoon, S. Chung, *Appl. Phys. Lett*., (2006) **89**, 033504.

[9] D. H. Kim, Y. D. Park, Y. Jang, H. Yang, Y. H. Kim, J. I. Han, D. G. Moon, S. Park, T. Chang, C. Chang, M. Joo, C. Y. Ryu, K. Cho, *Adv. Funct. Mater*., (2005) **15**, 77.

[10] A. Afzali, C. D. Dimitrakopoulos, T. L. Breen, *J. Am. Chem. Soc*., (2002) **124**, 8812.

[11] J. Smith, R. Hamilton, I. McCulloch, N. Stingelin-Stutzmann, M. Heeney, D. D. C. Bradley, T. D. Anthopoulos, *J. Mater. Chem*., (2010) **20**, 2562.

[12] J.-F. Chang, B. Sun, D. W. Breiby, M. M. Nielsen, T. I. Sölling, M. Giles, I. McCulloch, H. Sirringhaus, *Chem. Mater*., (2004) **16**, 4772.

[13] S.-I. Shin, J.-H. Kwon, H. Kang, B.-K. Ju, *Semicond. Sci. Technol*., (2008) **23**, 085009.
[14] J. Kang, N. Shin, D. Y. Jang, V. M. Prabhu, D. Y. Yoon, *J. Am. Chem. Soc*., (2008) **130**, 12273.
[15] K. R. Sarma, C. Chanley, S. R. Dodd, J. Roush, J. Schmidt, G. Srdanov, M. Stevenson, R. Wessel, J. Innocenzo, G. Yu, M. B. O'Regan, W. A. MacDonald, R. Eveson, K. Long, H. Gleskova, S. Wagner, J. C. Strum. Proc. SPIE 5080, (2003) 180, doi:10.1117/12.497638
[16] J. E. Anthony, J. S. Brooks, D. L. Eaton, S. R. Parkin, *J. Am. Chem. Soc.*, (2001) **123**, 9482.
[17] D. Gupta, N. Jeon, S. Yoo, *Org. Electron*., (2008) 9, 1026.
[18] R. J. Chesterfield, J. C. McKeen, C. R. Newman, P. C. Ewbank, D. A. S. Filho, J.-L. Brédas, L. L. Miller, K. R. Mann, C. D. Frisbie, *J. Phys. Chem. B.* (2004) **108**, 19281.
[19] S. K. Park, T. N. Jackson, J. E. Anthony, D. A. Mourey, *Appl. Phys. Lett.*, (2007) **91**, 063514.
[20] N. Shin, J. Kang, L. J. Richter, V. M. Prabhu, R. J. Kline, D. A. Fischer, D. M. DeLongchamp, M. F. Toney, S. K. Satija, D. J. Gundlach, B. Purushothaman, J. E. Anthony, D. Y. Yoon, *Adv. Funct. Mater*., (2013) **23**, 366.
[21] J. Chen, C. K. Tee, M. Shtein, D. C. Martin, J. E. Anthony, *Org. Electron.*, (2009) **10**, 696.
[22] W. Kalb, P. Lang, M. Mottaghi, H. Aubin, G. Horowitz, M. Wuttig, *Synthetic Metals*, (2004) **146**, 279.
[23] M. Mottaghi, G. Horowitz, *Org. Electron*., (2006) **7**, 528-536.
[24] S. Grecu, M. Roggenbuck, A. Opitz, W. Brütting, *Org. Electron*., (2006) 7, 276.
[25] A. B. Naden, J. Loos, D. A. MacLaren, *J. Mater. Chem. C*, (2014) **2**, 245.
[26] Y. Su, L. Zheng, J. Liu, Y. Han, *RSC Adv*., (2013) **3**, 5529.
[27] W. H. Lee, D. Kwak, J. E. Anthony, H. S. Lee, H. H. Choi, D. H. Kim, S. G. Lee, K. Cho, *Adv. Funct. Mater*., (2012) **22**, 267.
[28] S. Locci, M. Morana, E. Origiu, A. Bonfiglio, P. Lugli, *IEEE Trans. Electron. Devices*, (2008) **55**, 2561.
[29] K. B. Burke, W. J. Belcher, L. Thomsen, B. Watts, C. R. McNeill, H. Ade, P. C. Dastoor, *Macromolecules*, (2009) **42**, 3098.
[30] L. Miozzo, A. Yassar, G. Horowitz, *J. Mater. Chem*., (2010) **20**, 2513.
[31] J. Chen, D. C. Martin, J. E. Anthony, *J. Mater. Res*., (2011) **22**, 1701.
[32] B. Park, H. G. Jeon, J. Choi, Y. K. Kim, J. Lim, J. Jung, S. Y. Cho, C. Lee, *J. Mater. Chem.*, (2012) **22**, 5641.
[33] J. Smith, R. Hamilton, I. McCulloch, M. Heeney, J. E. Anthony, D. D. C. Bradley, T. D. Anthopoulos, *Synthetic Metals*. (2009) **159**, 2365.
[34] S. Y. Cho. J. M. Ko, J.-Y. Jung, J. Y. Lee, D. H. Choi, C. Lee, *Org. Electron*., (2012) **13**, 1329.
[35] S. Y. Cho, J. M. Ko, J. Lim, J. Y. Lee, C. Lee, *J. Mater. Chem. C*, (2013) **1**, 914.
[36] R. Hamilton, J. Smith, S. Ogier, M. Heeney, J. E. Anthony, I. McCulloch, J. Veres, D. D. C. Bradley, T. D. Anthopoulos, *Adv. Mater*., (2009) **21**, 1166.
[37] Y. S. Chung, N. Shin, J. Kang, Y. Jo, V. M. Prabhu, S. K. Satija, R. J. Kline, D. M. DeLongchamp, M. F. Toney, M. A. Loth, B. Purushothaman, J. E. Anthony, D. Y. Yoon, *J. Am. Chem. Soc.*, (2011) **133**, 412.

[38] D. K. Hwang, C. Fuentes-Hernandez, J. D. Berrigan, Y. Fang, J. Kim, W. J. Potscavage Jr, H. Cheun, K. H. Sandhage, B. Kippelen, *J. Mater. Chem*., (2012) **22**, 5531.
[39] L. Qiu, J. A. Lim, X. Wang, W. H. Lee, M. Hwang, K. Cho, *Adv. Mater*., (2008) **20**, 1141.
[40] T. Ohe, M. Kuribayashi, R. Yasuda, A. Tsuboi, K. Nomoto, K. Satori, M. Itabashi, J. Kasahara, *Appl. Phys. Lett*. (2008) **93**, 053303.
[41] H. Zhong, J. Smith, S. Rossbauer, A. J. P. White, T. D. Anthopoulos, M. Heeney, *Adv. Mater*., (2012) **24**, 3205.
[42] J.-H. Kwon, S.-I. Shin, K.-H. Kim, M. J. Cho, K. N. Kim, D. H. Choi, B.-K. Ju, *Appl. Phys. Lett*., (2009) **94**, 013506.
[43] D. T. James, B. K. C. Kjellander, W. T. T. Smaal, G. H. Gelinck, C. Combe, I. McCullock, R. Wilson, J. H. Burroughes, D. D. C. Bradley, J.-S. Kim. *ACS Nano*., (2011) **5**, 9824.
[44] F. D. Angelis, G. Das, E. Di. Fabrizio, Chem. Phs. Lett., (2008) **462**, 234.
[45] H. L. Cheng, Y. S. Mai, W. Y. Chou, L. R. Chang, X. W. Liang, *Adv. Funct. Mater.*, (2007) **17**, 3639.
[46] J. Xu, Y. Diao, D. Zhou, Y. Mao, G. Giri, W. Chen, N. Liu, S. C. B Mannsfeld, G. Xue, Z. Bao. *J. Mater. Chem. C*, (2014) **2**, 2985.
[47] J. W. Ward, M. A. Loth, R. J. Kline, M. Coll, C. Ocal, J. E. Anthony, O. D. Jurchescu, *J. Mater. Chem*., (2012) **22**, 19047.
[48] K. L. McCall, S. R. Rutter, E. L. Bone, N. D. Forrest, J. S. Bissett, J. D. E. Jones, M. J. Simms, A. J. Page, R. Fisher, B. A. Brown, S. D. Ogier. *Adv. Funct. Mater*., (2014) **24**, 3067.
[49] H. Kang, N-S. Lee, E. Ito, M. Hara, J. Noh, *Langmuir*, (2010), **26**, 2983-2985.
[50] P. V. Persavento, K. P. Puntambekar, C. D. Frisbie, J. C. McKeen, P. P. Ruden, *J. Appl. Phys*., (2006) **99**, 094504.
[51] D. Gupta, M. Katiyar, D. Gupta, *Org. Electron*., (2009) **10**, 775.
[52] D. Natali, M. Caironi, *Adv. Mater*., (2012) **24**, 1.
[53] T. Li, J. W. Balk, P. P. Ruden, I. H. Campbell, D. L. Smith, *J. Appl. Phys*., (2002) **91**, 4312.
[54] C. H. Shim, F. Maruoka, R. Hattori, *IEEE Electron. Dev*., (2010) **57**, 195.
[55] S. Scheinert, G. Paasch, *J. Appl. Phys*., (2009) **105**, 014509.
[56] N. Tessler, Y. Roichman, *Appl. Phys. Lett*., (2001) **79**, 2987.
[57] P. Bröms, J. Birgersson, W. R. Salaneck, *Synthetic Metals*, (1997) **88**, 255.
[58] S. Khodabakhsh. (2005). *Use of Self-Assembled Monolayers in Organic Semiconductor Devices.* (2005) Ph.D. Thesis, Imperial College London, U.K.
[59] V. I. Arkhipov, U. Wolf, H. Bässler, *Phys. Rev. B*, (1999) **59**, 7514.

Chapter 5

Small Molecule/Polymer Binder Organic Thin-Film Transistors Utilising 2,8-difluoro-5,11-bis(triethylsilylethynyl)anthradithiophene

This chapter is a development of the work discussed in **Chapter 4** and adopts similar device fabrication methods as previously described for optimising the performance of 2,8-difluoro-5,11-bis(triethylsilylethynyl)anthradithiophene (diF-TES-ADT) in OTFTs. Active-blend thin-films are prepared through the use of P4MS with investigations into its morphology and its correlation with the substrate surface energy properties. Additionally, bias-stress behaviour of these OTFTs is studied and its direct effect on the I-V characteristics of the device when operated over several hours.

5.1 Introduction

5,11-Bis(triethylsilylethynyl) anthradithiophene (TES-ADT) is a soluble small molecule organic semiconductor widely investigated in OTFTs.[1] This compound has similar structural properties to TIPS-pentacene, relating to its pentacene-like backbone and bulky side groups. The consensus in expanding upon such oligomers is due to the good π-orbital coupling associated with conjugated acene-based semiconductors. Popular functionalised derivatives of TES-ADT are associated with halogenation (i.e, Br, Cl, F) of the thienyl at both sides of the conjugated backbone. Increased charge-carrier mobility has been associated for such derivatives in relation to TES-ADT, with single-crystal mobilities for the fluorinated derivative, diF-TES-ADT, displaying a hole mobilities of 6 cm^2/V s.[2] and between 0.5 – 1.5 cm^2/V s for thin-films.[3,4] The addition of fluorine to both thiophenes

changes the structural and electronic properties of the compound.[3] The electronegativity of fluorine causes the thiophene ring to become more electron-deficient and thus the electron affinity can be increased, which subsequently increases the ionisation level and subsequently the position of the HOMO. The intermolecular spacing between neighbouring compounds is assumed to decrease, due to increased electron affinity, leading to better π-stacking, where a spacing of 3.2 Å has been measured compared with 3.43 Å for TIPS-pentacene.[5] Mobility values of higher than 3 cm^2 $V^{-1}s^{-1}$ for diF-TES ADT have been quoted in toluene and chlorobenzene by drop-casting, due to the slow crystallising of the solute by this deposition method benefiting crystallisation.[5] Achieving such high mobility by deposition methods such as spin-coating which can be scalable for industrial processing is highly advantageous and will be discussed within this chapter. The device performance of diF-TES-ADT incorporated with a polymer binder has shown reproducible performance.[6-8] and work with other different bulky groups has shown improved solubility and alterations in crystal packing.[9] High mobility values of 5 cm^2 $V^{-1}s^{-1}$ processed from solution blended with the semiconducting polymer binder poly(dialkyl-fluorene-co-dimethyl-triarylamine) (PF-TAA) have been achieved setting a precedent for achieving high performance OTFTs through the adoption of small molecule/polymer blend systems.[10] The methodology used for device preparation in **Chapter 4** has been implemented for the work on diF-TES-ADT, drawing parallels between both systems.

5.2 Results and Discussion

5.2.1 I-V Characteristics of diF-TES-ADT

The OTFT performance for diF-TES-ADT blended with P4MS was investigated on 4-FTP functionalised electrodes due to heightened OTFT performance observed for TIPS-pentacene under similar processing conditions. The I-V characteristics for both 'rinsed' and 'annealed' (140 °C) electrodes displayed similar behavioural traits to that of TIPS-pentacene, where annealing causes increased mobility in the saturation regime and negative shifts in V_T. The device performance for this active layer material was investigated on both glass substrates (see **Fig.5.1**) and passivated glass substrates by a planarization layer (see **Fig.5.2**) which is of equivalence to a plastic substrate.

The I-V curve for 4-FTP rinsed devices shown in **Fig.5.1**(a) displayed good OTFT characteristics. The electrical behaviour of the device in the linear regime displays minimal hysteresis and minimal deviation in mobility between trace and retrace scans as shown in **Fig.5.1(c)**. When tested in the saturation regime heightened hysteresis is observed which presents positive shifts in the threshold

voltage occurring in the retrace curve. The saturation mobility is slightly lower than the linear mobility in this instance. Surprisingly, when the 4-FTP modified substrate is annealed at 140 ^{o}C, shown in **Fig.5.1(b)**, no significant variation in the linear regime is observed between the two devices, but when measured in the saturation regime an almost twofold increase in the charge-carrier mobility is observed, shown in **Fig.5.1(d)**. The shape of the saturation mobility curve displays similar profile traits in both devices indicating the same influence on charge-carrier mobility

repeatedly occurs but a more conductive channel is present in the case of 4-FTP annealed devices.

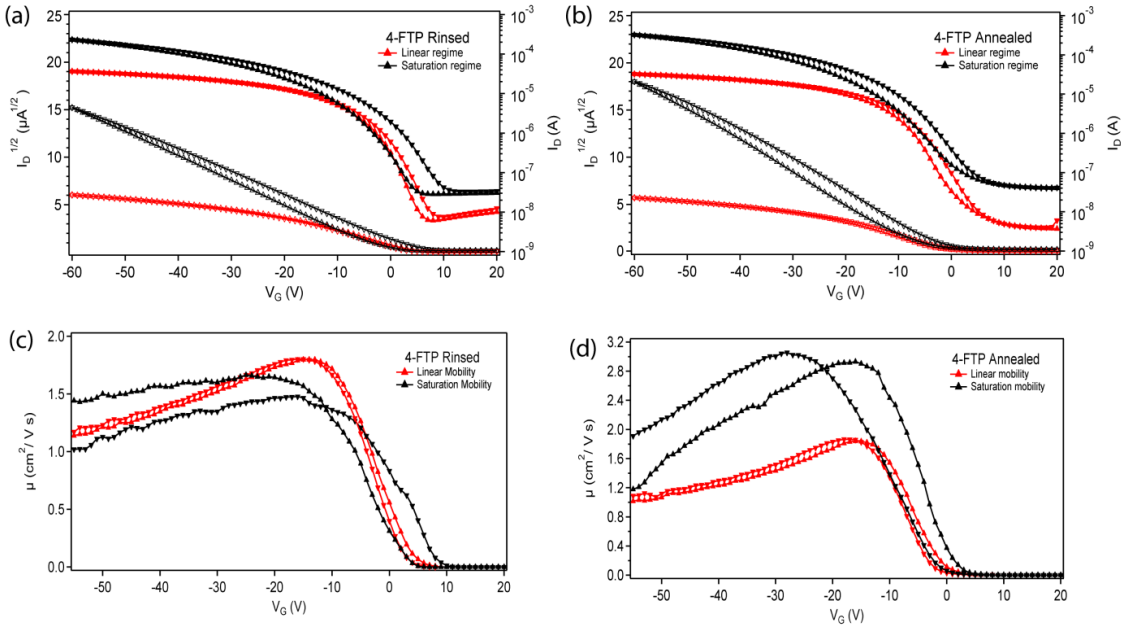

Figure 5.1: diF-TES-ADT device performance prepared on glass substrate. Au modified 4-FTP electrodes under rinsed and annealed conditions with respective (a, b) transfer curves and (c, d) mobility profiles. Device are in TG/BC configuration with L = 20 μm.

As a comparison, similar devices were prepared on glass substrates coated with a planarization layer which was spin-coated and UV cured. All other processing steps and layering were kept the same. **Fig.5.2** shows the I-V and mobility curves of 4-FTP 'rinsed' and 'annealed' devices. The 4-FTP rinsed devices, shown in **Fig.5.2(a)**, displayed significantly worse subthreshold behaviour with much higher threshold voltages, but did achieve lower I_{OFF} with turn-on voltages very close to zero. The overall mobility had significantly dropped displaying unstable behaviour in the saturation regime, requiring much large gate-voltages to induce charge-

carriers, shown in **Fig.5.2(c)**. Much better device performance was achieved by annealing the 4-FTP modified substrate, shown in **Fig.5.2(b)**, although the overall performance was still significantly poor, with mobilites < 1 cm^2 V^{-1} s^{-1} as shown in **Fig.5.2(d)**.

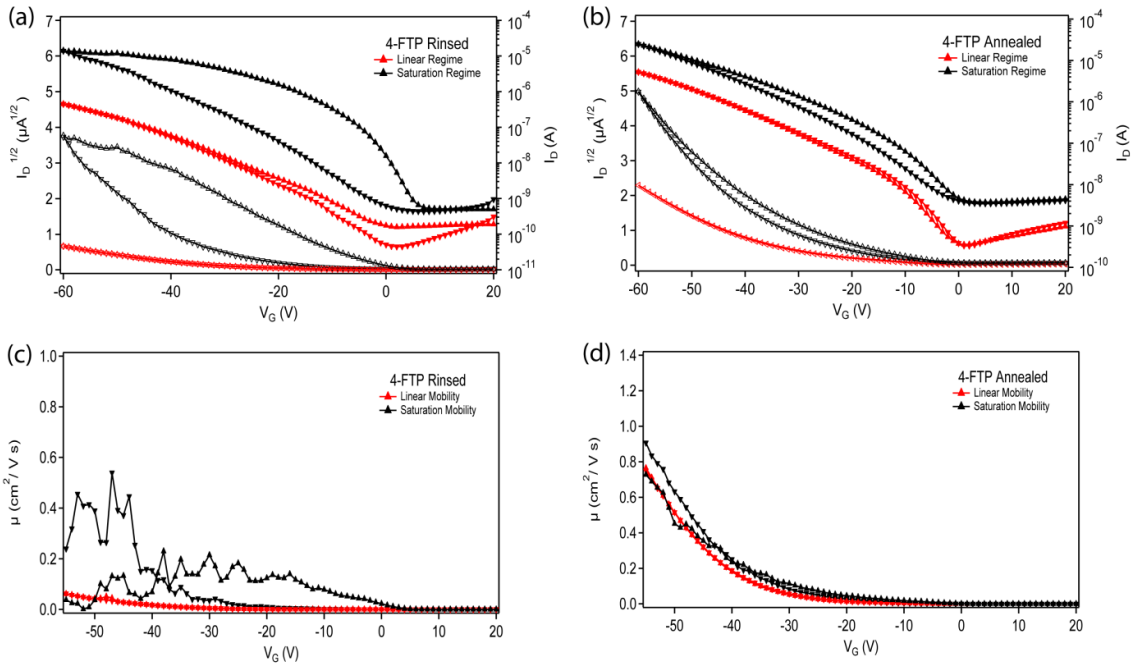

Figure 5.2: diF-TES-ADT device performance prepared on passivated (P014) glass substrate. Au modified 4-FTP electrodes under rinsed and annealed conditions with respective (a, b) transfer curves and (c, d) mobility profiles.

The device performance variation between the two different sets of OTFTs was investigated regarding the surface energy variations in the substrate and the morphology of the active layer. These results will now follow.

5.2.2 Correlation between Substrate Surface Energy and Device Performance

The surface energy values of the glass and passivated substrate are tabulated in **Table 5.1**. Variations in surface energy of both substrates was studied immediately after cleaning, rinsing with 4-FTP formulation, and then additional

annealing at 140 ^{o}C. Freshly cleaned glass was very hydrophilic with unmeasurable static-water contact angles which were < 5 degrees. After rinsing or subsequently annealing of the substrate the static-water contact angle increased to approximately 10 degrees indicating an uptake of contaminants onto the surface. Although such changes were observed the overall surface energy did not deviate. The surface energy of the passivated layer, which will be described as P014, presented a more hydrophobic surface concluded from the static-water contact angles in comparison to glass. The IFT of this substrate was much lower, presenting a more dispersive surface with a significantly lower polar constituent. The higher polar component associate to the glass surface compared to the passivated layer (P014) indicates a relative dependence between the polarity of the surface and device performance. By changing the surface energy of the substrate it has proved possible to alter the performance of the transistor even if this is not the interface at which charge accumulation occurs. This directly implies that a morphological change must be occurring which has a beneficial effect on charge-carrier mobility.

Table 5.1: Calculated surface energy values associated with the passivation layer (P014) and glass substrate. Samples were measured immediately after preparation (unmodified), after rinsing with 4-FTP (rinsed), and after an additional annealing step at 140 °C.

Sample	Water (°)	MI (°)	γ_D(mN/m)	γ_P (mN/m)	IFT (mN/m)
P014 (Unmodified)	71.48	35.39	37.96	5.83	43.81
P014 (Rinsed)	65.85	35.53	36.79	8.86	45.65
P014 (Annealed)	70.16	40.75	34.85	7.43	42.28
Glass (Unmodified)	< 5	41.48	27.30	45.25	72.55
Glass (Rinsed)	9.43	39.06	28.50	44.02	72.52
Glass (Annealed)	9.03	39.23	28.41	44.17	72.58

5.2.3 Topography Study of diF-TES-ADT

In the case of F-TES-ADT the microstructure of the thin-film is critically dependent on device performance. The formation of the microstructure of the OSC heavily impacts the device performance where grain boundaries, molecular ordering, molecular packing, and traps or defects sites can have a varied effect on device performance.

The morphology of diF-TES-ADT/P4MS thin-films for the devices prepared on glass are shown in **Fig.5.3**. Both 'rinsed' and 'annealed' device present contrastingly different topological features. The 'rinsed' surface presented

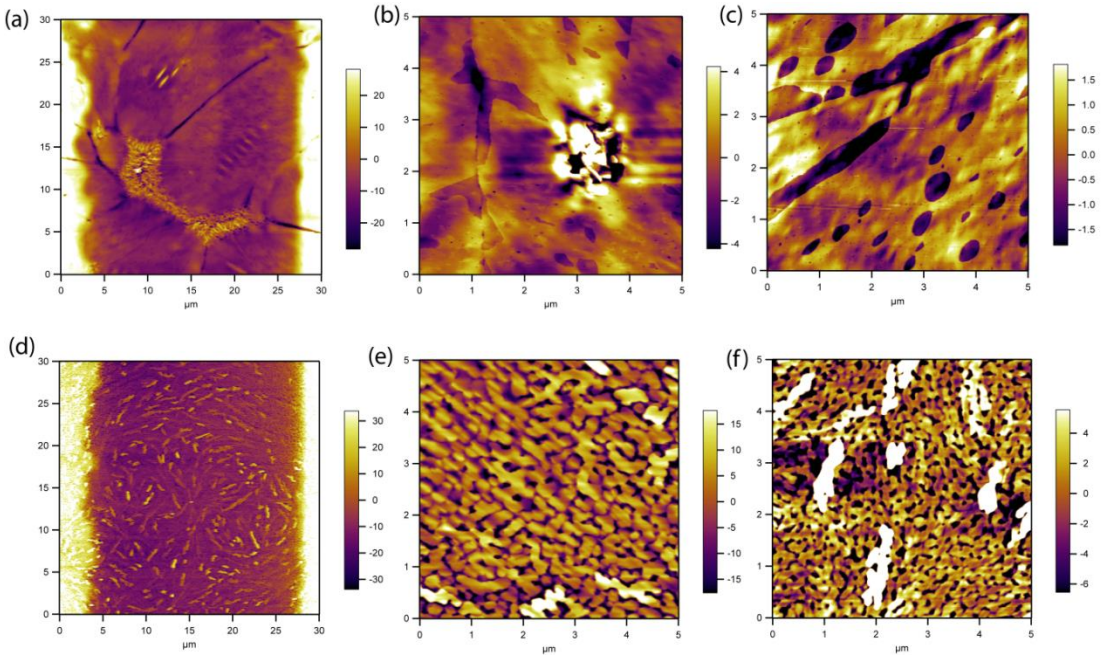

Figure 5.3: diF-TES-ADT topography for devices prepared on glass substrates. Morphology scans of (a,d) channel region, (b,e) Au electrode, (c,f) glass region within channel for 4-FTP rinsed and annealed devices, respectively.

significantly large crystals within the channel region (see **Fig.5.3(a)**). Similar crystal

growth appeared to be present on both the electrode surface (see **Fig.5.3(b)**) and on the glass substrate (see **Fig.5.3(c)**). As seen with the channel region for TIPS/P4MS thin-films prepared on PFBT annealed substrates (see **Fig.4.10(d)**), incomplete growth of the top layer of diF-TES-ADT is seen presenting voids within the layer (see **Fig.5.3(c)**). The morphology for 4-FTP annealed devices presents a much varied topography with significantly higher grain boundaries due to the presence of small grains, approximately 0.5 μm in length. The bulk of the thin-film may vary from the morphology observed at the air-interface which may relate to the enhanced charge-carrier mobility observed for this device.

The morphological features of diF-TES-ADT/P4MS thin-films on P014 passivated glass substrates are shown in **Fig.5.4**. In comparison to the varied morphology observed in **Fig.5.3** once again the thin-films display unique characteristic features related to this particular substrate. The topography for the 4-FTP rinsed substrates, shown in **Fig.5.3(a)**, display elongated needle-like structures which appear to protrude from the bulk. The morphology appears similarly matched on the electrode (see **Fig.5.3(b)**) and P014 substrate (see **Fig.5.3**(c)) displaying large grains and overlapping domains. A striking features is the parallel line structures present within the large domains which appear almost periodically ordered. This structural feature is even more pronounced for the 4-FTP annealed devices, shown in **Fig.5.3(e)**. A resemblance between the morphology of the two different preparations is more apparent in this instance as similar needle-like features are seen to dominate the topography. Although contradictory in its argument, the formation of small grains as seen in **Fig.5.3(e)** produces much better charge-carrier mobility which may result from better phase-segregation in the active layer, due to the increased polar

component of the glass and 4-FTP modified electrode when annealed.

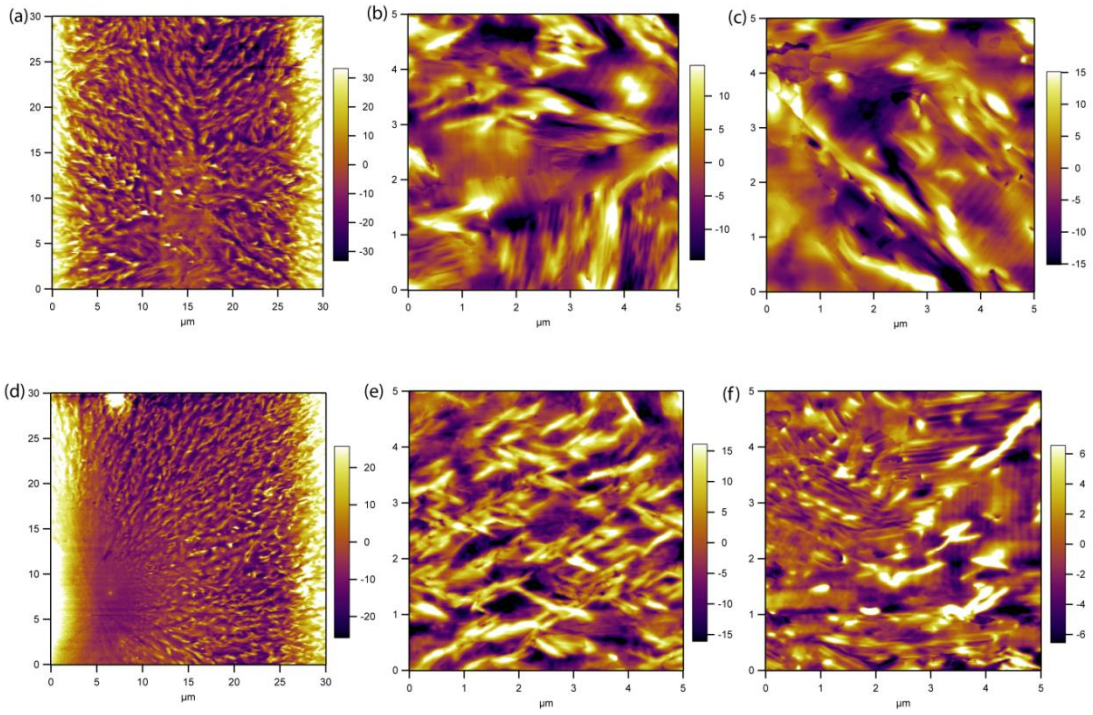

Figure 5.4: diF-TES-ADT topography for devices on passivated (P014) substrates. Morphology scans of (a,d) channel region, (b,e) Au electrode, (c,f) glass region within channel for 4-FTP rinsed and annealed devices, respectively.

5.2.4 XRD Study of diF-TES-ADT

The XRD diffractograms of diF-TES-ADT/P4MS thin-films prepared on 4-FTP 'rinsed' and 'annealed' glass substrates are shown in **Fig.5.5(a)** and **Fig.5.5(b)**, respectively. All characteristic diffraction peaks are present with particular spectral dominance from the 001 peak. A particularly strong intensity was measured for diF-TES-ADT/P4MS films prepared on 4-FTP rinsed (see **Fig.5.5(a)**) with all diffraction peaks being clearly distinguished with minimal noise present in the signal. The XRD spectrum for the 4-FTP annealed substrate (see **Fig.5.5(b)**) has increased noise in its signal with a lower relative intensity of the 001 peak. The 002, 003 and 004 peaks

appear to be lost in the high signal-to-noise, although very distinct 001 and 005

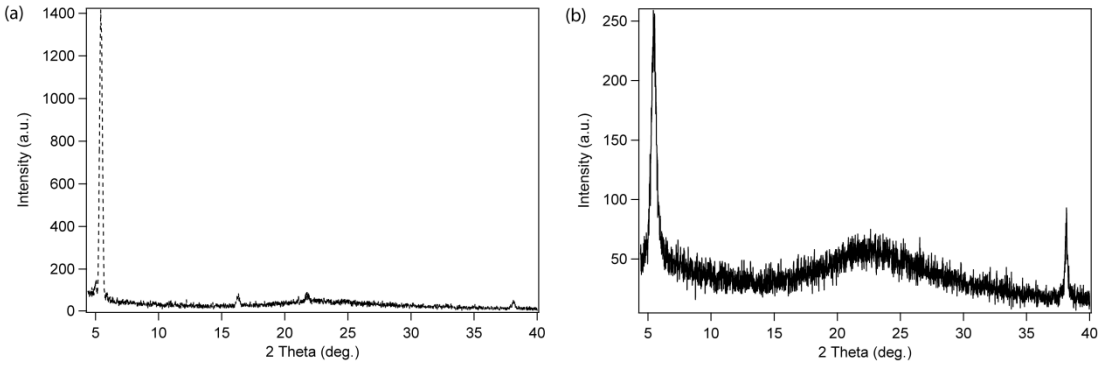

Figure 5.5: X-ray diffractogram of diF-TES-ADT/P4MS thin-films on (a) 4-FTP rinsed and (b) 4-FTP annealed (140 °C) prepared on glass substrates.

peaks are detected with a much high ratio between these peaks compared with the XRD results for the 4-FTP rinsed substrate in **Fig.5.5(a)**. The resulting d_{001}-spacing for each XRD scan corresponds to (a) 16.26 nm (2θ = 5.43 °) and (b) 16.14 nm (2θ = 5.47 °), for 'rinsed' and 'annealed' substrates, respectively. The d-spacing extracted from **Fig.5.5(b)** is detected as being slightly smaller which could imply better crystal packing in this thin-film resulting in enhanced intermolecular transport. This hypothesis correlates with the device data in **Fig.5.1** which shows significantly higher saturation mobility when compared between the two devices. Single-crystal diF-TES-ADT has a triclinic structure with a unit cell parameters a = 7.2089 Å, b = 7.3170 Å, c = 16.352 Å, α = 87.718°, β = 89.993°, and γ = 71.940°.[2]

5.2.5 Bias Stress of diF-TES-ADT Devices

The electrical stability was investigated by gated-bias stress with a prolonged gate bias of V_{GS} = -40V and V_{DS} = 0V in air ambient conditions under relative humidity ~40%. Each bias stress was applied for a total duration of 720 minutes and measured every 30 minutes, with only the initial and final scans presented below.

The 4-FTP annealed device on glass displayed a shift to lower off-currents with continual bias-stressing of the gate, and minimal deviation in the on-current, shown in **Fig.5.6(a)**. This off-current shift occurred within the first 60 minutes of bias-stressing and remained unchanged up to the final measurement at 720 minutes. A corresponding drop in the mobility occurred and stabilised at this time, shown in **Fig.5.6(b)**. Similar behaviour in the off-current was observed for 4-FTP rinsed devices on glass which occurred with the first 1 hour of biasing, shown in **Fig.5.7(a)**. The shape of the transfer curve is well defined in this instance, with better subthreshold swing and minimal deviation in the turn-on voltage. Again, a corresponding reduction in mobility was observed, shown in **Fig.5.7(b)**.

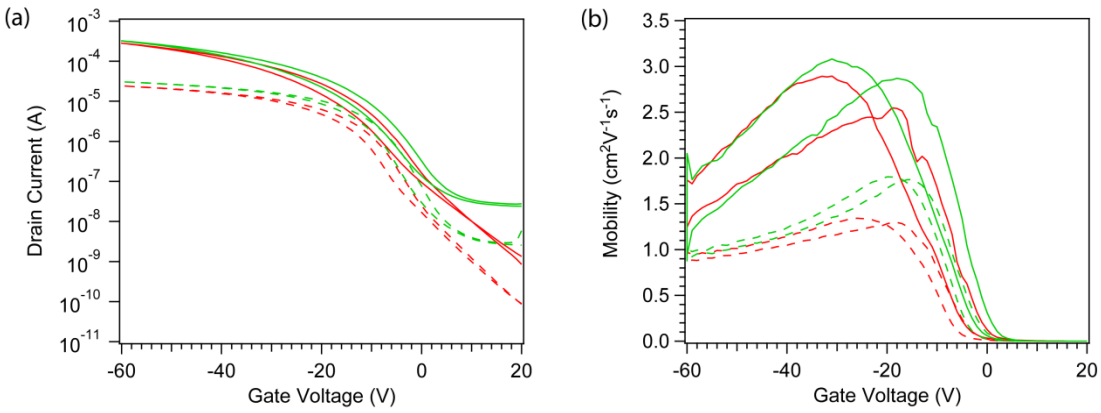

Figure 5.7: Bias stress of diF-TES-ADT/P4MS on 4-FTP (annealed at 140 °C) (a) transfer curve and (b) mobility plot. - - - Initial scan (linear); —— Initial scan (saturation); - - - 720 minutes (linear); —— 720 minutes (saturation).

The approach of gate stressing each device appears to be an effective means in stabilising the device operation (i.e. constant mobility) and overall reliability. The application of a gate-bias is known to have minimising effects on the off-current where drain-bias is known to be effective in reducing the V_T variation.[11] The

lowering in the off-current with gate-stress suggest a reduction in the charge trapping at the dielectric/OSC interface. A lowering in the drain leakage current observed for both devices points towards mechanisms involving interface traps or surface traps which would result in conduction via gate-induced drain leakage.[11] Gated-bias stress can reduce the interface trap density and consequently reduce the leakage current due to modification of the dielectric and source/drain interfaces formed with the OSC. Additionally, an increase in the surface barrier after gate stressing would reduce the number of trapped charge-carriers at the surface, resulting in improved tunnelling of charges from the gate.[11]

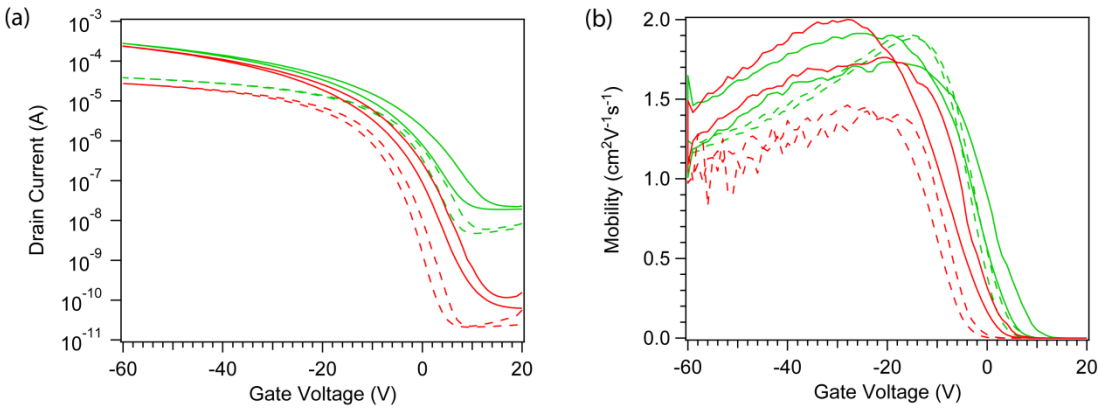

Figure 5.8: Bias stress of diF-TES-ADT/P4MS on 4-FTP (rinsed with solvent) (a) transfer curve and (b) mobility plot. - - - Initial scan (linear); —— Initial scan (saturation); - - - 720 minutes (linear); —— 720 minutes (saturation).

5.3 Conclusion

The surface energy of the substrate is an extremely effective way to control the morphology of a proprietary active-layer material, along with SAM modification of the source/drain electrodes. This work has shown both regions strongly dictate the resulting thin-film morphology, and in the case of TIPS/P4MS active-layers an

increased polar surface leads to enhanced thin-film formation. The low polar constituent of the surface energy for the P014 passivation layer may limit the degree of phase separation inhibiting charge transport through the active material, resulting in the poor device performance observed.

5.4 References

[1] D. J. Gundlach, J. E. Royer, S. K. Park, S. Subramanian, O. D. Jurchescu, B. H. Hamadani, A. J. Moad, R. J. Kline, L. C. Teague, O. Kirillov, C. A. Richter, J. G. Kushmerick, L. J. Richter, S. R. Parkin, T. N. Jackson, J. E. Anthony, *Nat. Mater*, (2008) **7**, 216.

[2] O. D. Jurchescu, S. Subramanian, R. J. Kline, S. D. Hudson, J. E. Anthony, T. N. Jackson, D. J. Gundlach, *Chem. Mater*. (2008) **20**, 6733.

[3] S. Subramanian, S. K. Park, S. R. Parkin, V. Podzorov, T. N. Jackson, J. E. Anthony, *J. Am. Chem. Soc*., (2008) **130**, 2706.

[4] S. K. Park, D. A. Mourey, S. Subramanian, J. E. Anthony, T. N. Jackson, *Appl. Phys. Lett*., (2008) **93**, 043301.

[5] S. K. Park, Ph.D Thesis, *High Mobility Solution Processed Organic Thin-Film Transistors*, (2007), Pennsylvania State University.

[6] J. Smith, R. Hamilton, M. Heeney, D. M. DeLeeuw, E. Cantatore, J. E. Anthony, I. McCulloch, D. D. C. Bradley, T. D. Anthopoulos, *Appl. Phys. Lett*,. (2008) **93**, 253301.

[7] J. Smith, M. Heeney, I. McCulloch, J. N. Malik, N. Stingelin, D. D. C. Bradley, T. D. Anthopoulos, *Org. Electron*. (2012) **12**, 143.

[8] J. Smith, R. Hamilton, Y. Qi, A. Kahn, D. D. C. Bradley, M. Heeney, I. McCullock, T. D. Anthopoulos, *Adv. Funct. Mater*. (2010) **20**, 2330.

[9] Y. Mei, M. A. Loth, M. Payne, W. Zhang, J. Smith, C. S. Day, S. R. Parkin, M. Heeney, I. McCulloch, T. D. Anthopoulos, J. E. Anthony, O. D. Jurchescu, *Adv. Mater*. (2013) **25**, 4352.

[10] J. Smith, W. Zhang, R. Sougrat, K. Zhao, R. Li, D. Cha, A. Amassian, M. Heeney, I. McCulloch, T. D. Anthopoulos, *Adv. Mater*. (2012) **24**, 2441.

[11] S. Ju, D. B. Janes, G. Lu, A. Facchetti, T. J. Marks, *Appl. Phys. Lett.*, (2006) **89**, 193506.

Chapter 6

Conclusion

6.1 Conclusion

Self-assembly is an extremely effective process for the development of organic electronic devices as the construction of layers without guidance from external stimuli can provide a simplistic methodology in the preparation of such applications. The key benefits of SAMs as a surface treatment procedure are the ability to fine-tune the energy-barrier height at critical interfaces and tailor surface energy conditions. Large selections of SAMs with varied constituent components (i.e. head-group, functional-group, and auxiliary group) are commercially available offering great diversity in this process step. The approach of SAM functionalisation is simple, effective and fast which bodes well from a manufacturing standpoint.

This thesis highlights the fundamental constraints observed for short self-assembly times of aromatic thiolates and elucidates their fundamental characteristics, as discussed in **Chapter 3**. Longer immersion times for self-assembly does increase the density of thiols present on the functionalised metal surface as studied by XPS, although the overall impact of this result on OTFT performance is limited by unfavourable changes in surface energy of the substrate which caused dewetting of the active-blend material. The benefit of prolonged self-assembly is to maximise the overall work function shift of the metal, although the presence of an interfacial barrier formed from the deposition of the organic semiconductor onto the SAM treated electrode can strongly dictate the ultimate energy-level alignment at this interface. Highly fluorinated aromatic molecules presented the largest increase in

hydrophobicity which may have consequential results on surface wetting if too hydrophobic, although such systems are favourable due to the large obtainable work function for matching with the high ionisation potential of some organic semiconductors. In addition, this thesis examined the effects of post-treatment annealing of the SAM and its resultant impact on its electronic and chemical characteristics, alongside adsorption/desorption behaviour. These effects were observed in the electrical performance of OTFTs with enhancements observed through high temperature annealing between 100 – 200 °C as discussed in **Chapter 4** and **Chapter 5**. This work has highlighted source/drain post-treatment annealing after SAM modification as an important processing variable for enhancing OTFT performance development.

Disentangling changes in work function and surface energy with respect to their influence on I-V characteristics of OTFTs is challenging, although optimisation of both physical properties for specific active-materials is critical for achieving good device performance. Changes in the homogeneity of the organic semiconductor layer were observed for ternary blend active-layers with different SAM treatments, although the structural ordering of the small molecule and polymer binder within the thin-film remains inconclusive from SIMS experiments conducted herein. The unavoidable occurrence of surface-dipoles introduced from the formation of the electrode/organic semiconductor interface is known to hamper the charge-injection of carriers due to the energetic misalignment, although the resulting morphology of the active-blend strongly dictates the charge-transport through the device. The result of increasing the work function beyond that of the HOMO level of the organic semiconductor presented no discernible change in OTFT performance, specifically

with respect to the charge-carrier mobility, although it is essential to not fall below this value.

There are several barriers which need to be overcome before OTFTs become fully commercialised. One important prerequisite for upscaling is the achievement of high yield and good uniformity of working devices across the substrate, with minimal deviation in OTFT parameter characteristics between all devices. This problem is very complex, particularly for ternary based systems, requiring understanding of the chemical and electrical properties of all materials for optimisation of the interfaces formed between layers, along with engineering of the device geometry. The work in thesis highlights the complexity in fabricating solution-processed OTFTs and how ternary blend active-layers and SAMs can be used to enhance their device characteristics.